

NON-EQUILIBRIUM CHEMISTRY FOR HYPERSONIC FLOWS
USING AN EDGE-BASED FINITE ELEMENT METHOD

Jory Seguin

Department of Mechanical Engineering
McGill University, Montréal
July 2018

A thesis submitted to McGill University
in partial fulfillment of the requirements for the degree of
MASTER OF MECHANICAL ENGINEERING

© Jory Seguin 2018

Abstract

The development of hypersonic vehicles for civilian transport presents several multi-disciplinary design challenges. The highly energetic conditions in the flow field can lead to chemical and thermal non-equilibrium effects that render complex the estimation of aerothermodynamic quantities such as lift, drag, mechanical stresses and heat fluxes through the body. These calculations are essential for the aerodynamic design of the vehicle as well as the development of thermal protection systems. Thus, there is a need for advanced computational tools to assist in the preliminary design phase.

The present work extends the capabilities of the HALO3D simulation software into the non-equilibrium regime. The numerical approach enables accurate and robust computation of hypersonic flows, as well as relatively straightforward coupling with additional physical models. The physical and numerical modeling of several aspects related to chemical non-equilibrium are discussed. The species transport equations are solved in a loosely-coupled manner to reduce computational cost and simplify implementation. Reactions are modeled using laminar finite-rate chemistry, and various vibration-dissociation coupling models account for the effect of thermal non-equilibrium in the chemistry. Varying mixture composition is accounted for in all thermodynamic relations and several mixture transport property models are implemented. All calculations are encapsulated in an edge-based finite element framework that simultaneously incorporates many of the advantages of finite volume and finite element methods.

A methodical verification and validation is carried out to isolate the effects and mechanisms in the model. The chemical source term and vibration-dissociation coupling models are first verified through unsteady reactor cases, then the mass diffusion is verified using a mixing layer problem. Subsequently, two-dimensional and three-dimensional flows in thermochemical non-equilibrium are simulated and comparisons are made against established codes and experimental data. Overall, the solver is shown to be extremely capable and promising for future hypersonics research.

Résumé

La conception de véhicules hypersoniques pour le transport civil présente plusieurs défis multidisciplinaires. Les hautes températures peuvent déclencher des effets chimiques et thermodynamiques hors-équilibre, rendant complexe la prédiction de quantités aérodynamiques telles que la portance, la traînée, les contraintes mécaniques et les flux thermiques. Ces calculs sont essentiels pour la conception aérodynamique du véhicule ainsi que le développement de systèmes de protection thermique.

Cette recherche étend les capacités du logiciel de simulation HALO3D jusqu'au régime hors-équilibre. L'approche numérique proposée permet la simulation robuste d'écoulements hypersoniques ainsi que le couplage de modèles physiques additionnels. La modélisation d'écoulements hors-équilibre chimique est clairement démontrée. Les équations de transport d'espèces chimique sont résolues séparément, réduisant le coût du calcul et simplifiant la modélisation du système. Les réactions chimiques considèrent un mélange à composition chimique variable et sont simulées à l'aide d'un modèle laminaire à taux de réaction fini. La modélisation tient compte de divers modèles de couplage des modes vibrationnels et de dissociation et de leurs effets thermodynamiques sur les réactions. La méthode des éléments finis avec assemblage par arête est utilisée, groupant ainsi les avantages des méthodes de volumes et d'éléments finis.

Un plan de vérification et validation méthodique est appliqué, introduisant progressivement les effets spécifiques du modèle. Le terme source et le modèle de couplage vibration-dissociation est examiné à l'aide de réacteurs, alors que la diffusion chimique est vérifiée avec une couche de mélange. Par la suite, des écoulements deux et trois-dimensionnelles hors d'équilibre chimique et thermodynamique sont calculés et des comparaisons sont effectuées par rapport à des codes établis et des mesures expérimentales. Conséquemment, le logiciel s'est avéré être très apte et semble prometteur pour des recherches futures.

Acknowledgements

I would like to acknowledge the individuals who were instrumental in helping me conduct my research and bring this thesis to its present level. First and foremost, my deepest gratitude to my co-supervisors, professors Wagdi G. Habashi and Marco Fossati, whose expertise and direction made this work possible. I would also like to thank Drs. Dario Isola and Guido Baruzzi at ANSYS Canada for their extensive technical support throughout my research, as well as their editorial assistance for both this thesis and our scientific papers. This entire research program is enabled through the generous financial support of the Lockheed Martin Company (LMCO) and NSERC, and I would particularly like to thank Drs. Ned Allen and Luke Uribarri from LMCO who participated in our capstone meetings. Additionally, I would like to thank Compute Canada and CLUMEQ for their computational resources, which allowed this research to be done in a timely manner. Many other components of this exciting research project are being completed by my colleagues Song Gao and Wenbo Zhang, with whom I collaborated closely during my work. My thanks to all the members of the CFD Lab at McGill; a creative and enjoyable work environment. Though my research has been deeply fulfilling, it has not been without its stresses and strains. I would like to thank Emily McRae for supporting me as well as all of my close friends who helped me balance out my life. Moreover, many thanks to my sister, Krista Seguin, whose great example showed me the importance of tenacity and determination. Finally, I cannot express enough gratitude to my parents Mark and Carol Seguin, whose love and support enabled me to pursue my passion, and who taught me the value of hard work.

“For small creatures such as we, the vastness is bearable only through love.”
- Carl Sagan

Table of Contents

Abstract.....	I
Résumé	II
Acknowledgements.....	III
Table of Contents	IV
List of Figures	VI
List of tables	VIII
List of Symbols	IX
1 Introduction.....	1
1.1 Research Motivation	1
1.2 Thesis Outline and Contributions	2
2 Background and Literature Review.....	4
2.1 Physical Phenomena in Hypersonic Flows.....	4
2.2 Non-equilibrium Chemistry.....	7
2.3 Numerical Methods for Hypersonic Non-equilibrium Flows.....	9
3 Physical Modeling	11
3.1 Governing Equations	11
3.2 Thermochemical Modeling	13
3.2.1 Internal Energy Representation Using NASA Polynomials.....	16
3.2.2 Internal Energy Representation Using Boltzmann Energy Distribution.....	16
3.2.3 Comparison of Internal Energy Models.....	17
3.3 Mixture Transport Coefficients	19
3.3.1 NIST Least-squares Polynomials	19
3.3.2 Blottner Viscosity and Eucken Conductivity	19
3.3.3 Sutherland’s Law	20
3.3.4 Comparison of Transport Property Models.....	20
3.4 Chemical Kinetics Model.....	21
3.4.1 Equilibrium Rate Constant via Polynomials	23
3.4.2 Equilibrium Rate Constant via Gibbs Free Energy.....	24
3.4.3 Comparison of Reaction Schemes	24
3.5 Thermodynamic Non-equilibrium	26
3.5.1 Two-temperature Model	26
3.5.2 Vibrational-electronic Energy Relaxation.....	28
3.6 Vibration-dissociation Coupling.....	29
3.6.1 Park’s Rate-controlling Temperature Model.....	29
3.6.2 Coupled Vibration-dissociation-vibration Model.....	30
3.6.3 Comparison of Vibration-dissociation Coupling Models	31
3.7 Chemical Diffusion.....	32
4 Numerical Modeling.....	35
4.1 Finite Element Discretization	35
4.2 Edge-based Assembly	37
4.3 Flux Stabilization Techniques	40
4.3.1 The Riemann Problem	40

Table of Contents

4.3.2	Roe's Scheme	42
4.3.3	AUSM Scheme	43
4.3.4	Flux Stabilization for the Decoupled Chemical System	44
4.4	MUSCL Reconstruction.....	45
4.5	Time Discretization.....	47
4.6	Loosely-coupled Methodology and Solution of the Linear System.....	48
4.7	Boundary Conditions	50
4.7.1	Inlets	51
4.7.2	Outlets.....	52
4.7.3	Walls	52
5	Results	54
5.1	Validation of Chemical Source Term	54
5.1.1	Hydrogen-iodine Production	54
5.1.2	High-temperature Air Reaction	56
5.2	Validation of Vibration-dissociation Coupling.....	57
5.3	Inviscid Thermo-chemical Non-equilibrium Flow Past a Cylinder	59
5.4	Validation of Species Mass Diffusion.....	64
5.5	Viscous Chemical Non-equilibrium Flow Past a Cylinder	67
5.6	Viscous Thermo-chemical Non-equilibrium Flow Past a Sphere.....	73
6	Conclusions	82
7	References	85
	Appendix A: Species data	88
	Appendix B: Chemical models	89
	Appendix C: Derivation of Jacobian Matrices.....	93
	Appendix D: Example of Reaction Kinetics	99
	Appendix E: Chemical Equilibrium Solver	100

List of Figures

Figure 2.1 - Mach number flow regimes.....	4
Figure 2.2 - Representative flow field of reentry capsule (left) [11] and charred ablative shield of Gemini capsule (right) [12].....	7
Figure 2.3 - Reentry profile of space shuttle Orbiter with overlays of non-equilibrium regions [1].....	8
Figure 3.1 - Internal energy modes of a gas.....	17
Figure 3.2 - Internal energy of frozen air in thermodynamic equilibrium versus temperature using various thermodynamic models.....	18
Figure 3.3 - Constant volume specific heat of frozen air in thermodynamic equilibrium versus temperature using various thermodynamic models.....	18
Figure 3.4 - Dynamic viscosity of frozen air using various transport property models.....	21
Figure 3.5 - Thermal conductivity of frozen air using various transport property models.....	21
Figure 3.6 - Forward reaction rate coefficients for nitrogen (left) and oxygen (right) dissociation using various reaction schemes.....	25
Figure 3.7 - Equilibrium rate constants for nitrogen (left) and oxygen (right) dissociation using various reaction schemes and the analytical (Gibbs) formulation.....	26
Figure 3.8 - VD coupling factor for nitrogen (left) and oxygen (right) dissociation reactions using various coupling models.....	32
Figure 4.1 - Diagram of 1D Riemann problem.....	41
Figure 4.2 - Diagram of MUSCL piecewise linear one-dimensional reconstruction.....	46
Figure 4.3 - Sweby diagram of various flux limiters.....	47
Figure 4.4 - Flow chart of loosely-coupled solution methodology for chemical non-equilibrium flow.....	49
Figure 5.1 - Molar concentration of products and reactants versus time. HALO3D (solid) versus analytical solution (dashed).....	55
Figure 5.2 - Normalized number densities versus time for 5-species air. Comparison between HALO3D (solid) and Cantera (points).....	56
Figure 5.3 - Temperature of 5-species reacting air versus time. Comparison between HALO3D (solid) and Cantera (points).....	57
Figure 5.4 - Normalized number densities for relaxation of nitrogen in a heat bath. Comparison between HALO3D (lines) and hy2foam (points) using Park and CVDV-QK models.....	59
Figure 5.5 - Translation-rotational and vibrational-electronic temperatures for relaxation of nitrogen in a heat bath. Comparison of HALO3D (lines) with hy2foam (points) using the Park and CVDV-QK models.....	59
Figure 5.6 - Computational mesh (left) and problem setup (right) for hypersonic inviscid thermo-chemical non-equilibrium flow past a cylinder.....	61
Figure 5.7 - L2 residuals for first order (left) and MUSCL (right) solutions of hypersonic inviscid thermo-chemical non-equilibrium air flow past cylinder.....	61
Figure 5.8 - Temperatures (left) and pressure (right) along stagnation line for hypersonic inviscid thermo-chemical non-equilibrium flow past cylinder. Comparison between HALO3D (solid) and NASCART-GT (dashed).....	62
Figure 5.9 - Molar fractions (left) and density (right) along stagnation line for hypersonic inviscid thermo-chemical non-equilibrium flow past cylinder. Comparison between HALO3D (solid) and NASCART-GT (dashed).....	62
Figure 5.10 - Trans-rotational temperature (left) and vibrational-electronic temperature (right) contours for hypersonic inviscid thermo-chemical non-equilibrium flow past a cylinder.....	63
Figure 5.11 - Damköhler number (left) and mixture gas constant (right) for hypersonic inviscid thermo-chemical non-equilibrium flow past cylinder.....	64
Figure 5.12 - Mass fraction contours of N2 for zero-shear mixing layer.....	65

List of Figures

Figure 5.13 - Mass fraction profile at channel outlet. Comparison of HALO3D solutions (solid) versus reference (dashed).	66
Figure 5.14 - Mass fraction of N ₂ along y=0.00055 m plane. Comparison between HALO3D (solid) and reference (dashed).	67
Figure 5.15 - Computational grid (left) and problem setup (right) for high-enthalpy viscous chemical non-equilibrium flow past a cylinder.	69
Figure 5.16 - L2 residuals for first-order (left) and second-order (right) solution of high-enthalpy viscous chemical non-equilibrium flow past a cylinder	69
Figure 5.17 - Temperature along stagnation line for high-enthalpy viscous chemical non-equilibrium flow past a cylinder. Comparison between HALO3D (solid) and Wasserman (dashed).	70
Figure 5.18 - Mass fractions along stagnation line for high-enthalpy viscous chemical non-equilibrium flow past a cylinder. Comparison between HALO3D (solid) and Wasserman (points).	71
Figure 5.19 - Wall pressure (left) and heat flux (right) for high-enthalpy viscous chemical non-equilibrium flow past cylinder. Comparison between HALO3D (solid), Wasserman (dashed) and HEGIII experimental data (points)	71
Figure 5.20 - Temperature [K] (left) and pressure [Pa] (right) contours for viscous chemical non-equilibrium flow past cylinder	72
Figure 5.21 - Mass fractions contours of N ₂ (left) and NO (right) for viscous chemical non-equilibrium flow past cylinder	73
Figure 5.22 - Problem setup for Lobb's sphere	73
Figure 5.23 - Computational grid (left) and close-up view of near-wall elements (right) for Lobb's sphere	74
Figure 5.24 - L2 residuals for first order (left) and second order (right) solution of Lobb's sphere.	75
Figure 5.25 - Temperature contours for Lobb's sphere.	75
Figure 5.26 - Pressure contours for Lobb's sphere. Comparison with experimental shock locations [71].	76
Figure 5.27 - Temperatures along stagnation line for Lobb's sphere.	77
Figure 5.28 - Mass fractions along stagnation line for Lobb's sphere	77
Figure 5.29 - Temperatures along stagnation line for Lobb's sphere. Comparison between calorically perfect, thermally perfect and non-equilibrium physical models.	78
Figure 5.30 - Temperatures along stagnation line for Lobb's sphere. Comparison between polynomial and Boltzmann heat models	79
Figure 5.31 - Trans-rotational (left) and vibrational-electronic (right) temperatures along stagnation line for Lobb's sphere. Comparison between various reactions schemes using analytical equilibrium constant	80
Figure 5.32 - Diatomic nitrogen (left) and oxygen (right) mass fractions along stagnation line for Lobb's sphere. Comparison between various reaction schemes using analytical equilibrium constant	80
Figure 5.33 - Nitric oxide (left) and atomic nitrogen and oxygen right) mass fractions along the stagnation line for Lobb's sphere. Comparison between various reaction schemes using analytical equilibrium constant.	81
Figure A.1 - Equilibrium molar fractions of five-species air model.	103

List of Tables

Table 4.1 - Riemann state for various flow conditions.....	51
Table 5.1 - Forward reaction rate parameters for hydrogen iodine case.....	55
Table 5.2 - Forward reaction rate parameters for nitrogen relaxation case.....	58
Table 5.3 - Flow parameters for hypersonic thermo-chemical inviscid flow past a cylinder	60
Table 5.4 - Flow parameters for high-enthalpy viscous chemical non-equilibrium flow past a cylinder ...	68
Table 5.5 - Flow parameters for Lobb's sphere	74

List of Symbols

Latin Alphabet

a	Speed of sound [m/s]
A_f	Pre-exponential Arrhenius parameter
$B_{(i)}$	Equilibrium constant parameters
C_v	Specific heat capacity at constant volume [kJ/(kg·K)]
C_p	Specific heat capacity at constant pressure [kJ/(kg·K)]
e	Internal energy per unit mass [J/kg]
E	Total energy per unit volume [J/m ³]
E_a	Activation energy Arrhenius parameter [J/mol]
\mathbf{F}	Flux vector
h	Specific enthalpy [J/kg]
H	Total enthalpy [J/kg]
\mathbf{J}	Diffusion flux vector
k_f	Forward rate coefficient
k_b	Backward rate coefficient
K_{eq}	Equilibrium rate constant
M	Molar mass [kg/mol]
N_s	Number of species in mixture
N_r	Number of reactions in model
p	Pressure [Pa]
$\dot{\mathbf{q}}$	Heat flux vector
\mathbf{Q}	Conservative variables vector
R_f	Forward reaction rate [mol/(m ³ ·s)]
R_b	Backward reaction rate [mol/(m ³ ·s)]
R_s	Individual gas constant [J/(kg·K)]
s	Specific entropy [J/(K·kg)]
\mathbf{S}	Source term vector
t	Time [s]
T	Temperature [K]
T_{tr}	Translational temperature [K]
T_{ve}	Vibrational-electronic temperature [K]
u, v, w	Cartesian Velocity components [m/s]
\mathbf{W}	Primitive variables vector
x, y, z	Cartesian direction components [m]
Y_s	Species mass fraction

Greek Alphabet

γ	Ratio of specific heats
δ	Thickness [m]
η_f	Exponential Arrhenius parameter
κ	Thermal conductivity [W/(m·K)]
λ	Mean free path [m]
μ	Dynamic viscosity [Pa·s]
ν'_s	Stoichiometric coefficient of reactant species s

List of Symbols

v_s''	Stoichiometric coefficient of product species s
ρ	Density [kg/m^3]
$\boldsymbol{\tau}$	Shear stress vector
$\dot{\omega}_s$	Species production/destruction term [$\text{kg}/\text{m}^3\text{s}$]

Non-Dimensional Numbers

CFL	Courant-Friedrichs-Lewy number
Da	Damköhler number
Kn	Knudsen number
Le	Lewis number
M	Mach number
Re	Reynolds number
Sc	Schmidt number

Constants

$k_B = 1.3806\text{E} - 23$	Boltzmann's Constant [J/K]
$N_A = 6.0221\text{E}23$	Avogadro's Number [$1/\text{mol}$]
$R_u = 8.3145$	Universal Gas Constant [$\text{J}/(\text{mol}\cdot\text{K})$]

Abbreviations

BVP	Boundary Value Problem
CFD	Computational Fluid Dynamics
DSMC	Direct Simulation Monte Carlo
FDM	Finite Difference Method
FDS	Flux Difference Splitting
FEM	Finite Element Method
FVM	Finite Volume Method
FVS	Flux Vector Splitting
IVP	Initial Value Problem
LEO	Low Earth Orbit
MUSCL	Monotonic Upstream-Centered Scheme for Conservation Laws
PDE	Partial Differential Equation
SCRAMJET	Supersonic Combustion Ramjet
SSTO	Single-Stage to Orbit
TPS	Thermal Protection System
TVD	Total Variation Diminishing

1 Introduction

1.1 Research Motivation

The first man-made object to reach hypersonic speed – typically defined as being above Mach 5 – reached a peak velocity of 6138 km/h and burned up upon reentry, leaving only charred remains in its wake [1]. This was the first practical indication that hypersonic flight presents many difficulties not encountered in the supersonic flight regime, and that alternative designs would be needed. Despite these various challenges, considerable research and development has occurred in this industry.

Examples of hypersonic flight applications include hypersonic transportation, single-stage-to-orbit (SSTO) aircraft, and atmospheric reentry vehicles. The Concorde was a supersonic airliner that was first introduced in the 70s and flew until 2004. The economic demise of this supersonic airliner can be attributed in large part to increased maintenance costs and engine emissions as well as bans on sonic booms over land [2]. A resurgence of interest in supersonic civilian flight is occurring, where advancements in manufacturing, propulsion, and vehicle design could significantly reduce costs, emissions, and noise.

The interest in SSTO vehicles has the goal of reducing space launch operating costs through vehicle reusability. Currently, orbital launches are carried out using fully or partially expendable rockets. The loss of the rocket stages therefore represents a significant portion of the operating cost, while the cost of fuel is typically less than one percent [3]. A middle ground solution is currently being industrialized by SpaceX in their multi-stage reusable launch systems. Progress in these technologies could drastically reduce the cost of space access and create an economic and technological boom in various space-related industries.

Due to the challenging nature of these engineering problems, suitable research and development of new designs must be conducted. Experimental testing in hypersonic conditions can be tremendously complex, costly, and often impossible [4]. Advancements in numerical methods and computing power has made numerical testing increasingly viable as an alternative to experiments. An essential class of design tools are Computational Fluid Dynamics (CFD) software packages, which are extremely useful for predicting various aerothermodynamic quantities, and whose efficiency has benefitted from continuous advancements in computational technology [5]. However, the hypersonic flight envelope is subject to numerous physical

phenomena that significantly increase the complexity of physical and numerical models. If accurate and efficient numerical methods can be developed for these flows, then simulations may become an integral part of the preliminary design and analysis phase for hypersonic vehicles.

The objective of the hypersonics project at McGill university's CFD Lab is to fill the gap identified in existing commercial CFD codes for hypersonic flight regimes. This research programme is a collaboration between the CFD Lab and ANSYS, with the backing of the Lockheed Martin Company. To accomplish this task, a software suite has been developed named HALO3D. The solver uses an edge-based methodology to combine the advantages of both FEM and FVM, such as robustness on highly stretched grids and the application of intricate flux schemes and limiters, respectively [6]. Ongoing work is being done to extend the capabilities of the hypersonic code with additional physical models [7]. The code also utilizes a decoupled methodology that enables a modular approach to the solution of the governing equations as well as an increase in computational efficiency [8]. This flexible framework also allows the easy inclusion of additional physical models. Emphasis is being placed on numerical methods which increase the robustness of the code without sacrificing accuracy.

1.2 Thesis Outline and Contributions

The present thesis focuses on developing physical models and numerical methods used in the simulation of the chemical non-equilibrium equations of hypersonic flows. Section 2.1 will provide background knowledge in the field of compressible flows and present relevant physical phenomena occurring in hypersonic flow fields. The numerical techniques which have been developed by various authors in this field will be discussed in Section 2.2. Section 3 will present the physical modeling employed in the HALO3D code, including the full governing equations, thermo-chemical relations, modeling of transport properties, chemical kinetics and species diffusion. Section 4 will discuss how the previously mentioned set of equations was solved numerically. Throughout the development of the solver's new capabilities, several verification and validation test cases were conducted. These are discussed in Section 5, in an order that builds up from simple zero-dimensional reactors for the verification of source terms, to viscous hypersonic thermo-chemical non-equilibrium flows past canonical geometries. Finally, conclusions and suggestions for future work will be offered in Section 6.

The present work contributes to the area of numerical methods as applied to hypersonic flows. More specifically, the phenomenon of chemical non-equilibrium has been addressed. The author has developed a decoupled edge-based FEM solver for the conservation of species mass with finite-rate chemistry. Several mixture transport property and vibration dissociation coupling models were also implemented, as well as species diffusion terms appearing in the energy conservation equations.

2 Background and Literature Review

2.1 Physical Phenomena in Hypersonic Flows

When studying compressible fluid flows, an essential value is the speed of sound. Sound is propagated as a series of longitudinal compression waves within a medium, and therefore its transmission speed is dependent on the fluid's compressibility [1]. This is an important notion in aerodynamics for the study of transonic and supersonic flow and the various effects associated with these flow regimes. Flow regimes can be classified via their Mach number, defined as the ratio of the local velocity to the local speed of sound

$$M = \frac{V}{a} \quad (2.1)$$

The range of Mach numbers with associated fluid flow regimes are shown in Figure 2.1. When the local Mach number is less than unity the flow is said to be subsonic. Although compressibility in a fluid is always present to some extent, flows may be treated as incompressible when changes in fluid density are negligible, which is for all practical purposes true of flows where $M < 0.3$.

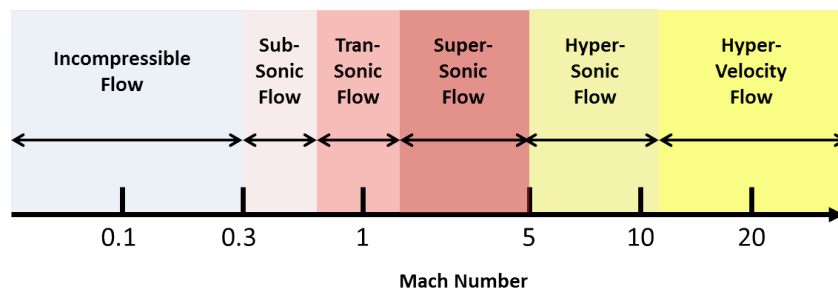


Figure 2.1 - Mach number flow regimes

Flows in which the Mach number is greater than unity are known as supersonic. In a steady flow with a supersonic freestream, shock waves may form, which are the response of a fluid to a disturbance moving greater than the speed of information propagation. Although experiments show the thicknesses of these shock waves to be on the order of several hundred nanometers, on a macroscopic scale and in aerodynamic theory they are typically treated as an instantaneous increase in entropy. Shocks may also form when certain parts of the flow are locally supersonic due to fluid acceleration, in what is known as the transonic regime. Shock waves may be associated with a large increase in temperature, pressure and density and are therefore of great

concern in aerothermodynamic design [1]. For example, the elevated pressure and density can greatly reduce aerodynamic lift and increase drag. An accurate assessment of a vehicle's aerodynamic properties is essential for mission profile design as well as the development of thermal protection systems (TPS), control systems and avionics packages. The transition to the hypersonic flight regime is commonly defined at Mach 5, though its true definition is when a combination of effects, which will be discussed below, begin to manifest themselves.

Although the presence of strong shock waves in supersonic flows is problematic for the design of supersonic vehicles, the hypersonic flight envelope is susceptible to an even wider array of problems. First and foremost, hypersonic vehicles fly at even higher velocities, resulting in significant freestream kinetic energy. Reentry vehicles returning from orbit enter the Earth's atmosphere at least at low earth orbit (LEO) velocities of roughly 7.8 km/s [1]. The kinetic energy of the flow is converted mainly to thermal energy through recompression as well as viscous dissipation effects that occur within a boundary layer, resulting in extremely large heat fluxes to the body. Furthermore, the large freestream Mach numbers result in smaller deflection angles for oblique shocks emanating from the body. Consequently, the hot shock layer is located even closer to the vehicle, increasing heat fluxes. Other shocks propagating from the body may also lead to shock-shock interaction, which generates extremely high temperature and pressure regions [9].

Another issue with hypersonic flows is the presence of a thick boundary layer with respect to the vehicle. For the laminar compressible flow past a flat-plate, the theory predicts that the boundary layer thickness is proportional to the square of the Mach number and the inverse square root of the Reynolds number

$$\delta \propto \frac{M^2}{\sqrt{\text{Re}}} \quad (2.2)$$

Aside from increased drag and a significant displacement effect, it is known that the features of hypersonic flows can create a feedback effect named *viscous interaction*, which grows the boundary layer even further. This can give way to shock-boundary layer interaction, a complex phenomenon that can prompt flow separation. Separated flow may negatively impact aerodynamic force coefficients, disrupt air intakes and cause strong buffeting [1].

Vehicles that are designed to encounter high Mach number flows are likely to travel at high altitudes where the atmospheric density is very low. The Knudsen number is a non-dimensional number representing the ratio of the molecular mean-free path of a molecule, λ_m , to a characteristic length, L , as

$$\text{Kn} = \frac{\lambda_m}{L} \propto \frac{M}{\text{Re}} \quad (2.3)$$

This number is important in determining the validity of the continuum assumption when modeling fluid flows. The gas can be assumed to be a continuum for $\text{Kn} < 0.01$, when the mean-free path is very small in comparison to the characteristic length. The so-called *slip regime* ($0.01 < \text{Kn} < 0.1$) can still be adequately simulated using the Navier-Stokes equations with the inclusion of additional physics such as slip boundary conditions [7]. However, the *transitional flow* ($0.1 < \text{Kn} < 1.0$) and *free-molecular flow* regions ($\text{Kn} > 1.0$) cannot be described as a continuum, since the molecules are extremely sparse. As a result, a more accurate approach to modeling these non-continuum flows is to solve the Boltzmann equation or to use particle methods such as Direct Simulation Monte Carlo (DSMC) simulations [10], although these significantly increase computational costs.

Finally, the strong normal shock (sometimes referred to as a *bow shock*) generated by reentry vehicles, as seen in Figure 2.2 (left), can generate gas temperatures of over 10000 K, leading to significant high-temperature and non-equilibrium effects on the flow and severe heat fluxes to the vehicle, the result of which is shown in Figure 2.2 (right). For example, the vibrational energy modes and low-lying electronic states of the gas may become excited and the calorically perfect gas assumption can no longer be used. Furthermore, the large temperatures initiate chemical reactions, which may significantly change the composition of the gas and lead to substantial non-equilibrium chemistry effects, which will be discussed in the following section.

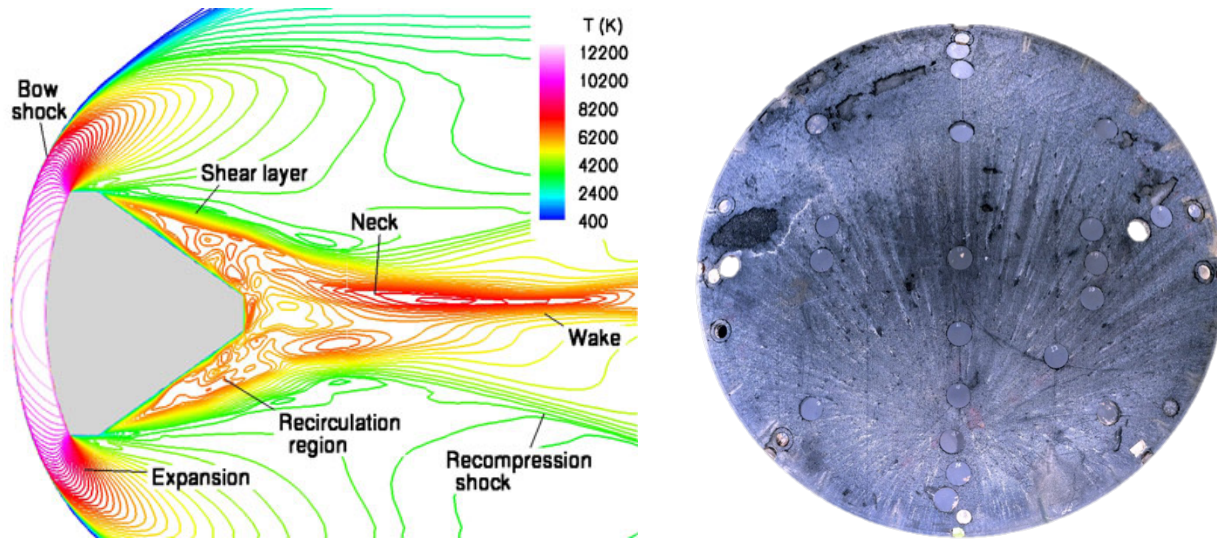


Figure 2.2 - Representative flow field of reentry capsule (left) [11] and charred ablative shield of Gemini capsule (right) [12]

2.2 Non-equilibrium Chemistry

The chemical regime of the flow is characterized by the ratio of characteristic flow time to the characteristic chemical reaction time, shown below

$$Da = \frac{\tau_f}{\tau_c} = \frac{L/V_\infty}{\rho_\infty/\dot{\omega}} \quad (2.4)$$

Three flow regimes can be defined. Firstly, if the residence time of the fluid is much smaller than the characteristic time of the reaction ($Da \ll 1$), then the fluid is advected away before the reaction can appreciably change the gas composition. This is named the *frozen flow regime* and is a typical assumption in fluid dynamics where non-equilibrium effects may be neglected. On the other hand, if the residence time of the fluid is long and the reactions occur relatively quickly ($Da \gg 1$), the fluid will reach its chemical equilibrium composition. This assumption is often used in stirred reactors, for example. Finally, when the chemical and fluid time scales are comparable ($Da \approx 1$) the flow is said to be in chemical non-equilibrium. This is the most complex case, as one must consider the rate of reactions in addition to the flow field to determine the chemical composition of the fluid. Typically, this regime necessitates the use of a finite-rate chemical kinetics model to compute reaction rates based on several parameters.

Many factors may influence the rate of a chemical reaction, such as the temperature and pressure of a gas, the concentration of reactants, the presence of catalysts, and several others

[13]. For example, the dissociation of diatomic oxygen and nitrogen occur at roughly 2000 K and 4000 K, respectively. At even higher temperatures, ionization reactions may occur, in which molecules or atoms lose electrons through collisions with other particles. The newly ionized plasma envelops the body, resulting in a non-adiabatic, radiating flow-field. The effect of this ionized gas on radio frequencies can lead to a communications blackout during reentry [1]. Intriguingly, the interaction of the charged particles with an imposed magnetic field may lead the way to innovative thermal protection systems [14]. As seen in Figure 2.3, even the space shuttle Orbiter, which used a softer lifting reentry profile to limit peak heat fluxes, encountered significant non-equilibrium effects. Vehicles that venture beyond Low Earth Orbit (LEO) reenter at even higher velocities, such as the Stardust Sample Return capsule, which reentered the atmosphere at roughly 12.9 km/s [1].

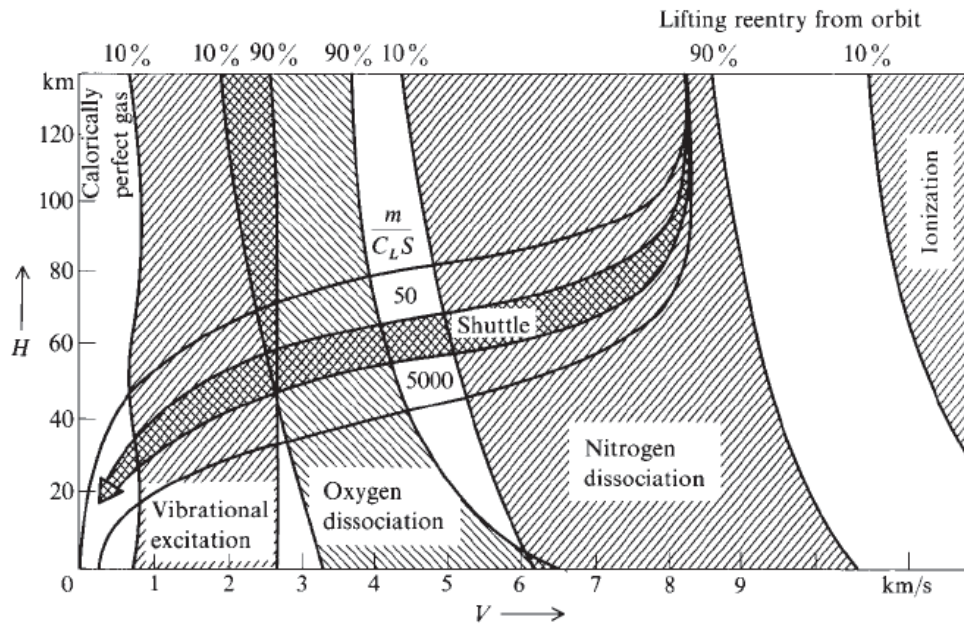


Figure 2.3 - Reentry profile of space shuttle Orbiter with overlays of non-equilibrium regions [1]

The consideration of finite-rate chemistry presents several modeling challenges. Firstly, the relevant chemical reactions must be identified along with their important parameters. The experimental determination of reactions rates has been the subject of continuous investigation [15], and the uncertainty in these rates tend to dominate the results of chemically reacting flow simulations. Furthermore, changes in gas composition due to chemistry are strongly interdependent with many aspects of the flow. For example, endothermic and exothermic reactions create changes in the internal energy of the gas. Additionally, mixture properties may

be drastically altered, and these may also be dependent on temperature, thus creating a feedback effect on the flow field. As for numerical difficulties associated with chemistry, the additional conservation equations significantly increase computational times and memory requirements, while the disparate chemical timescales result in a very stiff numerical system, demanding complex techniques for numerical integration [16].

2.3 Numerical Methods for Hypersonic Non-equilibrium Flows

The first use of CFD to simulate hypersonic flows solved the viscous-shock layer equations, a simplification to the Navier-Stokes equations for moderately low Reynolds numbers [17]. Such methods were used in the simulation of several vehicle configurations such as the space shuttle Orbiter [18] and the Galileo probe [19]. As numerical methods evolved, and computational resources increased, the focus shifted from simplifying the governing equations to augmenting them with non-equilibrium effects. Two landmark studies that first coupled the solution of species transport equations, including finite-rate chemistry, with the Navier-Stokes equations are those of Lee [20] and Park [21]. These studies were some of the first to identify numerical difficulties associated with simulating reacting flows. Park's 1985 paper presented a reacting air model that is still widely in use today, though more accurate reaction sets have been proposed.

The works of Gnoffo [22] and Candler [23] were the first to include simulations of hypersonic non-equilibrium effects in a multi-dimensional framework. The former is an extensive report that detailed the relevant governing equations and physical models and proposed numerical methods for these non-equilibrium flows. This research produced NASA's CFD code, the Langley Aerothermodynamic Upwind Relaxation Algorithm (LAURA), which was used during the design of the space shuttle's thermal protection system (TPS) [24]. Candler's model was the first to consider independent vibrational temperatures for each molecular species. Both works stressed the importance of using implicit methods for steady-state computations of reacting flows due to the numerical stiffness associated with the chemistry system. Candler and Wright applied this to the development of a data-parallel line-relaxation algorithm that later went on to become the DPLR code [25], currently in use at NASA Ames Research Center.

With much of the groundwork laid out, subsequent studies focused on the investigation of transport property and diffusion models [26], slip wall and catalytic boundary conditions [27, 28], ablation [29], radiation [30], and many more phenomena. Clearly, a comprehensive

simulation of all relevant effects can still be prohibitively expensive. The addition of finite-rate chemistry, especially when including ionization effects, significantly increases the number of equations of the system. More recently, Candler proposed an approach that reduced the computational times associated with the solution of these sets of equations by decoupling the chemistry and non-equilibrium energy equations from the Navier-Stokes system [16]. Despite all previous advances, the hypersonic simulation community still struggles with adequate grid generation, long computation times, uncertainty in kinetic data and dubious validation [5].

3 Physical Modeling

3.1 Governing Equations

The flow is modeled using the continuum assumption, which postulates that the gas is a continuous medium rather than composed of individual particles. Although the validity of this assumption decreases with an increase in Knudsen number, the implementation of chemical and thermal non-equilibrium accounts for many of the molecular processes encountered in the transition regime, making it adequate for a large range of hypersonic flows. An Eulerian framework is used.

Under the above assumptions, the fluid is modeled using the compressible Navier-Stokes equations extended with equations that account for non-equilibrium effects. The Navier-Stokes equations for a fluid in thermodynamic and chemical equilibrium consist of the conservation of total mass, momentum and energy. Body forces are neglected. When a gas mixture with variable composition is considered, supplementary mass conservation equations are solved for each additional species. Finally, a two-temperature model is considered in this work, where it is assumed that the translational and rotational energy modes, as well as the vibrational and electronic energy modes, may be lumped together. Therefore, an additional conservation of energy equation is solved for the vibrational-electronic energy. The full system of equations in conservative form is shown below

$$\frac{\partial Q}{\partial t} + \frac{\partial(\mathbf{F}_x^i - \mathbf{F}_x^v)}{\partial x} + \frac{\partial(\mathbf{F}_y^i - \mathbf{F}_y^v)}{\partial y} + \frac{\partial(\mathbf{F}_z^i - \mathbf{F}_z^v)}{\partial z} = S \quad (3.1)$$

The vector of conservative variables Q is given as

$$Q = \{\rho, \rho Y_1, \dots, \rho Y_{N_s}, \rho u, \rho v, \rho w, \rho e, \rho e_{ve}\}^T \quad (3.2)$$

where ρ is the total density, Y is a species mass fraction, u , v , and w are Cartesian velocities, e is the total energy per unit mass, and e_{ve} is the vibrational-electronic energy per unit mass. The inviscid fluxes \mathbf{F}^i are given by

$$\mathbf{F}_x^i = \begin{Bmatrix} \rho u \\ \rho Y_1 u \\ \dots \\ \rho Y_{N_s} u \\ p + \rho u^2 \\ \rho v u \\ \rho w u \\ \rho u \left(e + \frac{p}{\rho} \right) \\ \rho e_{ve} u \end{Bmatrix}, \quad \mathbf{F}_y^i = \begin{Bmatrix} \rho v \\ \rho Y_1 v \\ \dots \\ \rho Y_{N_s} v \\ \rho u v \\ p + \rho v^2 \\ \rho w v \\ \rho v \left(e + \frac{p}{\rho} \right) \\ \rho e_{ve} v \end{Bmatrix}, \quad \mathbf{F}_z^i = \begin{Bmatrix} \rho w \\ \rho Y_1 w \\ \dots \\ \rho Y_{N_s} w \\ \rho u w \\ \rho v w \\ p + \rho w^2 \\ \rho w \left(e + \frac{p}{\rho} \right) \\ \rho e_{ve} w \end{Bmatrix} \quad (3.3)$$

where p is the pressure. Viscous stresses are accounted for through the viscous flux vector \mathbf{F}^v , expressed as follows

$$\mathbf{F}_x^v = \begin{Bmatrix} 0 \\ -J_{1,x} \\ \dots \\ -J_{N_s,x} \\ \tau_{xx} \\ \tau_{xy} \\ \tau_{xz} \\ \mathbf{V}\boldsymbol{\tau}_x - \dot{q}_x \\ -\dot{q}_x^{VE} - \dot{q}_x^{D,VE} \end{Bmatrix}, \quad \mathbf{F}_y^v = \begin{Bmatrix} 0 \\ -J_{1,y} \\ \dots \\ -J_{N_s,y} \\ \tau_{yx} \\ \tau_{yy} \\ \tau_{yz} \\ \mathbf{V}\boldsymbol{\tau}_y - \dot{q}_y \\ -\dot{q}_y^{VE} - \dot{q}_y^{D,VE} \end{Bmatrix}, \quad \mathbf{F}_z^v = \begin{Bmatrix} 0 \\ -J_{1,z} \\ \dots \\ -J_{N_s,z} \\ \tau_{zx} \\ \tau_{zy} \\ \tau_{zz} \\ \mathbf{V}\boldsymbol{\tau}_z - \dot{q}_z \\ -\dot{q}_z^{VE} - \dot{q}_z^{D,VE} \end{Bmatrix} \quad (3.4)$$

where $\boldsymbol{\tau}$ is the viscous shear stress tensor, \mathbf{J} is a mass diffusion vector, \dot{q}^{TR} is the translational-rotational heat flux, \dot{q}^{VE} is the vibrational-electronic heat flux, and $\dot{q}^{D,E}$ and $\dot{q}^{D,VE}$ are the inter-diffusional enthalpy and inter-diffusional vibrational-electronic energy fluxes due to species mass diffusion, respectively. The total heat flux is given by a summation of contributions, shown below

$$\dot{q} = \dot{q}^{TR} + \dot{q}^{VE} + \dot{q}^{D,E} \quad (3.5)$$

with

$$\dot{q}^{TR} = -\kappa_{tr} \nabla T_{tr}, \quad \dot{q}^{VE} = -\kappa_{ve} \nabla T_{ve}, \quad \dot{q}^{D,E} = \sum_{s=1}^{N_s} J_s h_s \quad (3.6)$$

where κ_{tr} and κ_{ve} are the mixture translational-rotational and vibrational-electronic thermal conductivities, respectively. The inter-diffusional vibrational energy flux due to species mass diffusion is given by

$$\dot{q}^{D,VE} = \sum_{s=1}^{N_s} J_s e_{ve,s} \quad (3.7)$$

The viscous shear stress tensor in Einstein's notation is given by

$$\tau_{ij} = \mu \left(\frac{\partial u_i}{\partial x_j} + \frac{\partial u_j}{\partial x_i} \right) + \lambda \frac{\partial u_k}{\partial x_k} \delta_{ij} \quad (3.8)$$

where μ is the coefficient of viscosity and λ is obtained using the Stoke's hypothesis as $\lambda = 2\mu/3$ [31]. For a Newtonian fluid, $\tau_{ij} = \tau_{ji}$. Finally, the source terms S are given by

$$S = \{0, \dot{\omega}_1, \dots, \dot{\omega}_{N_s}, 0, 0, 0, 0, \dot{\omega}_{ve}\}^T \quad (3.9)$$

where $\dot{\omega}_s$ is a species chemical source term and $\dot{\omega}_{ve}$ is the vibrational-electronic energy source term. Note that the summation of the conservation of species mass equations equals the conservation of total mass, resulting in a redundant equation. The way in which this is resolved will be discussed in Section 4.6. To fully close this system, an equation of state is required that relates the intensive properties of the fluid. For this purpose, the ideal gas law is used, and its extension to gas mixtures is discussed in the following section.

3.2 Thermochemical Modeling

The medium is assumed to be a mixture of a number N_s of ideal gases. This assumes that both the volume occupied by the gas particles themselves, as well as the interaction forces between particles, are negligible [32]. Although these assumptions break down at extremely high pressures and very rarefied conditions, they are deemed valid for the range of conditions considered in this work. The species densities ρ_s and mass fractions Y_s respect the following relations

$$\rho = \sum_{s=1}^{N_s} \rho_s \quad Y_s = \frac{\rho_s}{\rho} \quad \sum_{s=1}^{N_s} Y_s = 1 \quad (3.10)$$

Since the gases behave ideally, each species also obeys the ideal gas law, and the total pressure is given by the sum of partial pressures p_s , as follows

$$p_s = \rho_s R_s T, \quad p = \sum_{s=1}^{N_s} p_s \quad (3.11)$$

Note that R_s is the individual gas constant for chemical species s . The mixture gas constant is computed as a mass-weighted average of the individual gas constants, shown below

$$R = \sum_{s=1}^{N_s} Y_s R_s \quad (3.12)$$

The molar concentration $[X_s]$ of a mixture component and the number density n_s may be found using the molar mass M_s as follows

$$[X_s] = \frac{\rho_s}{M_s}, \quad n_s = \frac{[X_s]}{N_A} \quad (3.13)$$

Where N_A is Avogadro's constant. The volumetric portion of a component in a gas mixture may be expressed as a molar fraction as follows

$$X_s = \frac{[X_s]}{\rho/M} = \frac{n_s}{n} = \frac{p_s}{p} \quad (3.14)$$

The speed of sound is a quintessential parameter for compressible flows. Based on classical mechanics [32] it is defined as

$$a^2 = \left(\frac{\partial p}{\partial \rho} \right)_s \quad (3.15)$$

For a perfect gas, the following simplified relations are obtained

$$a = \sqrt{\gamma RT} = \sqrt{\gamma \frac{p}{\rho}} \quad (3.16)$$

The total energy per unit volume E , is given by the sum of kinetic and internal energies e_s , defined as

$$\rho e = E = \frac{1}{2} \rho (u^2 + v^2 + w^2) + \rho \sum_{s=1}^{N_s} Y_s e_s \quad (3.17)$$

The specific enthalpy is related to the specific energy by the following relation

$$h = e + \frac{p}{\rho} \quad (3.18)$$

The species internal energy e_s for a gas assumed to be in thermodynamic equilibrium can be obtained from the following expression

$$e_s = C_{v,s}T + e_{f,s}^0 \quad (3.19)$$

where $C_{v,s}$ is the species specific heat at constant volume and $e_{f,s}^0$ is the species energy of formation, equal to the enthalpy of formation $h_{f,s}^0$ at a reference temperature. By convention, the enthalpy of formation for a molecular species is zero at 298.15 K [33]. The well-known thermodynamic relationships with the specific heat at constant pressure, C_p , and the ratio of specific heats, γ , are given by

$$C_v = C_p - R \quad \gamma = \frac{C_p}{C_v} \quad (3.20)$$

The specific heats are formally defined as follows

$$C_p = \left(\frac{\partial h}{\partial T} \right)_p \quad C_v = \left(\frac{\partial e}{\partial T} \right)_v \quad (3.21)$$

These relate the heat added to the resulting change in temperature for systems at constant pressure and constant volume, respectively. At this point, the treatment of the specific heats must be placed in two separate categories. The first is the assumption of a calorically perfect gas, which states that the specific heats are constant [32] and therefore the following relations hold

$$h = C_p T \quad e = C_v T \quad (3.22)$$

Although this assumption may be adequate for subsonic and low supersonic flows, it is known that air is calorically imperfect at the elevated temperatures found in hypersonic flows [34]. One must therefore use a thermally perfect gas model that assumes the specific heats to be temperature dependent. This representation of the specific heats in conjunction with the assumption of a gas that obeys the ideal gas law defines what is known as a semi-perfect gas (often referred to as a thermally perfect gas) [35].

The solution of the governing equations is carried out using the conservative variables. To obtain the temperature, which is required by many other equations in the model, an iterative

Newton-Raphson procedure is used to invert the expressions for internal energy. Two different heat models are implemented in the present work for the representation of the internal energy of a high temperature gas.

3.2.1 Internal Energy Representation Using NASA Polynomials

From equation 3.21, we see that the specific heat capacities may be integrated to obtain the energy and enthalpy, as shown below

$$h(T) = \int_{T_{ref}}^T C_p(T) dT + h_f^{T_{ref}} \quad e(T) = \int_{T_{ref}}^T C_v(T) dT + h_f^{T_{ref}} \quad (3.23)$$

where $h_f^{T_{ref}}$ is the heat of formation, which is typically taken by convention to be at 298.15 K. These integrals were tabulated by NASA [33], who introduced the following standard polynomials

$$\begin{aligned} \frac{C_p(T)}{R} &= a_4 T^4 + a_3 T^3 + a_2 T^2 + a_1 T + a_0 + a_{-1} T^{-1} + a_{-2} T^{-2} \\ \frac{H^0(T)}{RT} &= a_1 + a_2 \frac{T}{2} + a_3 \frac{T^2}{3} + a_4 \frac{T^3}{4} + a_5 \frac{T^4}{5} + a_6 T^{-1} \\ \frac{S^0(T)}{R} &= a_1 \ln T + a_2 T + a_3 \frac{T^2}{2} + a_4 \frac{T^3}{3} + a_5 \frac{T^4}{4} + a_7 \end{aligned} \quad (3.24)$$

where $H^0(T)$ and $S^0(T)$ are the absolute enthalpy and entropy, which account for the heats of formation. It is important to note that by convention, the heats of formation of molecular species are zero at the reference temperature, while they are non-zero for atomic species.

3.2.2 Internal Energy Representation Using Boltzmann Energy Distribution

Another method to model the internal energy that is often used when the flow is assumed to be in thermal non-equilibrium is to split the contributions from each internal energy mode [22]. By the equipartition theorem, the internal energy of a particle is given by the summation of its average translational, rotational, vibrational and electronic energies, as shown in Figure 3.1.

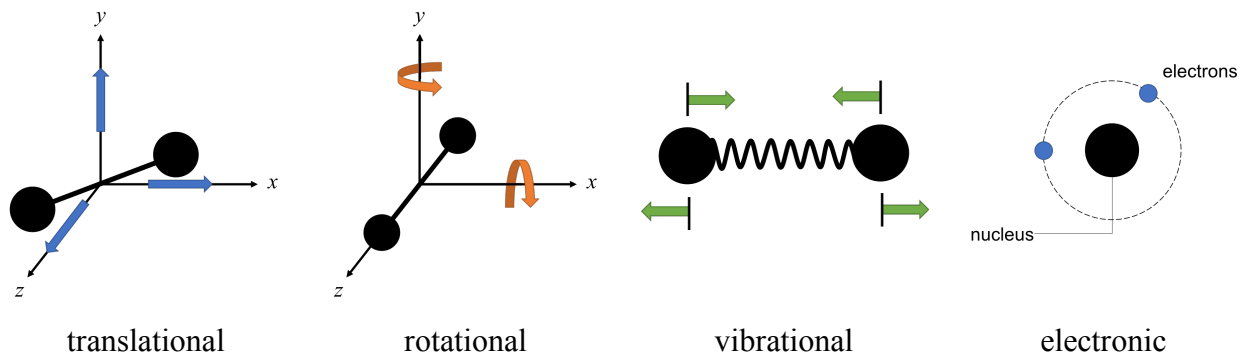


Figure 3.1 - Internal energy modes of a gas

The theorem assumes that the number densities of particles in each excitation mode follow a Maxwell-Boltzmann distribution. Although this approach allows flexibility in how to define the average energy of each mode, simplifications are often made for practical purposes. In the current work, the vibrational energy mode is modeled using a harmonic oscillator, since anharmonic effects may be neglected at low vibrational energies [22]. The electronic energy is computed by summing over observed energy level data for each species.

3.2.3 Comparison of Internal Energy Models

It is important to compare the thermodynamic models to understand their relative errors. The internal energy computed using each thermodynamic model is shown in Figure 3.2. These computations assume a state of thermodynamic equilibrium (all energy levels described by a single temperature), a frozen air composition of $X_{N_2} = 0.79$ and $X_{O_2} = 0.21$ and a freestream pressure of 101325 Pa. The internal energy obtained assuming a calorically perfect gas is linear and severely underestimates the actual energy content of the gas. The thermally perfect gas models are all quite close to each other up to roughly 10000 K, beyond which they begin to diverge. The full Boltzmann model and the polynomial models agree well, while the Boltzmann model neglecting electronic energy underestimates the others. It can therefore be said that for flows with negligible ionization and relatively low temperatures ($T < 10000$ K), any thermally perfect model is sufficient and will produce minimal errors. Finally, the energy of the gas is negative at temperatures lower than T^{ref} due to the convention that $h(T^{ref}) = 0$ for molecular species.

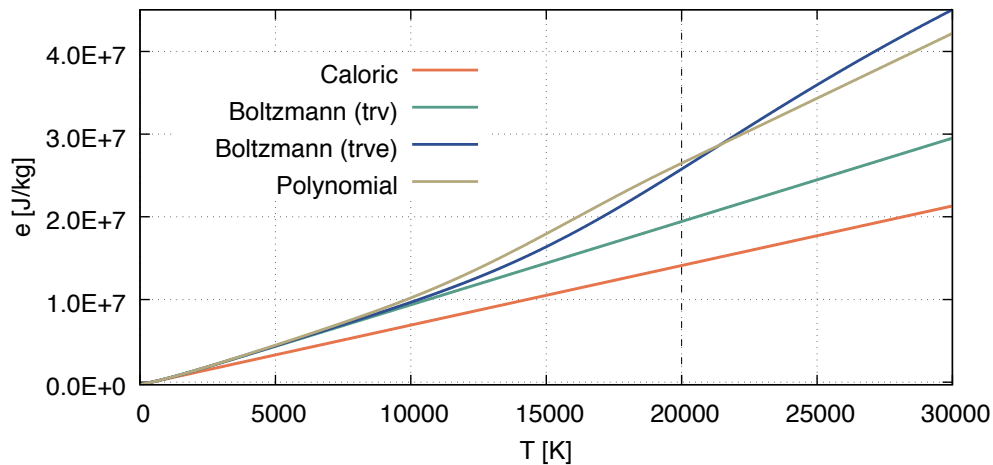


Figure 3.2 - Internal energy of frozen air in thermodynamic equilibrium versus temperature using various thermodynamic models

The constant volume specific heats are plotted in Figure 3.3. The calorically perfect model has a constant value, and the thermally perfect models begin to diverge from the calorically perfect assumption very early on ($T \approx 1000$ K). Since the chemically frozen air is entirely composed of molecular species, the inclusion of a vibrational contribution makes a significant difference. The electronic contribution must also not be ignored for temperatures above roughly 5000 K, as it can be seen that the polynomial and full Boltzmann models begin to diverge from the simplified Boltzmann model. The full Boltzmann and polynomial models are relatively similar, though the latter is constant above 20000 K since this is above the range of validity for the polynomial fit [33].

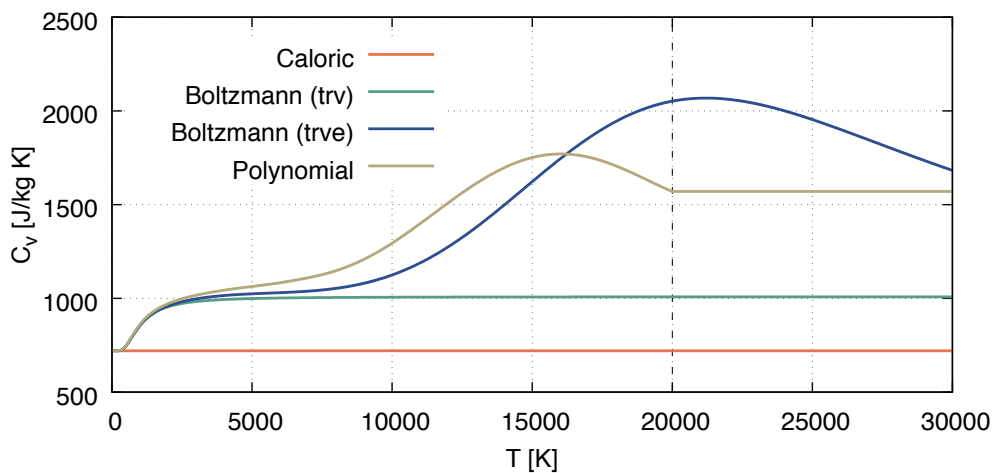


Figure 3.3 - Constant volume specific heat of frozen air in thermodynamic equilibrium versus temperature using various thermodynamic models

3.3 Mixture Transport Coefficients

The simulation of viscous flows requires values for various transport properties such as viscosity and thermal conductivity. Once again, variations in the fluid composition have a significant impact on the overall mixture properties and therefore must be taken into consideration. The mixture properties are therefore computed as a weighted summation of the individual species properties using Wilke's mixing rule [26], as follows:

$$\mu = \sum_{s=1}^{N_s} \frac{X_s \mu_s}{\phi_s} \quad \text{and} \quad \kappa = \sum_{s=1}^{N_s} \frac{X_s \kappa_s}{\phi_s} \quad (3.25)$$

where μ_s and κ_s are the species viscosity and thermal conductivity, respectively, and ϕ_s is the scaling factor, given by

$$\phi_s = \sum_{i=1}^{N_s} X_i \left[1 + \sqrt{\frac{\mu_s}{\mu_i}} \left(\frac{M_i}{M_s} \right)^{\frac{1}{4}} \right]^2 \left[\sqrt{8 \left(1 + \frac{M_s}{M_i} \right)} \right]^{-1} \quad (3.26)$$

Various options for computing the species viscosity and thermal conductivity are implemented and will be discussed below.

3.3.1 NIST Least-squares Polynomials

Gordon and McBride [33] provide curve fits of experimental data for the species viscosity and thermal conductivities, shown below

$$\left. \begin{array}{l} \ln \mu_s \\ \ln \kappa_s \end{array} \right\} = A_s \ln T + \frac{B_s}{T} + \frac{C_s}{T^2} + D_s \quad (3.27)$$

where A_s , B_s , C_s and D_s are tabulated values from experimental data fits of the viscosity or conductivity of various species. For flows in thermal equilibrium there is no need to split the thermal conductivity into its translational-rotational and vibrational components, as done in the following model.

3.3.2 Blottner Viscosity and Eucken Conductivity

A common representation of viscosity is given by Blottner's curve fit [26], expressed as follows

$$\mu_s = 0.1 \exp[(A_s \ln T + B_s) \ln T + C_s] \quad (3.28)$$

Eucken's relation considers the thermal conductivity to be the sum of a trans-rotational and a vibrational contribution as shown below

$$\kappa_{s,tr} = \mu_s \left(\frac{5}{2} C_{v,t,s} + C_{v,r,s} \right) \quad \kappa_{s,ve} = \begin{cases} \mu_s C_{v,ve,s} & \text{molecules} \\ 0 & \text{atoms} \end{cases} \quad (3.29)$$

The vibrational contribution to the thermal conductivity must be computed for flows that include thermal non-equilibrium and therefore this option is nearly ubiquitous for non-equilibrium simulations.

3.3.3 Sutherland's Law

For frozen flows in thermal non-equilibrium at low temperatures, Sutherland's law is implemented, shown below.

$$\frac{\mu}{\mu_{ref}} = \frac{T_{ref} + S}{T + S} \left(\frac{T}{T_{ref}} \right)^n \quad (3.30)$$

where T_{ref} , S , n and μ_{ref} are gas dependent parameters. The same expression may be used for the thermal conductivity with different parameters. In this work the standard parameters for air are used, resulting in the following

$$\frac{\mu}{\mu_{ref}} = \frac{(1.458E - 06)T^{3/2}}{T + 110}, \quad \frac{\kappa}{\kappa_{ref}} = \frac{(2.162E - 03)T^{3/2}}{T + 133.7} \quad (3.31)$$

Individual species properties may be computed using Sutherland's formula and subsequently mixed using Wilke's rule. However, due to the greater availability of data, the Blottner and NIST models are used for flows in chemical non-equilibrium.

3.3.4 Comparison of Transport Property Models

For the sake of completeness, the various models for viscosity and thermal conductivity are plotted in Figure 3.4 and Figure 3.5, respectively, for a frozen air mixture in thermal equilibrium. The gas is assumed to be comprised of 79% nitrogen and 21% oxygen by volume and the pressure is 101325 Pa. It is evident that Sutherland's law results in a much lower

viscosity and thermal conductivity than is predicted from the other models shown. Furthermore, it is seen that Blottner's model is reasonably close to the NIST polynomial, but Eucken's relation tends to result in lower values than NIST for the thermal conductivity.

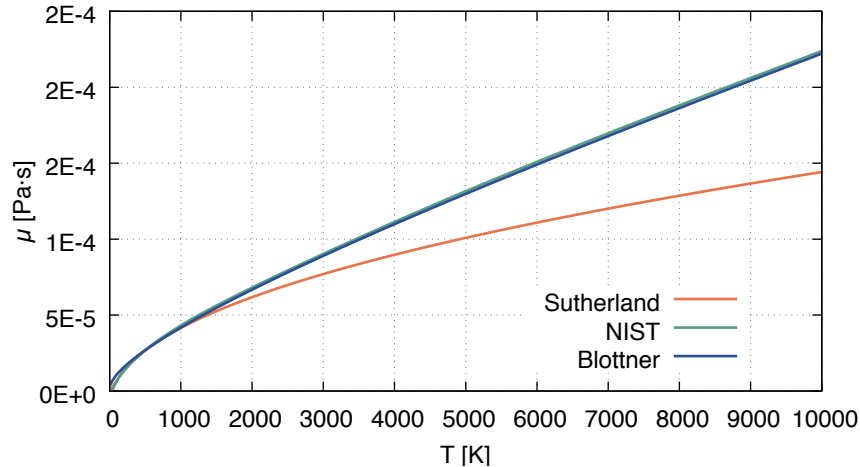


Figure 3.4 - Dynamic viscosity of frozen air using various transport property models

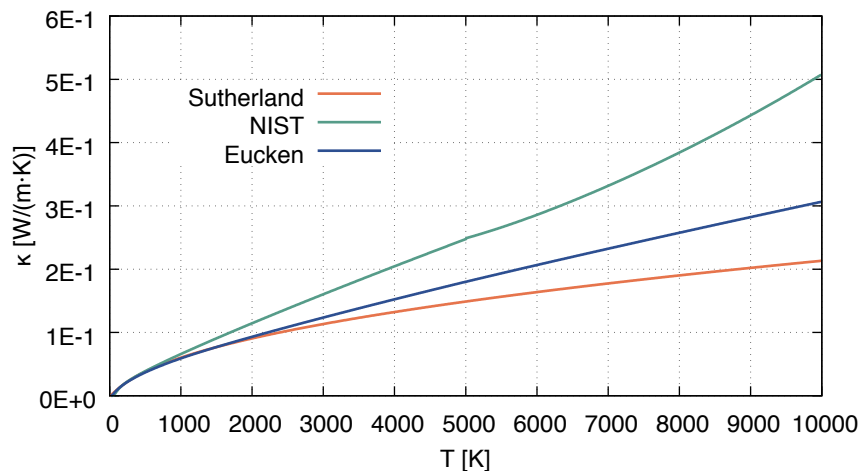


Figure 3.5 - Thermal conductivity of frozen air using various transport property models

3.4 Chemical Kinetics Model

As discussed in Section 2.2, the chemical non-equilibrium regime is of interest for many hypersonic applications. As such, a kinetic model must be used to account for the effect of chemical reactions on the production and destruction of species. In the present work, a laminar finite-rate chemistry model is used that assumes the reactions follow simple Arrhenius kinetics and ignores the effect of turbulent fluctuations in the flow. An equilibrium chemistry solver was

also developed (presented in Appendix D) to address equilibrium-type boundary conditions and provide a point of comparison in future developments. Consider a reversible reaction of the form



where the lowercase letters are stoichiometric coefficients for a balanced reaction and the uppercase letters are molar amounts of the participating chemical species. The *Law of Mass Action* [36] states that an equilibrated system at a given temperature yields the following relation

$$K_{eq} = \frac{[C]^c [D]^d}{[A]^a [B]^b} \quad (3.33)$$

where K_{eq} is the equilibrium constant and the bracketed terms represent molar concentrations. If we subsequently define the forward and backward rate coefficients k_f and k_b as follows

$$K_{eq} = \frac{k_f}{k_b} \quad (3.34)$$

then a general system of N_r chemical reactions involving N_s chemical species can be represented in the following form

$$\sum_{s=1}^{N_s} v'_{r,s} [X_s] \rightleftharpoons \sum_{s=1}^{N_s} v''_{r,s} [X_s] \quad \forall r \in [1, N_r] \quad (3.35)$$

where $[X_s]$ are the species concentrations and v'_s and v''_s are the reactants and products stoichiometric coefficients, respectively. The rate of change of each species due to a reaction is the summation of the forward and backward rates of progress

$$\frac{d[X_s]_r}{dt} = \frac{d[X_s]_{f,r}}{dt} - \frac{d[X_s]_{b,r}}{dt} \quad (3.36)$$

The terms on the right-hand-side are known as the forward and backward rates of progress of species s due to reaction r and can be expressed as follows

$$\begin{aligned} \frac{d[X_s]_{f,r}}{dt} &= (v''_{s,r} - v'_{s,r}) R_{f,r} \\ \frac{d[X_s]_{b,r}}{dt} &= (v'_{s,r} - v''_{s,r}) R_{b,r} \end{aligned} \quad (3.37)$$

where $R_{f,r}$ and $R_{b,r}$ are the forward and backward reaction rates, respectively. These reaction rates are products of the species molar concentrations raised to their stoichiometric coefficients and the forward and backward reaction rate coefficients, respectively, as shown below

$$R_{f,r} = k_{f,r} \prod_{i=1}^{N_s} [X_i]^{v'_{i,r}}, \quad R_{b,r} = k_{b,r} \prod_{i=1}^{N_s} [X_i]^{v''_{i,r}} \quad (3.38)$$

From these expressions, the equation for the mass source term of species s is given by

$$\dot{\omega}_s = M_s \sum_{r=1}^{N_r} (v'_{s,r} - v''_{s,r}) (R_{f,r} - R_{b,r}) \quad (3.39)$$

where M_s is the species molar mass and N_r is the number of chemical reactions. The final step in defining the finite-rate chemistry model is to provide expressions for the forward and backward reaction rates. The forward reaction rate coefficient is usually modeled using the modified Arrhenius equation

$$k_{f,r}(\bar{T}_c) = A_{f,r} \bar{T}_c^{\eta_{f,r}} \exp\left(-\frac{E_{a,r}}{R_u \bar{T}_c}\right) \quad (3.40)$$

where $A_{f,r}$, $\eta_{f,r}$ and $E_{a,r}/R_u$ are reaction-specific parameters found in the literature and \bar{T}_c represents the corrected rate-controlling temperature, which will be discussed in Section 3.6. Note that reaction set data is commonly given in the CGS unit system. Using equation 3.34 we can determine $k_{b,r}$ by providing an appropriate expression for $K_{eq,r}$. Two options are implemented in the solver and will be discussed below.

3.4.1 Equilibrium Rate Constant via Polynomials

Many experiments have been conducted to measure reaction rate coefficients for various temperature ranges. Polynomial fits can be applied to this experimental data to obtain a continuous representation as a function of temperature. Since there is a variety of polynomial forms, a general polynomial is implemented into the code, shown below

$$K_{eq,r}(\bar{T}) = \exp\left(B_{r,1} \left(\frac{1}{Z^2}\right) + B_{r,2} \left(\frac{1}{Z}\right) + B_{r,3} + B_{r,4}Z + B_{r,5}Z^2 \right. \\ \left. + B_{r,6}Z^3 + B_{r,7}Z^4 + B_{r,8} \log(Z) + B_{r,9} \log\left(\frac{1}{Z}\right) \right) \quad (3.41)$$

where $z = 10000/\bar{T}$. Many researchers rely on these polynomials due to their simplicity and their applicability regardless of assumptions on the representation of internal energy.

3.4.2 Equilibrium Rate Constant via Gibbs Free Energy

The equilibrium constant can also be calculated based on thermodynamic principles. The equilibrium constant in pressure units is given by

$$K_{p,r} = \exp\left(-\frac{\Delta G_r}{R_u T}\right) \quad (3.42)$$

The Gibbs function ΔG_r is computed as

$$\Delta G_r = \sum_{s=1}^{N_s} \nu_{s,r} G_s, \quad G_s(T) = H_s(T) - TS_s(T) \quad (3.43)$$

where $H_s(T)$ and $S_s(T)$ can be obtained using the NASA polynomials. The equilibrium constant in concentration units is subsequently computed as follows

$$K_{eq,r} = K_{p,r} \left(\frac{p_{atm}}{R_u T}\right)^{\nu_r}, \quad \text{with } \nu_r = \sum_{s=1}^{N_s} \nu_{s,r} \quad (3.44)$$

This formulation has the advantage of being an exact expression when using the polynomial thermodynamic model. However, if a different thermodynamic formulation is used, the Gibbs function may not be readily computed.

3.4.3 Comparison of Reaction Schemes

As previously stated, the comparison and analysis of reaction rates is essential for aerothermodynamic predictions of chemically reacting flow fields. Experimental reaction rates typically have large scatter in the literature and are sometimes used outside of their range of applicability [15]. The forward reaction rate coefficients and equilibrium rate constants for the dissociation of nitrogen and oxygen are plotted in Figure 3.6 and Figure 3.7, respectively.

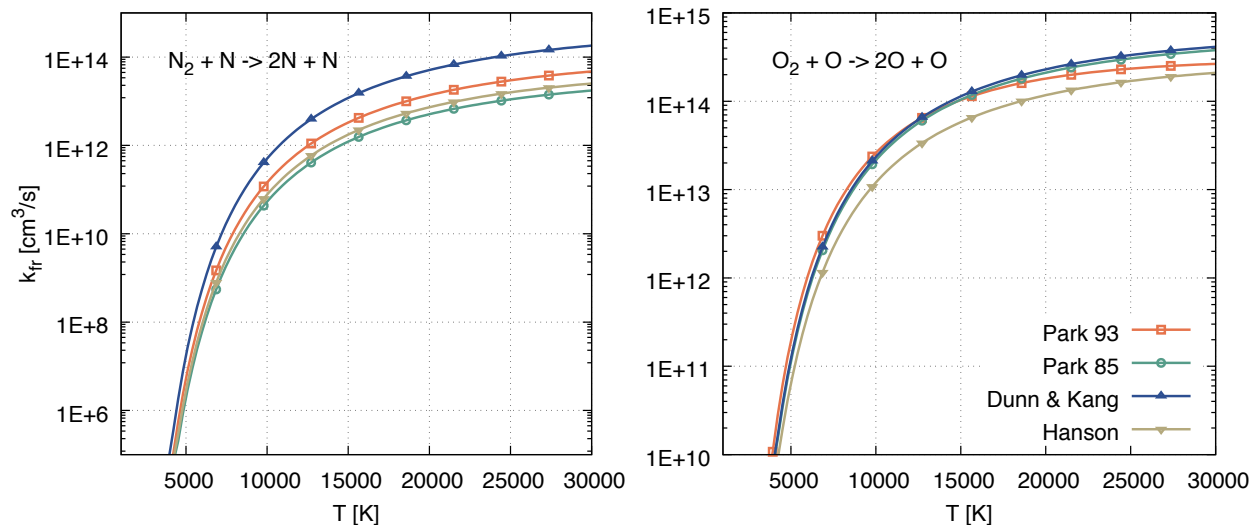


Figure 3.6 - Forward reaction rate coefficients for nitrogen (left) and oxygen (right) dissociation using various reaction schemes

The Park 1993 [37], Park 1985 [21], Dunn & Kang [38], and Hanson [39] models are compared. Note that both Park models use polynomial formulations to compute the equilibrium constant, while the Dunn & Kang model provides the backward reaction rate coefficient as an Arrhenius expression. Furthermore, Hanson's model does not provide data for the equilibrium constant, instead opting to use Park's polynomial fits. The analytical equilibrium constant obtained using Gibbs' free energy is also shown. The purpose of this comparison is not to extrapolate any conclusions on the behavior of an entire reaction scheme based on data for a single reaction, but rather to demonstrate the variance in the data. In general, it can be seen that the rate coefficients may differ by several orders of magnitude from each other, and this difference increases with temperature, indicating the limited range of validity of the schemes. The analytical equilibrium constant generally agrees well with the other schemes, demonstrating its suitability. Note that although the equilibrium constants agree well with each other for moderately low temperatures, discrepancies in forward reaction rate coefficients will nevertheless translate to differences in backward rate coefficients.

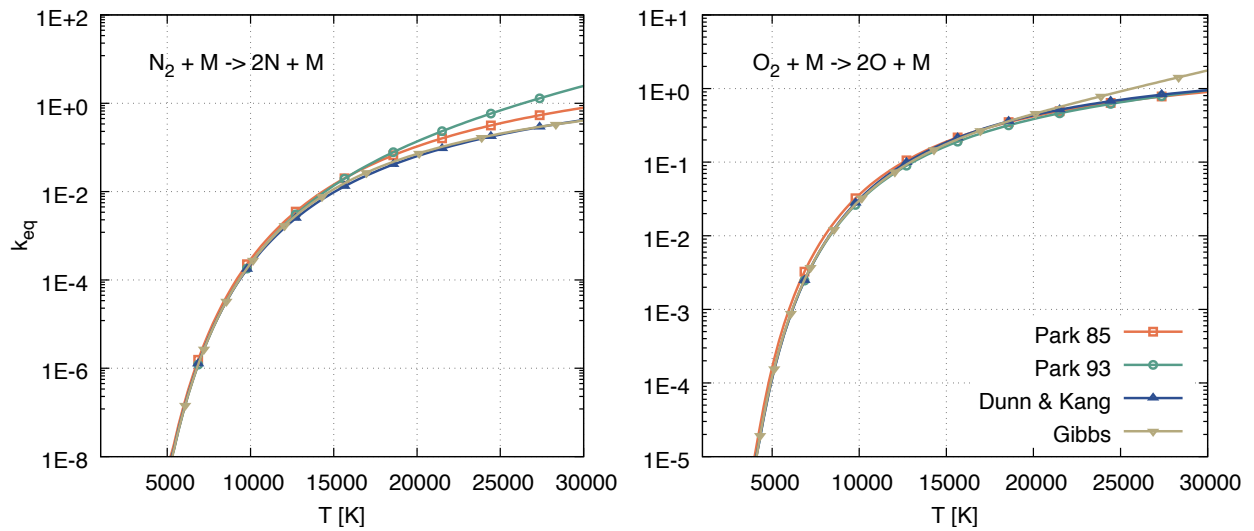


Figure 3.7 - Equilibrium rate constants for nitrogen (left) and oxygen (right) dissociation using various reaction schemes and the analytical (Gibbs) formulation

Stability Corrections

At low temperatures, the equilibrium rate constant expressions may be extremely ill-conditioned since they have a specific range of validity. Furthermore, as the temperature tends to zero, the equilibrium constant tends to zero, which may lead to numerical errors when computing the backward reaction rate coefficient. Therefore, for numerical purposes, the following cutoff is applied to the temperature to avoid a division by zero error when computing the backward rate coefficient

$$\bar{T}(T) = \frac{1}{2} \left((T + T_{min}) + \sqrt{(T + T_{min})^2 + \epsilon^2} \right) \quad (3.45)$$

where the parameters $T_{min} = 700$ and $\epsilon = 70$ are typically used. A soft cutoff is used to ensure a smooth derivative of the residual, which is required by Newton's method. This correction is deemed acceptable, since the reactions of interest have low rates at temperatures below 700 K.

3.5 Thermodynamic Non-equilibrium

3.5.1 Two-temperature Model

In the current work, a two-temperature model is adopted, which assumes that the translational and rotational energy modes are in equilibrium and can therefore be defined by the same temperature, T_{tr} . This assumption is valid as these energy modes are fully excited at very

low temperatures. Furthermore, it is assumed that the vibrational and electronic energy modes are in equilibrium and may be described by a common temperature T_{ve} . This is an adequate model for most hypersonic applications, as the vibrational energy states are typically in equilibrium with each other, and the higher electronic states may be assumed to be in equilibrium with the vibrational mode, as they are negligible [20]. Adopting a Boltzmann approach, the internal energy of a given species is

$$e_s(T_{tr}, T_{ve}) = e_{s,t}(T_{tr}) + e_{s,r}(T_{tr}) + e_{s,v}(T_{ve}) + e_{s,e}(T_{ve}) + e_{s,f}^0 \quad (3.46)$$

where $e_{s,t}$ is the translational energy, $e_{s,r}$ is the rotational energy, $e_{s,v}$ is the vibrational energy and $e_{s,e}$ is the electronic energy. Assuming a Maxwell-Boltzmann energy distribution for each individual energy mode, statistical mechanics may be used to obtain the following expressions for the translational and rotational constant-volume specific heats

$$e_{s,t} = C_{v,t,s} T_{tr} = \frac{3 R_u}{2 M_s} T_{tr} \quad e_{s,r} = \begin{cases} C_{v,r,s} T_{tr} = \frac{R_u}{M_s} T_{tr} & \text{molecules} \\ 0 & \text{atoms} \end{cases} \quad (3.47)$$

The vibrational energy for molecules is modelled assuming a harmonic oscillator, shown below

$$e_{s,v} = \begin{cases} R_s \frac{\theta_{v,s}}{\exp(\theta_{v,s}/T_{ve}) - 1} & \text{molecules} \\ 0 & \text{atoms} \end{cases} \quad (3.48)$$

where $\theta_{v,s}$ is the characteristic vibrational temperature of the species. The expression of species electronic energy is given by

$$e_{s,el} = \begin{cases} R_s \frac{\sum_{i=1}^N g_{i,s} \theta_{el,i,s} \exp(-\theta_{el,i,s}/T_{ve})}{\sum_{i=0}^N g_{i,s} \exp(-\theta_{el,i,s}/T_{ve})} & \text{molecules and atoms} \\ 0 & \text{electrons} \end{cases} \quad (3.49)$$

where $\theta_{el,i}$ and g_i is the characteristic electronic temperature and degeneracy of the i -th level, respectively. The constant volume heat capacities of the vibrational and electronic energy modes may be obtained as

$$C_{v,v,s} = \frac{\partial e_{s,v}}{\partial T_{tr}}, \quad C_{v,el,s} = \frac{\partial e_{s,el}}{\partial T_{ve}} \quad (3.50)$$

The full expressions may be found in [41]. As for the translational temperature, the vibrational-electronic temperature is obtained using a Newton-Raphson procedure on the vibrational-electronic energy.

3.5.2 Vibrational-electronic Energy Relaxation

To complete the non-equilibrium modeling, the expression of the vibrational-electronic energy source term must be discussed. In the current work, the source term is comprised of two terms, shown below

$$\dot{\omega}_{ve} = Q_{T-V} + Q_{V-D} \quad (3.51)$$

where Q_{T-V} models the relaxation between the translation and vibrational energy modes and Q_{V-D} models the production or destruction of vibrational energy due to the changes in gas composition because of chemical reactions. The latter term will be discussed in the next section. The translational-vibrational relaxation term is given by

$$Q_{T-V} = \sum_{s=1}^{N_s} \rho_s \frac{e_{s,ve}(T_{tr}) - e_{s,ve}(T_{ve})}{\tau_s^{LT}} \quad (3.52)$$

where τ_s^{LT} is the Landau-Teller relaxation time [34], given by

$$\tau_s^{LT} = \frac{\sum_{i=1}^{N_s} X_i}{\sum_{i=1}^{N_s} X_i / \tau_{si}^{LT}} \quad (3.53)$$

The interspecies Landau-Teller relaxation time τ_{si}^{LT} is obtained using the semi-empirical formula of Millikan and White as follows

$$\tau_{si}^{LT} = \frac{p_{atm}}{p} \exp[A_{si}(T_{tr}^{-1/3} - 0.015\mu_{si}^{1/4}) - 18.42] \quad (3.54)$$

The parameters used in the formula are

$$A_{si} = (1.16E - 03)\mu_{si}^{1/2}\theta_{vi}^{4/3} \quad (3.55)$$

$$\mu_{si} = \frac{M_s M_i}{M_s + M_i}$$

For relatively high temperatures (above roughly 8000 K), the expression above under-predicts the relaxation times [34]. The relaxation time is therefore modified as

$$\tau_{si}^{LT} = \tau_s^{LT} + \tau_s^P \quad (3.56)$$

Where τ_s^P is Park's correction based on experimental correlations, given by

$$\tau_s^P = \frac{1}{\sigma_s c_s N_s} \quad (3.57)$$

with the following variables defined as

$$\sigma_s = (1.0\text{E} - 21) \left(\frac{50000}{T_{tr}} \right)^2, \quad c_s = \sqrt{\frac{8R_u T_{tr}}{\pi M_s}}, \quad N_s = \frac{N_A \rho}{M} \quad (3.58)$$

3.6 Vibration-dissociation Coupling

It is known that dissociation-type reactions are strongly influenced by the vibrational energy mode, as a result of the vibrational ladder-climbing process [21]. Various models have been developed that modify the reaction rates given the thermal non-equilibrium state of the gas. These models also add a component to the vibrational-electronic source term to account for vibrational-electronic energy that is created or destroyed due to chemical reactions. Two models are considered in this work and are explained below.

3.6.1 Park's Rate-controlling Temperature Model

The most commonly used vibration-dissociation coupling method is the empirical Park model [21], which has shown good agreement with experimental data, despite its simplicity. Park defines a rate-controlling temperature T_c that is a blend of the translational-rotational and vibrational-electronic temperatures, as follows

$$T_c = T_{tr}^q T_{ve}^{1-q} \quad (3.59)$$

Originally, the rate exponent q was set to be 0.5, however it was later found that 0.7 yielded more favorable results [37]. This rate-controlling temperature is subsequently used to compute the forward reaction rate coefficient. Note that the backward reaction rate coefficient must still be computed using the translational energy as follows

$$k_{b,r}(\bar{T}_{tr}) = \frac{k_{f,r}(\bar{T}_{tr})}{K_{eq,r}(\bar{T}_{tr})}, \quad k_{f,r}(\bar{T}_c) = A_{f,r} \bar{T}_c^{\eta_{f,r}} \exp\left(-\frac{E_{a,r}}{R_u \bar{T}_c}\right) \quad (3.60)$$

The creation or destruction of molecular species in turn increases or decreases the vibrational-electronic energy of the mixture. Park's model accounts for this through the following source term

$$Q_{C-v} = \sum_{m=1}^{N_m} \dot{\omega}_m D'_m \quad (3.61)$$

where N_m represents the number of molecules and D'_m is the produced vibrational energy, for which two models are available. The non-preferential model assumes that molecules are created at the average vibrational energy, while the preferential model assumes that molecules are created at lower vibrational energy states, as shown below

$$D'_s = \begin{cases} e_{s,ve}(T_{ve}) & \text{non - preferential} \\ \alpha_s D_s & \text{preferential} \end{cases} \quad (3.62)$$

where D_s is the dissociation potential of the chemical species and α_s is a fractional number typically taken as 0.3.

3.6.2 Coupled Vibration-dissociation-vibration Model

Treanor and Maronne proposed the coupled vibration-dissociation-vibration model (CVDV) which assumes that more molecules are formed in upper vibrational levels [42]. In this model the forward reaction rate coefficient is modified by a coupling factor V as follows

$$\tilde{k}_{f,r} = V k_{f,r}(T_{tr}), \quad V = \frac{Z(T_{tr})Z(T_{F,m})}{Z(T_{ve})Z(-U_m)} \quad (3.63)$$

where m is an index representing the dissociating molecule, and

$$U_m = \frac{E_{a,r}}{3k_B}, \quad T_{F,m}^{-1} = \frac{1}{T_{ve}} - \frac{1}{T_{tr}} - \frac{1}{U_m} \quad (3.64)$$

The vibrational partition function Z computes the cumulative energy of each vibrational energy level modeled as a harmonic oscillator as follows

$$Z(T) = \sum_{\alpha=0}^N \exp\left(-\frac{\epsilon_{\alpha,m}}{k_B T}\right) \quad (3.65)$$

where α is a positive integer representing the vibrational energy level, N is a cutoff parameter, and $\epsilon_{\alpha,m}$ is the energy of the α -th energy level given by

$$\epsilon_{\alpha,m} = \alpha k_B \theta_{v,m} \quad (3.66)$$

Finally, to model the vibrational energy produced by the chemical reactions, we can separate the influence of the vibration-coupled forward reactions and the standard backward reactions as follows

$$Q_{C-V} = \sum_{m=1}^{N_m} \frac{1}{M_m} [\bar{E}(T_{tr}, T_{ve}) \dot{\omega}_{f,m} + \bar{E}(T_{tr}, T_{tr}) \dot{\omega}_{b,m}] \quad (3.67)$$

where

$$\begin{aligned} \bar{E}(T_{tr}, T_{ve}) &= \frac{1}{Z(T_{F,m})} \sum_{\alpha=0}^N \epsilon_{\alpha,m} \exp\left(-\frac{\epsilon_{\alpha,m}}{k_B T_F}\right) \\ \bar{E}(T_{tr}, T_{tr}) &= \frac{1}{Z(-U_m)} \sum_{\alpha=0}^N \epsilon_{\alpha,m} \exp\left(-\frac{\epsilon_{\alpha,m}}{k_B U}\right) \end{aligned} \quad (3.68)$$

3.6.3 Comparison of Vibration-dissociation Coupling Models

The coupling factor V may be used to quantify the influence of the chosen vibration-dissociation coupling model on the computed reaction rate coefficient. The forward reaction rate coefficients for a nitrogen dissociation reaction is computed under the assumption of thermodynamic equilibrium at $T = 20000$ K. The reaction rate coefficient is then computed assuming thermodynamic non-equilibrium using the various coupling models and the coupling factor is subsequently calculated. The Park 93 reaction scheme is used. The results are shown in Figure 3.8.

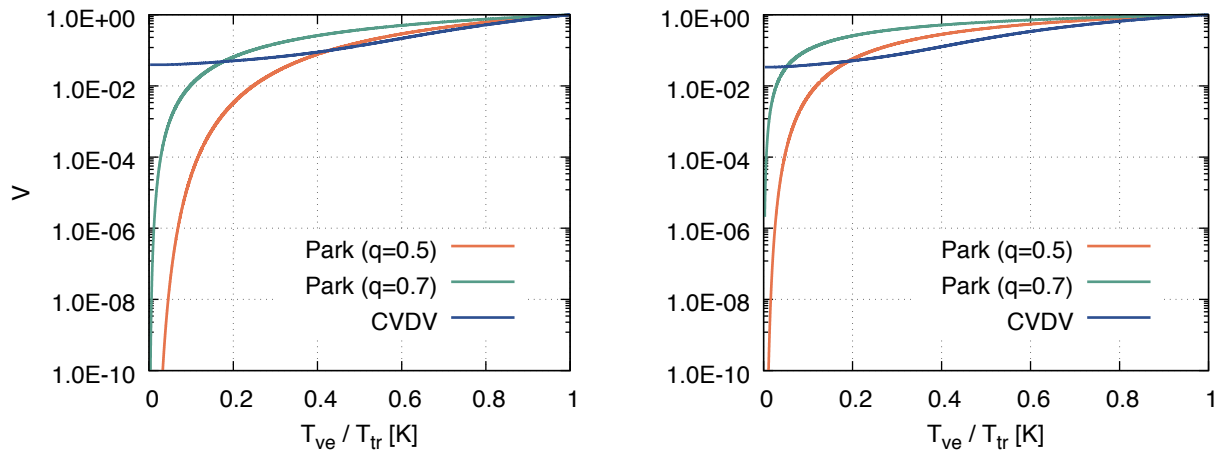


Figure 3.8 - VD coupling factor for nitrogen (left) and oxygen (right) dissociation reactions using various coupling models

The coupling factor approaches unity as T_{ve}/T_{tr} does, since the gas approaches thermal equilibrium. It is shown that Park's model predicts extremely strong coupling the further a gas is from thermodynamic equilibrium. A rate exponent that is closer to unity ($q = 0.7$) predicts weaker coupling. The CVDV model tends to predict coupling slightly stronger than Park's original model when close to thermodynamic equilibrium. As the level of non-equilibrium increases, however, the CVDV model does not stray significantly like Park's model.

3.7 Chemical Diffusion

Molecular diffusion is an extremely complex process that can occur due to a variety of factors, such as concentration, pressure and temperature gradients. To accurately model this complex phenomenon, the Stefan-Maxwell equations are used [36]. This is a coupled system of equations that must be solved spatially. For this reason, as well as the necessity of detailed diffusion data, a simplification is often made, known as Fick's law, which assumes a binary gas mixture and neglects thermal and pressure diffusion. This formulation is often used for multicomponent gas mixtures but does not ensure consistency. Fick's law provides the following diffusion flux for a single species

$$J_s = -\rho \sum_{i=1}^{N_s} \mathcal{D}_{s,i} \nabla Y_i \quad (3.69)$$

where $\mathcal{D}_{s,i}$ is the binary diffusivity for the interaction of species i and s . Although this accounts for the different diffusion speeds of each combination of species, a much simpler approach is to use the constant dilute approximation, which considers a single diffusion coefficient for all interactions. The diffusion coefficient may then be obtained by assuming a constant Lewis number Le , shown below

$$D = \frac{Le\kappa_{tr}}{\rho C_{p,tr}} \quad (3.70)$$

The Lewis number is typically taken as a constant number between 1.0 and 1.4. Another model considers a constant Schmidt number, as

$$D = \frac{\mu}{\rho Sc} \quad (3.71)$$

where the Schmidt number may be anywhere from 0.1 to 1.0. These approximations are useful both due to their simplicity as well as the fact that they render the diffusion coefficient matrix a scalar. Thus, the summation of diffusion fluxes becomes

$$\sum_{s=1}^{N_s} -\rho D \nabla Y_s = -\rho D \sum_{s=1}^{N_s} \nabla Y_s \equiv 0, \quad \text{since } \nabla Y_s = 0 \quad (3.72)$$

Therefore, the summation of species transport equations equals the total mass conservation equation, ensuring consistency.

When species diffusion occurs, the molecules or atoms carry energy as well as mass. Consequently, variations in composition also cause variations in internal energy. The species mass diffusion therefore has a counterpart in the total energy equation, known as the inter-diffusional heat flux, given by the following expression

$$\mathbf{q}^{D,E} = \sum_{s=1}^{N_s} h_s \mathbf{J}_s \quad (3.73)$$

Although the summation of mass fluxes should be zero, the above term is still non-zero, as it is weighted by the species enthalpies. The internal enthalpy of each species, h_s , is used as opposed to the internal energy, since it is assumed that the diffusive velocities of each species are

negligible. Similarly, species diffusion is also accounted for in the vibrational-electronic energy equation with the inter-diffusional vibrational-electronic energy flux, shown below

$$\mathbf{q}^{D,VE} = \sum_{s=1}^{N_s} e_{s,ve} \mathbf{J}_s \quad (3.74)$$

The consideration of these terms is essential to prevent local violations of the entropy condition in mixing regions [43].

4 Numerical Modeling

4.1 Finite Element Discretization

Let the governing equations be defined on a complete closed domain $\bar{\Omega} = \Omega \cup \Gamma$, where Ω is the open domain, Γ is the boundary and $\bar{\Omega} \in \mathbb{R}^n$. The first step in the FEM is subdividing the domain into a non-overlapping set of N_e finite elements, known as a tessellation, as follows

$$\Omega^h \approx \bigcup_{i=1}^{N_e} \Omega_i^e, \quad \Omega^h \subset \bar{\Omega} \quad (4.1)$$

where Ω^e is an element. Subsequently, we assume that a dependent unknown variable vector Q can be approximated over a generic element as follows

$$Q(t, \mathbf{x}) = \sum_{j=1}^{N_n} N_j(\mathbf{x}) Q_j(t) \quad (4.2)$$

where N_j is the piece-wise linear Lagrangian shape function of the node, N_n is the number of nodes in the element and Q_j is the vector of variable values at a given node. Similar approximations are obtained for \mathbf{F} and S . Two important properties hold for shape functions, shown below

$$N_i(x_j) = \delta_{ij} \quad \text{and} \quad \sum_{i=1}^{N_n} N_i(x_j) = 1 \quad (4.3)$$

where δ_{ij} is the Kronecker delta, defined as

$$\delta_{ij} = \begin{cases} 1 & \text{if } i = j \\ 0 & \text{if } i \neq j \end{cases} \quad (4.4)$$

Much of the power and flexibility of the FEM arises from being able to use a wide variety of elements with shape functions that satisfy the continuity requirements of the governing equations. The discretization will necessitate the evaluation of several integrals. These can be exactly evaluated if the function is represented by a polynomial using the following quadrature

$$\int_{-1}^1 f(x) dx = \sum_{i=1}^n w_i f(x_i) \quad (4.5)$$

where $f(x)$ is the function to be integrated, w_i is the Gauss weight and n is the number of Gauss points. This rule can yield an exact result for polynomials of degree $2n - 1$ or less [43]. The Gauss weights and locations w_i and x_i are tabulated for the standard interval $[-1,1]$, and therefore it is convenient to introduce local coordinates ζ , η and χ . The local coordinates are related to the global coordinates as follows

$$\begin{Bmatrix} \frac{\partial N_i}{\partial \zeta} \\ \frac{\partial N_i}{\partial \eta} \\ \frac{\partial N_i}{\partial \chi} \end{Bmatrix} = \begin{bmatrix} \frac{\partial x}{\partial \zeta} & \frac{\partial y}{\partial \zeta} & \frac{\partial z}{\partial \zeta} \\ \frac{\partial x}{\partial \eta} & \frac{\partial y}{\partial \eta} & \frac{\partial z}{\partial \eta} \\ \frac{\partial x}{\partial \chi} & \frac{\partial y}{\partial \chi} & \frac{\partial z}{\partial \chi} \end{bmatrix} \begin{Bmatrix} \frac{\partial N_i}{\partial x} \\ \frac{\partial N_i}{\partial y} \\ \frac{\partial N_i}{\partial z} \end{Bmatrix} = J \begin{Bmatrix} \frac{\partial N_i}{\partial x} \\ \frac{\partial N_i}{\partial y} \\ \frac{\partial N_i}{\partial z} \end{Bmatrix} \quad (4.6)$$

where J is the element Jacobian matrix. Since the elemental shape functions N are given for many types of elements in local coordinates and the global coordinates of the element are known a priori, the Jacobian matrix is readily computed. Upon integration, we may introduce the following change of variables

$$dV = J d\zeta d\eta d\chi \quad (4.7)$$

The evaluation of a volume integral using Gaussian quadrature therefore becomes

$$\iiint F(\zeta, \eta, \chi) dV = \sum_i \sum_j \sum_k W_i W_j W_k F(\zeta, \eta, \chi) J \quad (4.8)$$

and similar for surface integrals.

The governing equations are solved in an average sense over the domain using the weighted residual method. We introduce suitable weight functions W_i and integrate by parts to obtain the weak formulation of the species transport equation

$$\int_{\Omega} W_i \frac{\partial \rho Y_s}{\partial t} - \int_{\Omega} \nabla W_i (\rho Y_s \mathbf{V} - \mathbf{J}_s) + \int_{\Gamma} W_i \mathbf{n} (\rho Y_s \mathbf{V} - \mathbf{J}_s) - \int_{\Omega} W_i \dot{\omega}_s = 0 \quad (4.9)$$

This is known as the weak formulation as the equality is satisfied in an integral sense. Substituting the discrete representation of the unknown variables we obtain

$$\begin{aligned}
 \sum_{j=1}^{N_n} \int_{\Omega} W_i N_j \frac{d(\rho Y_s)_j}{dt} - \sum_{j=1}^{N_n} \int_{\Omega} N_j \nabla W_i \cdot (\rho Y_s \mathbf{V})_j + \int_{\Omega} \nabla W_i \cdot \mathbf{J}_s \\
 + \int_{\Gamma} W_i \mathbf{n} \cdot (\rho Y_s \mathbf{V} - \mathbf{J}_s) - \sum_{j=1}^{N_n} \int_{\Omega} W_i N_j (\dot{\omega}_s)_j = 0
 \end{aligned} \tag{4.10}$$

Note that the flux term is split into a domain contribution as well as a boundary contribution. In the Galerkin formulation the weight functions are equal to the shape functions, thus making $W_i = N_i$. This formulation provides the best approximation in the Rayleigh-Ritz energy norm [43]. The integration over Ω appearing in the equation above is replaced by a summation of the elements Ω^e of the mesh Ω^h , thanks to the local support of the shape functions. For each test function, we have

$$\begin{aligned}
 \sum_{e \in E_i} \sum_{j \in K_e} \int_{V^e} W_i N_j \frac{\partial(\rho Y_s)_j}{\partial t} dV - \sum_{e \in E_i} \sum_{j \in K_e} \int_{V^e} N_j \nabla W_i \cdot (\rho Y_s \mathbf{V})_j dV + \sum_{e \in E_i} \int_{V^e} \nabla W_i \cdot \mathbf{J}_s dV \\
 + \sum_{e \in F_i} \int_A W_i \mathbf{n} \cdot (\rho Y_s \mathbf{V} - \mathbf{J}_s) dA - \sum_{e \in E_i} \sum_{j \in K_e} \int_{V^e} W_i N_j (\dot{\omega}_s)_j dV = 0
 \end{aligned} \tag{4.11}$$

where E_i is the set of elements connected to the i -th node, F_i is the set of faces connected to the i -th node and K_e is the set of nodes belonging to the e -th element.

4.2 Edge-based Assembly

Although extensive development of FVM techniques for fluid dynamics problems has occurred due to their conservative properties and physical foundation, these techniques suffered from several drawbacks, such as inaccurate discretization of viscous fluxes and difficulties on highly stretched unstructured meshes. The FEM, on the other hand, is naturally suited to these types of meshes due to the piecewise-continuous representation of the solution variables [44]. Although many stabilization schemes were devised to address the hyperbolic nature of the fluid dynamic equations, one particularly powerful formulation is the edge-based assembly developed by Luo [45]. By restructuring the assembly of the residual vector from element-based to edge-based, significant reductions in computational time and memory requirements can be achieved.

Furthermore, the application of one-dimensional upwind stabilization schemes is natural, as will be discussed in Section 4.3.

Here the term edge is used to describe a pair of nodes belonging to the same element. Following the technique described in [31] the inviscid flux term of equation 4.10 can be integrated by parts to obtain the following

$$\begin{aligned} \int_{V^e} N_j \nabla W_i \cdot (\rho Y_s \mathbf{V})_j dV \\ = \frac{1}{2} \left(\int_{V^e} N_j \nabla W_i dV - \int_{V^e} W_i \nabla N_j dV + \int_A W_i N_j \mathbf{n} dA \right) \cdot (\rho Y_s \mathbf{V})_j \end{aligned} \quad (4.12)$$

The sum of the volume integral terms on the right-hand side of the above equation represents the contribution of the e -th element to the metric coefficient associated with the ij -th edge

$$\boldsymbol{\eta}_{ij}^e = \int_{V^e} N_j \nabla W_i dV - \int_{V^e} W_i \nabla N_j dV \quad (4.13)$$

The assembly of inviscid fluxes over an element becomes

$$\sum_{j \in K_e} \int_{V^e} N_j \nabla W_i \cdot (\rho Y_s \mathbf{V})_j dV = \sum_{j \in K_e} \left[\left(\int_A W_i N_j \mathbf{n} dA - \boldsymbol{\eta}_{ij}^e \right) \cdot \frac{(\rho Y_s \mathbf{V})_j}{2} \right] \quad (4.14)$$

The term on the RHS can be integrated by parts again and developed using the zero-sum property of the gradients of the shape function to obtain

$$\begin{aligned} \sum_{j \in K_e} \int_{V^e} N_j \nabla W_i \cdot (\rho Y_s \mathbf{V})_j dV \\ = - \sum_{j \in K_e} \boldsymbol{\eta}_{ij}^e \cdot \frac{(\rho Y_s \mathbf{V})_j + (\rho Y_s \mathbf{V})_i}{2} + \sum_{j \in K_e} \boldsymbol{\chi}_{ij}^e \frac{(\rho Y_s \mathbf{V})_j - (\rho Y_s \mathbf{V})_i}{2} \end{aligned} \quad (4.15)$$

where a second edge-based elemental metric coefficient is defined as

$$\boldsymbol{\chi}_{ij}^e = \int_A W_i N_j \mathbf{n} dA \quad (4.16)$$

The complete node-pair formulation for the volume term of the inviscid fluxes for a node i is given by taking the summation over every surrounding element e as follows

$$\begin{aligned}
 & \sum_{e \in E_i} \sum_{j \in K_e} \int_{V^e} N_j \nabla W_i \cdot (\rho Y_s \mathbf{V})_j dV \\
 &= - \sum_{j \in K_e} \boldsymbol{\eta}_{ij} \frac{(\rho Y_s \mathbf{V})_j + (\rho Y_s \mathbf{V})_i}{2} + \sum_{j \in K_e} \chi_{ij} \frac{(\rho Y_s \mathbf{V})_j - (\rho Y_s \mathbf{V})_i}{2}
 \end{aligned} \quad (4.17)$$

where the node-pair metric coefficients are given by

$$\boldsymbol{\eta}_{ij} = \sum_{e \in E_i} \int_{V^e} (W_i \nabla N_j - N_j \nabla W_i) dV \quad \chi_{ij} = \sum_{f \in F_i} \int_A W_i N_j \mathbf{n} dA \quad (4.18)$$

The second metric coefficient is non-zero only for elements who possess a face on the boundary Γ . The following properties hold for the first metric coefficient

$$\boldsymbol{\eta}_{ij} = -\boldsymbol{\eta}_{ji}, \quad \boldsymbol{\eta}_{ii} = 0, \quad \sum_{j \in K_e} \boldsymbol{\eta}_{ij}^e + \int_A W_i N_j \mathbf{n} dA = 0 \quad (4.19)$$

If we assume that the mesh is not dynamically changing during the computations, the metric coefficients for all edges may be computed prior to the simulation using the mesh information and Gauss quadrature.

The boundary terms are treated in typical FEM fashion to maintain accurate computation of heat fluxes and shear stresses on surfaces [31]. Flexibility is maintained with respect to the discretization of the viscous fluxes, which may be accomplished through element-based volume integration or changed to an edge-based form [46]. The species mass diffusion fluxes are computed in edge-based fashion, the discretization of which will be omitted here for brevity. The mixed edge-based formulation of the governing equations is therefore as follows

$$\begin{aligned}
 & \sum_{j \in K_i} M_{ij} \frac{d(\rho Y_s)_j}{dt} + \sum_{j \in K_i} \boldsymbol{\eta}_{ij} \frac{(\rho Y_s \mathbf{V})_j + (\rho Y_s \mathbf{V})_i}{2} - \sum_{j \in K_i} \chi_{ij} \frac{(\rho Y_s \mathbf{V})_j - (\rho Y_s \mathbf{V})_i}{2} \\
 &+ \sum_{j \in K_i} \text{tr}(\mathbf{D}_{ij}^S) (\mathbf{J}_s)_{ij} + \sum_{e \in F_i} \int_A W_i \mathbf{n} \cdot (\rho Y_s \mathbf{V} - \mathbf{J}_s) dA = 0
 \end{aligned} \quad (4.20)$$

where M_{ij} is the consistent mass matrix and $\text{tr}(\mathbf{D}_{ij}^S)$ is the trace of the symmetric component of the edge-based second derivative tensor, which may also be pre-computed. The consistent mass matrix M_{ij} is given by

$$M_{ij} = \sum_{e \in E_i} \int_V W_i N_j dV \quad (4.21)$$

Convergence can be improved by using a lumped version of the mass matrix [31], where all entries are lumped onto the diagonal, as follows

$$L_i = \sum_{j \in K_i} M_{ij} \quad (4.22)$$

The conservation of mass, momentum and total energy are solved using a similar hybrid formulation in which only the inviscid fluxes are assembled in an edge-based manner.

4.3 Flux Stabilization Techniques

The PDE's governing inviscid compressible fluid flows have a set of strictly real eigenvalues. Due to their hyperbolic nature, a naïve discretization of inviscid terms of the equation would lead to an unstable scheme for convection dominated flows. In order to guarantee stability, upwinded differencing and artificial diffusion schemes are typically used. In the present section two schemes are briefly discussed; the Roe and AUSM⁺-up schemes.

4.3.1 The Riemann Problem

The Euler equations and the Navier-Stokes equations both admit flow features such as shocks and rarefaction waves that are characteristics of the solution. A Riemann problem is an IVP of a conservation equation with discontinuous initial conditions. This problem displays the same characteristics as typical fluid flow equations and is therefore used to understand their behavior as well as to develop suitable numerical flux discretizations. The one-dimensional time-dependent Euler equations are given by

$$\frac{\partial Q}{\partial t} + \frac{\partial F(Q)}{\partial x} = 0, \quad \text{where } Q = \begin{Bmatrix} \rho \\ \rho u \\ E \end{Bmatrix}, \quad F(Q) = \begin{Bmatrix} \rho u \\ \rho u^2 + p \\ u(E + p) \end{Bmatrix} \quad (4.23)$$

The Riemann problem consists of a piecewise-defined initial state [48], given by

$$W(x, 0) = W_0(x) = \begin{cases} W_L & \text{for } x \leq 0 \\ W_R & \text{for } x > 0 \end{cases} \quad (4.24)$$

where

$$W_L = \begin{Bmatrix} \rho_L \\ u_L \\ p_L \end{Bmatrix} \quad \text{and} \quad W_R = \begin{Bmatrix} \rho_R \\ u_R \\ p_R \end{Bmatrix} \quad (4.25)$$

It can be shown that for a hyperbolic system a centered finite-difference scheme is unstable [48]. We can rewrite the system in quasi-linear form as follows

$$\frac{\partial Q}{\partial t} + A \frac{\partial Q}{\partial x} = 0 \quad (4.26)$$

where A is the flux Jacobian in one dimension, given as follows

$$A = \frac{\partial F}{\partial Q} = \begin{bmatrix} 0 & 1 & 0 \\ \frac{1}{2}(\gamma - 3)u^2 & (3 - \gamma)u & \gamma - 1 \\ u \left[\frac{1}{2}(\gamma - 1)u^2 - H \right] & H - (\gamma - 1)u^2 & \gamma u \end{bmatrix} \quad (4.27)$$

The characteristic speeds of the system correspond to the eigenvalues of the flux Jacobian. For the current set of equations, the eigenvalues and characteristic vectors are given by

$$\begin{aligned} \lambda_1 &= u - a, & \lambda_2 &= u, & \lambda_3 &= u + a \\ r_1 &= \begin{Bmatrix} 1 \\ u - a \\ H - ua \end{Bmatrix}, & r_2 &= \begin{Bmatrix} 1 \\ u \\ \frac{1}{2}u^2 \end{Bmatrix}, & r_3 &= \begin{Bmatrix} 1 \\ u + a \\ H + ua \end{Bmatrix} \end{aligned} \quad (4.28)$$

These eigenvectors are linearly independent. As such the flux Jacobian satisfies the homogeneity property $F = AQ$, therefore allowing a variety of flux vector splitting (FVS) and flux difference splitting (FDS) schemes to be developed.

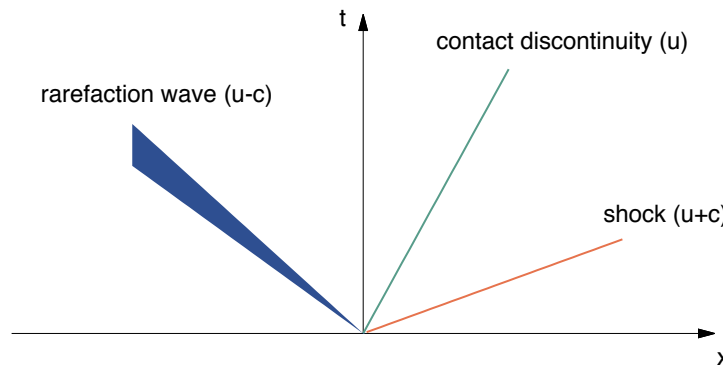


Figure 4.1 - Diagram of 1D Riemann problem

4.3.2 Roe's Scheme

It is possible to solve the Riemann problem exactly by calculating the characteristic wave speeds of the system to determine the actual left and right states. However, this discretization, known as Godunov's scheme, is still only $\mathcal{O}(\Delta x)$ due to the assumption of piecewise constant data. Roe suggested solving an approximate Riemann problem whereby the flux Jacobian is replaced by an average Jacobian \tilde{A} , which satisfies the following properties

- 1) *Hyperbolicity*: the matrix \tilde{A} is required to have n real eigenvalues and linearly independent right eigenvectors.
- 2) *Consistency*: $\tilde{A}(Q_L, Q_R) \rightarrow A$ as $\Delta Q \rightarrow 0$
- 3) *Conservation*: $\tilde{A} \cdot (\Delta Q) = F(Q_R) - F(Q_L)$

To obtain the above conditions, Roe defined a set of averaged variables, given below

$$\begin{aligned} \tilde{\rho} &= \sqrt{\rho_L \rho_R}, & \tilde{u} &= \frac{\sqrt{\rho_L} u_L + \sqrt{\rho_R} u_R}{\sqrt{\rho_L} + \sqrt{\rho_R}} \\ \tilde{H} &= \frac{\sqrt{\rho_L} H_L + \sqrt{\rho_R} H_R}{\sqrt{\rho_L} + \sqrt{\rho_R}}, & \tilde{a}^2 &= (\gamma - 1) \left[\tilde{H} - \frac{1}{2} \tilde{u}^2 \right] \end{aligned} \quad (4.29)$$

With these conditions met, the interface flux can be defined as

$$F_{ROE}(Q_R, Q_L) = \frac{F(Q_R) + F(Q_L)}{2} - \frac{1}{2} \sum_{i=1}^3 \tilde{\lambda}_i \tilde{\alpha}_i \tilde{r}_p \quad (4.30)$$

where $\tilde{\lambda}_i$ are the eigenvalues of the approximate Jacobian, \tilde{r}_p are the corresponding right eigenvectors and $\tilde{\alpha}_i$ are the wave strengths. The eigenvalues and eigenvectors are the same as in equation 4.28 computed using the Roe averaged variables. Finally, the wave strengths are given by

$$\begin{aligned} \tilde{\alpha}_2 &= \frac{(\gamma - 1)}{\tilde{\alpha}} \left((\tilde{H} - \tilde{u}^2) \Delta \rho + \tilde{u} \Delta(\rho u) - \Delta E \right) \\ \tilde{\alpha}_1 &= \frac{1}{2\tilde{a}} \left((\tilde{u} + \tilde{a}) \Delta \rho - \Delta(\rho u) - \tilde{a} \tilde{\alpha}_2 \right) \\ \tilde{\alpha}_3 &= \Delta \rho - (\tilde{\alpha}_1 + \tilde{\alpha}_2) \end{aligned} \quad (4.31)$$

By construction, Roe's approximate solver admits discontinuities into its solution. However, this scheme cannot differentiate between a compression process and an expansion process and

therefore sometimes places an unphysical shockwave in an expansion fan. Thus, this work uses the entropy correction proposed by Harten [48] to suitably correct the wave speeds and avoid Carbuncle phenomena. Although the entropy fix creates a very robust solver it tends to result in more diffusion than certain FVS schemes [49]. The scheme may be extended to 3D flows by considering the full flux Jacobian.

4.3.3 AUSM⁺-up Scheme

The AUSM scheme first proposed by Liou and Steffen [49] is a FVS technique that aims to separate the flux vector into components that can each be appropriately upwinded. The flux vector is divided into a convective component and a pressure component as follows

$$F = F_c + F_p = \begin{Bmatrix} \rho u \\ \rho u^2 \\ \rho u H \end{Bmatrix} + \begin{Bmatrix} 0 \\ p \\ 0 \end{Bmatrix} \quad (4.32)$$

Liou and Steffen recognized that the convective flux is transported by the entropy wave $\lambda = u$, while the pressure perturbation is transported by the acoustic waves $\lambda = u \pm a$. To determine stable upwinding for the convective fluxes an interface Mach number is defined as

$$M_{1/2} = M_L^+ + M_R^- \quad (4.33)$$

where the Mach number is split as per Van Leer's Mach number splitting for subsonic flows [50]. The convective flux is therefore given by

$$F_c = M_{1/2} \begin{Bmatrix} \rho a \\ \rho u a \\ \rho a H \end{Bmatrix}_{(L \text{ or } R)} \quad \text{where } (L \text{ or } R) = \begin{cases} L & \text{if } M_{1/2} \geq 0 \\ R & \text{if } M_{1/2} < 0 \end{cases} \quad (4.34)$$

The pressure term is split similarly to the Mach number

$$p_{1/2} = p_L^+ + p_R^- \quad (4.35)$$

The first order polynomial splitting proposed by Liou and Steffen are used. The full interface flux is therefore as follows

$$F_{AUSM}(Q_L, Q_R) = M_{1/2} \begin{Bmatrix} \rho a \\ \rho u a \\ \rho a H \end{Bmatrix}_{(L \text{ or } R)} + \begin{Bmatrix} 0 \\ p_{1/2} \\ 0 \end{Bmatrix} \quad (4.36)$$

The AUSM scheme satisfies the entropy condition and exhibits positivity preserving characteristics. The present work utilizes the improved AUSM⁺-up scheme proposed by Liou, which exhibits better robustness across a wider range of flow speeds [51]. It is much less diffusive than Roe and is slightly more efficient due to not requiring differentiation of the fluxes.

4.3.4 Flux Stabilization for the Decoupled Chemical System

The schemes that were introduced in Sections 4.3.2 and 4.3.3 are applicable to governing equations of fluid flow with hyperbolic characteristics. These schemes were originally developed for perfect ideal gases in chemical and thermodynamic equilibrium. When considering additional governing equations such as the conservation of species mass and vibrational-electronic energy, a straightforward extension of the upwinding scheme is not possible. To account for the additional flow physics, these schemes should be re-derived using the fully-coupled system of equations. In the case of Roe's scheme this would involve significant computational overhead to evaluate the eigenvalues and eigenvectors. Furthermore, as will be discussed in section 4.6, the present work opts to solve each system separately. As such, the direct application of the previous solvers to the decoupled chemical system has been shown to be unsuitable [52]. This is because the eigenvalues of the decoupled chemical flux Jacobian consist only of degenerate eigenvalues corresponding to the entropy wave, causing the flux scheme to neglect potential shock or rarefaction waves present in the solution. Since these waves are properly considered in the gasdynamic system, this may lead to a consistency error between the two systems.

The fluxes in the chemical system are therefore modeled using the approximate multi-component flux method found in [52]. This scheme computes the species mass flux by first computing the total mass flux of the gasdynamic system and subsequently multiplying it by the upwinded species mass fraction, as shown below

$$\mathbf{F}_s^i = \widehat{\mathbf{F}}_\rho \begin{cases} Y_{s,L} & \text{if } \widehat{\mathbf{F}}_\rho \geq 0 \\ Y_{s,R} & \text{else} \end{cases} \quad (4.37)$$

Equation 4.37 ensures that the species fluxes capture all the flow physics considered by the flux scheme being used in the gasdynamic system. In addition, the following consistency property is satisfied

$$\sum_{s=1}^{N_s} Y_s = 1 \Rightarrow \sum_{s=1}^{N_s} \mathbf{F}_s^i = \widehat{\mathbf{F}}_\rho \quad (4.38)$$

Finally, in the absence of chemical source terms, it has been shown that the current scheme satisfies the discrete maximum principle [52] for all spatial positions i in the domain and time levels n

$$\min_j Y_j^0 \leq Y_i^n \leq \max_j Y_j^0 \quad (4.39)$$

Which is a favorable property for both stability and convergence.

4.4 MUSCL Reconstruction

The edge-based formulation permits the application of FV-style flux schemes on each geometric edge. When attempting to discretize a hyperbolic partial differential equation, first-order schemes that have suitable unwinding are known to be stable under certain conditions but diffusive. A strict notion of stability is that of monotonicity; in other words, not generating new extrema [48]. However, Godunov's theorem states that "*Linear numerical schemes for solving partial differential equations, having the property of not generating new extrema can be at most first-order accurate*" [31]. A less strict notion of stability for CFD was defined by Harten as the Total Variation Diminishing (TVD) property [49]. A numerical scheme is said to be TVD if

$$TV(Q^{n+1}) \leq TV(Q^n) \quad (4.40)$$

where the total variation is defined as

$$TV = \sum_i |Q_{i+1} - Q_i| \quad (4.41)$$

It has been shown that some higher order linear schemes are not TVD and may produce spurious oscillations in the presence of discontinuities [50]. It is possible to overcome the Godunov barrier by resorting to a non-linear scheme such that second order accuracy can be achieved when the solution is sufficiently smooth, while retaining the TVD property for regions of sharp discontinuities. To this end, the Monotonic Upstream-Centered Scheme for Conservation Laws (MUSCL) was introduced by Bram van Leer [50] in 1979. Consider a discrete representation of a

vector of quantities Q that is represented by a piecewise-linear function that is discontinuous at the edge midpoint, as seen in Figure 4.2.

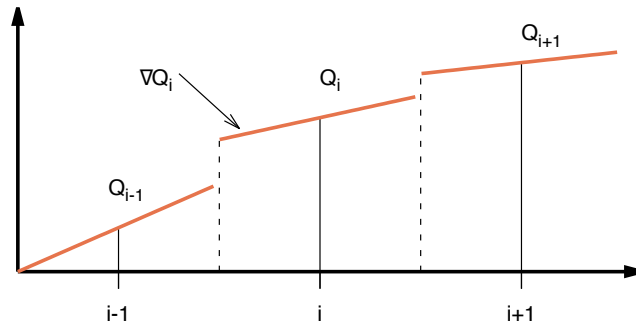


Figure 4.2 - Diagram of MUSCL piecewise linear one-dimensional reconstruction

The function for a given node is therefore expressed as

$$Q_i(\mathbf{x}) = Q_i + \nabla Q_i \cdot (\mathbf{x} - x_i) \quad (4.42)$$

The reconstructed values of Q at the interface relative to node i or j are given by

$$Q_{i,i,j} = Q_i + \nabla Q_i \cdot \frac{x_j - x_i}{2} \quad Q_{j,i,j} = Q_j + \nabla Q_j \cdot \frac{x_i - x_j}{2} \quad (4.43)$$

Note that higher order reconstructions are possible but are not used in the present work. If the reconstruction is neglected, a first-order solution is obtained. Note that the flux reconstruction technique does not guarantee a higher-order solution in all parts of the flow, especially where steep gradients are seen.

Flux Limiters

Although the MUSCL technique permits second order solutions, to ensure stability as per the TVD property [53], one may apply a one-dimensional limiter to the edge-based reconstruction as follows

$$Q_{i,i,j} = Q_i + \frac{1}{2} \lim(\Delta Q_{ij}, \Delta Q_{ij,up}), \quad Q_{j,i,j} = Q_j - \frac{1}{2} \lim(\Delta Q_{ij}, \Delta Q_{ij.down}) \quad (4.44)$$

Defining the limiting function as $\lim(a, b)$, a wealth of options is available for symmetric, TVD limiters [54]. Symmetry in the limiter ensures that forward and backward gradients are treated in the same fashion. For completeness, a Sweby diagram is shown in Figure 4.3 comparing various implemented limiters, with the 2nd order TVD region shown in gray. The x -axis represents the

ratio of successive gradients $r = \frac{(Q_i - Q_{i-1})}{(Q_{i+1} - Q_i)}$ and the y -axis represents the limiter function ϕ . A smooth solution occurs when $r = 1$, and therefore the limiter function should apply the higher resolution flux, $\phi = 1$.

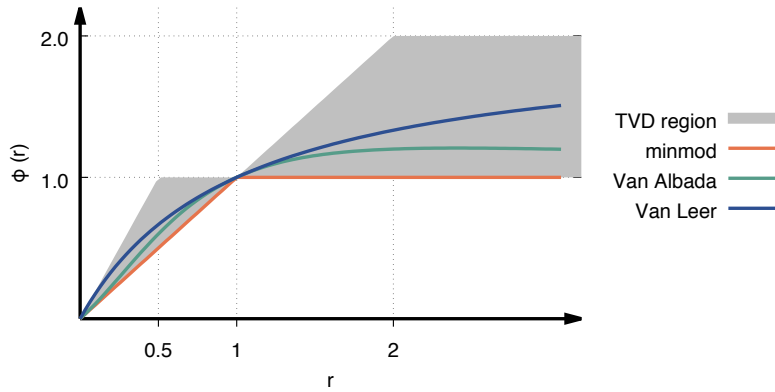


Figure 4.3 - Sweby diagram of various flux limiters

In general, a limiter which tends more towards the upper boundary of the TVD region is less diffusive. In the present work, only the Van Albada TVD limiter is used due to its satisfactory accuracy and stability properties. The Van Albada limiter is given below

$$\lim(a, b) = \frac{a^2 b + b^2 a}{a^2 + b^2} \quad (4.45)$$

4.5 Time Discretization

The full system of equations is rewritten in matrix form as

$$\mathbf{L} \frac{d\mathbf{Q}}{dt} + \mathbf{R}(\mathbf{Q}) = 0, \quad \text{where} \quad \mathbf{R}(\mathbf{Q}) = \mathbf{K}\mathbf{Q} - \mathbf{F} \quad (4.46)$$

where \mathbf{Q} is the nodal vector of unknowns, \mathbf{L} is the mass matrix and \mathbf{R} is the residual vector. At this point we must make the choice between discretizing the time term in an explicit or implicit manner. Implicit numerical methods are typically chosen for problems that exhibit a large degree of stiffness, meaning that they require an impractically small time step to remain numerically stable. This is a significant problem in hypersonic flows in chemical non-equilibrium, since the chemical source term is extremely non-linear. The chemical source term has strong exponential dependence on temperature as well as quadratic or cubic dependence on species densities, depending on the order of reaction [55]. Thus, vastly different chemical time scales are present in

the solution and an implicit discretization of the chemical system is a more suitable choice. We define the change in the nodal solution vector as

$$\Delta \mathbf{Q} = \mathbf{Q}^{n+1} - \mathbf{Q}^n \quad (4.47)$$

An implicit discretization is achieved by computing the residual vector using the future state \mathbf{Q}^{n+1} . The system is rearranged into the following system of equations

$$\mathbf{A}(\mathbf{Q}^n)\Delta \mathbf{Q} = -\mathbf{R}(\mathbf{Q}^n) \quad (4.48)$$

where

$$\mathbf{A} = \frac{\mathbf{L}}{\Delta t} \mathbf{I} + \left. \frac{\partial \mathbf{R}}{\partial \mathbf{Q}} \right|_n \quad (4.49)$$

The Jacobian matrix \mathbf{A} is a square matrix of dimension equal to the number of equations per node. The Jacobian terms for the chemical system may be found in the Appendices. The time step Δt is computed using a specified Courant number, defined as

$$\text{CFL} = \frac{\lambda_{max} \Delta t}{\Delta x} \quad (4.50)$$

where λ_{max} is the largest wavespeed at the current node and Δx is a measure of the element's edge lengths. The CFL number is typically chosen to be between 1 and 10.

The employed implicit methodology marches the solution forward in pseudo-time until a measure of the residual vector is suitably close to zero. However, for verification and validation purposes an unsteady time integration scheme has also been implemented via a dual time-stepping technique outlined in [56]. This allows unsteady reactor cases to be simulated, as will be demonstrated in Section 5.

4.6 Loosely-coupled Methodology and Solution of the Linear System

The computation of the Jacobian matrix is one of the aspects that renders the implementation of implicit methods complex. Not only must all terms be analytically differentiated with respect to the solution variables, but the resulting linear system is quite large in terms of memory requirements, as its size scales quadratically with the number of equations for a three-dimensional problem. Moreover, the computational requirements in solving the linear system at each iteration is significantly increased. Candler proposed a decoupled implicit method

for steady-state hypersonic flows [16] in which the species mass and vibrational-electronic energy conservation equations are solved as a separate linear system. As such, the solution of a large linear system is traded for two smaller ones, resulting in smaller storage requirements as well as decreased solution times for each iteration. This is even more advantageous when the complexity of the reaction scheme is increased, and more species are considered.

The present work uses a loosely-coupled scheme in which the thermal non-equilibrium system is also solved as a separate system. Presently, the system for the thermodynamic non-equilibrium only consists of a single vibrational-electronic energy equation. However, this approach allows the relatively easy extension to a multi-vibrational temperature or a three-temperature model. In addition, whereas Candler’s method solves each system for the change in variables from time level n to $n + 1$, the present work updates the thermochemical state of the flow field after the solution of each independent system. This is comparable to performing a Gauss-Seidel update of the solution as opposed to a Jacobi one, and therefore an improvement in performance is expected. However, this method does not allow the use of relation 3.10 to remove an equation from the system, since the conservation of total mass is computed for a different time frame. Using this relation would therefore create instabilities at the beginning of the simulation, when difficult flow features are developing. A flow chart of the loosely coupled methodology for a flow in chemical non-equilibrium is shown in Figure 4.4. If thermodynamic non-equilibrium is considered, the vibrational-electronic energy system is solved sequentially in the same manner.

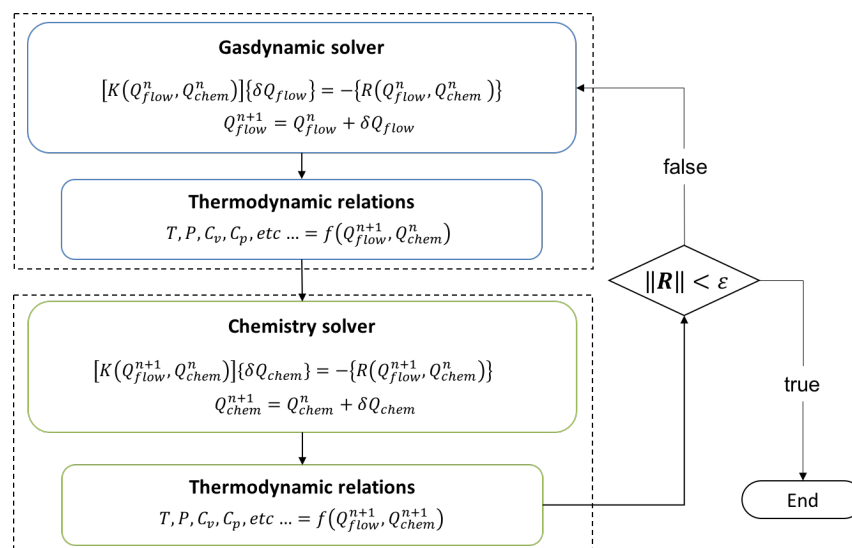


Figure 4.4 - Flow chart of loosely-coupled solution methodology for chemical non-equilibrium flow

The resulting matrix systems are solved using a GMRES iterative method with an incomplete lower-upper (ILU) preconditioner. The PETSc library [57] is used for this purpose, ensuring fast and scalable implementation of the sparse linear solvers. Convergence is monitored using the L_2 norms of the residual vector, shown below

$$\|\mathbf{R}\|_{L_2} = \sqrt{\sum_{k=1}^n |R_k|^2} \quad (4.51)$$

where n is the number of degrees of freedom. The overall residual of a system is evaluated using the RMS value of the set of residuals of the entire system, as follows

$$\|\mathbf{R}\|_{RMS} = \sqrt{\frac{\sum_{i=1}^N \|\mathbf{R}\|_{L_2}^2}{N}} \quad (4.52)$$

where N is the number of equations in the system.

4.7 Boundary Conditions

The imposition of boundary conditions is quintessential in forming a well-posed problem and obtaining an accurate computation of the governing equations. There are two basic classes of boundary conditions; Dirichlet and Neumann. Both types of boundary conditions are easily imposed in the FEM formulation.

A Dirichlet condition imposes the solution at a given node by imposing the condition that $\delta Q_i = 0$. This is done by setting the entire row in the linear system to be zero except for the column corresponding to node, which is set to one. The corresponding row in the residual vector is also set to zero, therefore resulting in a variable change of zero upon solving. Since the present formulation solves for the change in conservative variables, if a primitive variable must be imposed some alteration is required. This is referred to as a *pseudo-Dirichlet* condition and will be discussed later. A Neumann condition imposes the gradient of the solution $\partial Q_i / \partial n$ or a flux at the boundary. In the present section, relevant boundary conditions for the chemical system will be described.

4.7.1 Inlets

For all inlets, the species mass fractions are imposed on the boundary. Furthermore, it is assumed that no mass diffusion fluxes exist through the boundary. The imposition of the chemical inviscid fluxes on inlet boundaries will be discussed in the following sections.

4.7.1.1 Supersonic Inlet

When the inlet flow is supersonic, all characteristics are entering the domain and therefore the conservative variables may be imposed. For the chemical system, these variables are the species densities. Thus, the following condition is imposed in the linear system for all species

$$\delta(\rho Y_s) = 0, \quad \forall s \in [1, N_s] \quad (4.53)$$

4.7.1.2 Riemann Inlet

Riemann boundary conditions make use of the Riemann invariants to properly specify inlet and outlet conditions. These are used when the flow at a boundary is not necessarily completely supersonic or subsonic. Given a reference state Q_∞ , a gauss state Q_g and a resulting Riemann state Q_r , the Riemann state can be calculated as follows

$$Q_r = Q_g - [R(Q_g)N(Q_g)L(Q_g)](Q_\infty - Q_g) \quad (4.54)$$

where R and L are the right and left eigenvectors and N is a diagonal matrix that depends on the eigenvalues vector Λ

$$N_{i,i} = -\max(0, \text{sgn}(\lambda_i)) \quad (4.55)$$

The resulting boundary state is given in the table below:

Table 4.1 - Riemann state for various flow conditions

Condition	State
Subsonic inflow	Q_r
Subsonic outflow	Q_r
Supersonic inflow	Q_∞
Supersonic outflow	Q_g

The boundary term is therefore given by

$$\sum_{e \in F_i A} \int W_i \mathbf{n} \cdot \mathbf{F}_r^i dA = \sum_{e \in F_i A} \int W_i \mathbf{n} \cdot \mathbf{F}^i \left(Q_r \left(\sum_j N_j Q_j \right) \right) dA \quad (4.56)$$

As discussed in Section 4.3.4, decoupling the chemical system can lead to a misrepresentation of the characteristic wave speeds. Therefore, the Riemann state is computed as for the gasdynamic system and subsequently the mass fractions are taken from the inlet state or the grid value if the boundary is an inlet or outlet, respectively.

4.7.2 Outlets

If the flow is supersonic at the outlet, all characteristics are leaving the domain. Thus, the values at the gauss point are used to compute the flux and this flux is subsequently imposed as

$$\sum_{e \in F_i A} \int W_i \mathbf{n} \cdot \mathbf{F}_{out}^i dA = \sum_{e \in F_i A} \int W_i \mathbf{n} \cdot \mathbf{F}^i \left(\sum_j N_j Q_j \right) dA \quad (4.57)$$

If an outlet is not imposed as supersonic, a Riemann condition is used. The species mass fractions on outlet boundaries are taken from the gauss state. Mass diffusion is included on outlet boundaries.

4.7.3 Walls

4.7.3.1 Slip Wall

A slip wall is typically used in cases of inviscid flow. The no penetration condition is enforced in the gasdynamic system. Since the chemical system consists of a set of continuity equations, the conditions are simply

$$\mathbf{n}(\mathbf{x}_g) \cdot (\rho Y_s \mathbf{V}) = 0 \quad \forall s \in [1, N_s] \quad (4.58)$$

The symmetry plane boundary condition is equivalent to a slip-wall.

4.7.3.2 No-slip Wall

When viscous flows are being simulated, the velocity at the wall is usually set to zero. For rarefied gases velocity and temperature jump conditions may exist, but these are neglected in

this work. The wall may be adiabatic (zero heat flux) or isothermal (set wall temperature). Primitive variables such as temperature and velocity are enforced on the wall by imposing zero change in primitive variables and subsequently solving for the resulting change in conservative variables using an algebraic relationship. This boundary condition will be referred to as a *pseudo-Dirichlet* condition.

There has been considerable investigation on chemical boundary conditions and their influence on surface heat fluxes. Varying amounts of catalytic recombination at the wall have been reported which are dependent on the gas-surface interaction [28]. In this work, the non-catalytic and super-catalytic boundary conditions are implemented, representing the lower and upper limits on heat fluxes, respectively [58]. For a non-catalytic wall, the species mass fractions may vary, and mass diffusion is set to zero by enforcing $\partial Y_s / \partial \eta = 0$. On the other hand, super-catalytic walls are often enforced on isothermal walls. This *pseudo-Dirichlet* condition is imposed by setting $\delta Y_s = 0$ and defining an algebraic relationship between the primitive and conservative chemistry variables as

$$\delta \rho_s = Y_s \delta \rho, \quad \text{where } \delta \rho = \sum_{i=1}^{N_s} \delta \rho_i \quad (4.59)$$

Therefore, we have

$$\delta \rho_s (1 - Y_s) - \sum_{i=1, i \neq s}^{N_s} Y_s \delta \rho_i = 0, \quad \forall s \in [1, N_s] \quad (4.60)$$

The above relationship is inserted into the linear system before the solution step.

5 Results

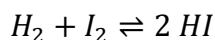
In the present section the physical and numerical modeling is applied to a series of test cases. Specific cases were chosen to provide isolated verification and validation of distinct features during implementation. Firstly, the finite-rate chemical kinetic model is tested on several zero-dimensional reactor cases. An additional reactor is presented that includes thermodynamic non-equilibrium and vibration-dissociation coupling effects. Subsequently, a two-dimensional inviscid problem in thermo-chemical non-equilibrium is presented and cross-code validation is performed. The species mass diffusion fluxes are then verified using a mixing layer problem. Next, a two-dimensional viscous chemical non-equilibrium flow is simulated, and cross-code and experimental validation is conducted. Finally, a three-dimensional viscous thermo-chemical non-equilibrium flow is simulated. For this final test case, cross-code validation and a brief parametric study are performed.

5.1 Validation of Chemical Source Term

Finite-rate chemical reactions are inherently time-dependent phenomena and thus may be appropriately studied using zero-dimensional reactor problems. These may be set up in the solver by using a cube mesh and neglecting advective and diffusive effects. The reaction is enabled in HALO3D with unsteady time integration. The mesh walls are adiabatic, and the thermodynamic state is computed after every iteration. If an isothermal or isobaric condition is required, the temperature or pressure are imposed after each iteration manually.

5.1.1 Hydrogen-iodine Production

To determine if the chemical source term has been implemented properly, a simple reactor test case can be created which allows a bath gas to react under certain conditions. A classic reaction that has a simple analytical solution is the constant-temperature bimolecular reaction that yields hydrogen iodide



The rate coefficients are constant due to the constant temperature condition [13]. The forward reaction rate parameters, obtained from the NIST kinetics database [59] are shown in Table 4.1. The analytical solution is given by

$$\frac{d[C_{HI}]}{dt} = \frac{k_f}{2} (2[C_0] - [C_{HI}])^2 - 2k_b[C_{HI}]^2$$

The initial temperature and pressure are $T = 700$ K and $p = 0.528$ atm, respectively, and the mixture is set to initially be 50 % H_2 and 50 % I_2 by volume. To comply with the constraints of the reaction, the temperature is re-initialized at 700 K after each iteration. The time evolution of the molar concentration of the products and reactants are plotted against the analytical solution in Figure 5.1. Since the reaction is reversible, the reaction does not proceed to completion, and some reactants are still present in the final mixture.

Table 5.1 - Forward reaction rate parameters for hydrogen iodine case

A_f	η_f	E_a/R_u
1.939E14	0.0	20566

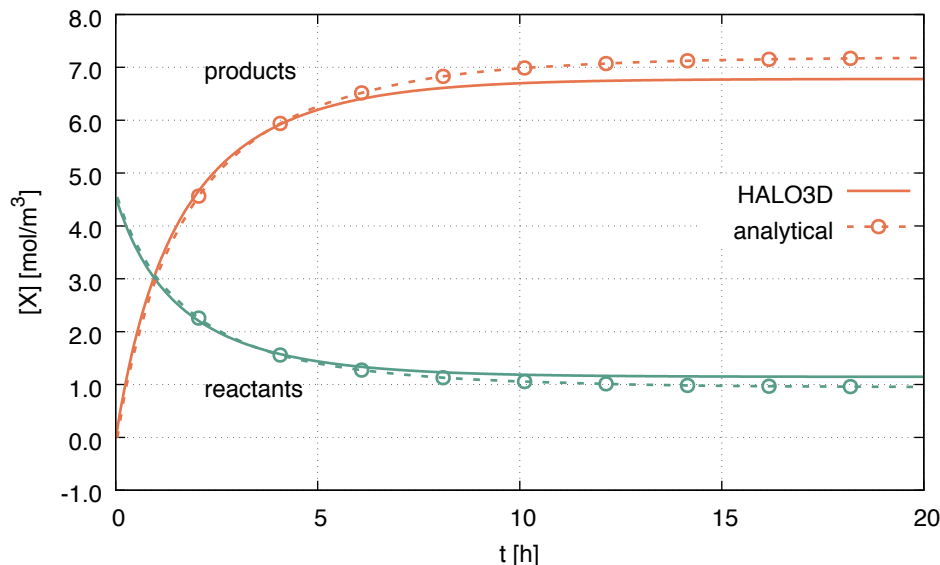


Figure 5.1 - Molar concentration of products and reactants versus time. HALO3D (solid) versus analytical solution (dashed).

The agreement with the analytical solution is seen to be very good. It is noted that HALO3D computes the backward reaction rate coefficient using the Gibbs formulation for the equilibrium constant and this may be the reason for the minor discrepancies seen in the final solution.

5.1.2 High-temperature Air Reaction

Although the simplest high temperature air models include only five chemical species and 17 reactions, the level of complexity increases significantly when ionization, ablation and other effects are considered. As such, the chemical source term must be validated using a more complex reaction mechanism to assess its validity for large, coupled reaction schemes. The present test case considers a 5-species air model with 19 irreversible reactions. These reactions include 3 dissociation reactions (each with 5 possible third bodies) and 4 exchange reactions. The reaction rate parameters are taken from a full report on the DSMCfoam open-source solver [60]. The initial pressure is 0.063 atm and the initial temperature is 10000 K. The gas is assumed to be in thermal non-equilibrium. The reaction is adiabatic and therefore the energy equation of the HALO3D Navier-Stokes solver is included. The results are compared against the open-source chemistry toolkit Cantera [61]. The time evolution of normalized number densities for each species is shown in Figure 5.2, while the time evolution of the temperature is shown in Figure 5.3.

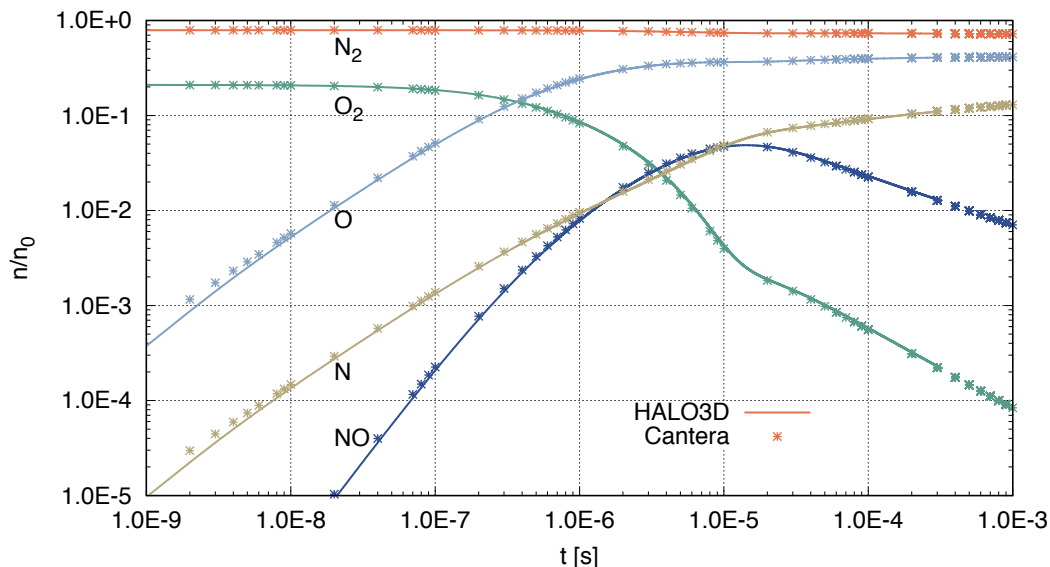


Figure 5.2 - Normalized number densities versus time for 5-species air. Comparison between HALO3D (solid) and Cantera (points).

The agreement is shown to be excellent, indicating the correct implementation of both the chemical source term and the thermodynamic relations. The time-evolution of the chemical species demonstrates several important concepts for air chemistry. Firstly, it is seen that oxygen begins dissociating much earlier than nitrogen. However, they both exhibit the same rate of

dissociation, since both reactions are of the same order. There is initially no nitric oxide in the gas, meaning the production of this species relies initially on exchange reactions, which are of order zero. Another important effect is seen in the temperature in Figure 5.3, called relaxation. Dissociation being an endothermic process, the enthalpy of the product species is larger than the reactant species, resulting in a decrease in gas temperature. In turn, this lower temperature contributes to lower reaction rates as the reaction proceeds, which can be seen in Figure 5.2. It is important to capture such a process accurately since chemical relaxation occurs behind shock waves in hypersonic flows.

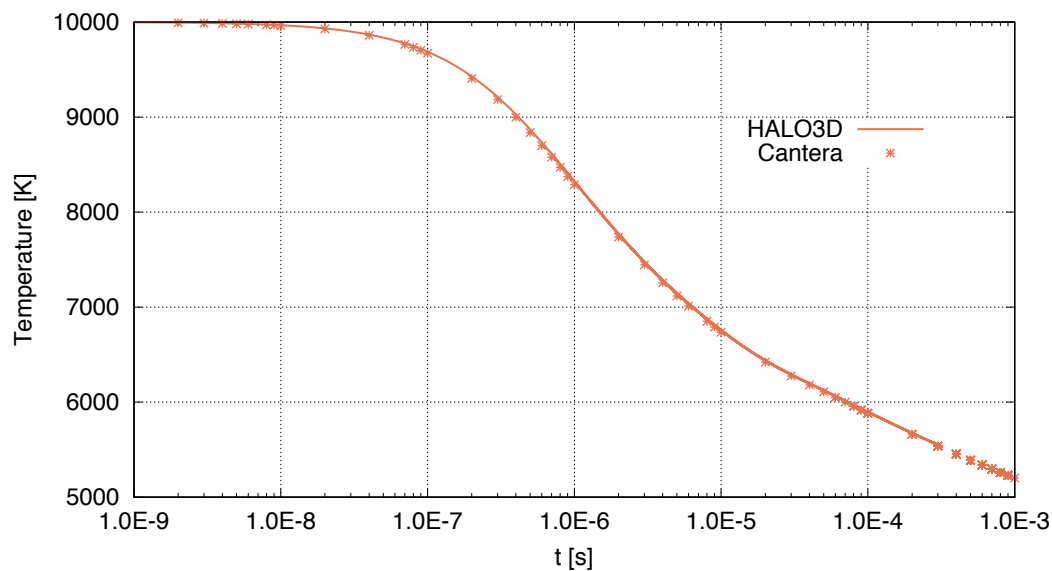
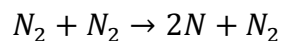


Figure 5.3 - Temperature of 5-species reacting air versus time. Comparison between HALO3D (solid) and Cantera (points).

5.2 Validation of Vibration-dissociation Coupling

When appreciable thermal non-equilibrium is present in a hypersonic flow field it can have a significant effect on the chemical processes. Conversely, a variation in gas composition may change the amount of vibrational-electronic internal energy in the mixture. A test case must therefore be devised to validate and investigate the coupling between the two systems.

Such a case was investigated by Casseau [62] using the hy2foam open-source solver. The case is a reactor which considers the following irreversible nitrogen dissociation reaction



This case tests the relaxation of diatomic nitrogen in a high temperature heat bath. Only one diatomic species is present and therefore neglecting vibrational-vibrational coupling between different molecules is valid. Since the reaction is irreversible, only the forward reaction rate parameters are needed. Casseau considers two reaction mechanisms, shown in Table 5.2.

Table 5.2 - Forward reaction rate parameters for nitrogen relaxation case

	A_f	η_f	E_a/R_u	VD Coupling
Park 1993	7.00E21	-1.6	113200	Park
QK	2.47E18	-0.62	113200	CVDV

The first case considers an initial translational-rotational temperature of 30000 K and vibrational-electronic temperature of 1000 K. The initial gas is composed of equal parts diatomic and atomic nitrogen, each with a number density of $5.0E22 \text{ m}^{-3}$, resulting in a total pressure of 41420 Pa. The reactor setup the same as previous reactors; No advection or diffusion effects are activated, and the walls are adiabatic. The unsteady flow is simulated using the dual time-stepping procedure. It was found that the time-accuracy of the solution was sensitive to the initial time step used, and therefore a refinement in the temporal dimension was used until time convergence was achieved. The time-evolution of the normalized number densities of each species is shown in Figure 5.4. The HALO3D results are compared with those obtained by the hy2foam solver for both the Park and CVDV-QK models, and the agreement between codes is good. The CVDV model predicts faster dissociation, due to the coupling factor V being closer to unity for a wider range of thermal non-equilibrium values. The relaxation of both temperatures is shown in Figure 5.5 and once again the codes are found to be very close. This case demonstrates the significance of vibration dissociation coupling, as the reaction rate at the start of the simulation is relatively slow despite the extremely high initial translational-rotational temperature. This is due to the influence of the low vibrational-electronic temperature, which reduces the effective reaction rate through coupling. As the simulation proceeds, the two temperatures equilibrate and continue to decrease together as the nitrogen continues to dissociate.

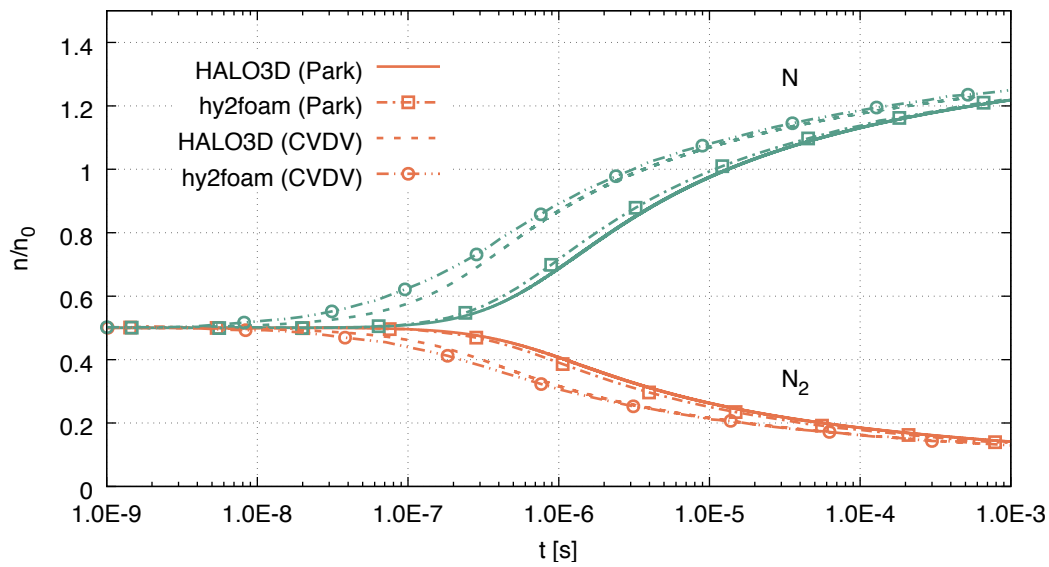


Figure 5.4 - Normalized number densities for relaxation of nitrogen in a heat bath. Comparison between HALO3D (lines) and hy2foam (points) using Park and CVDV-QK models.

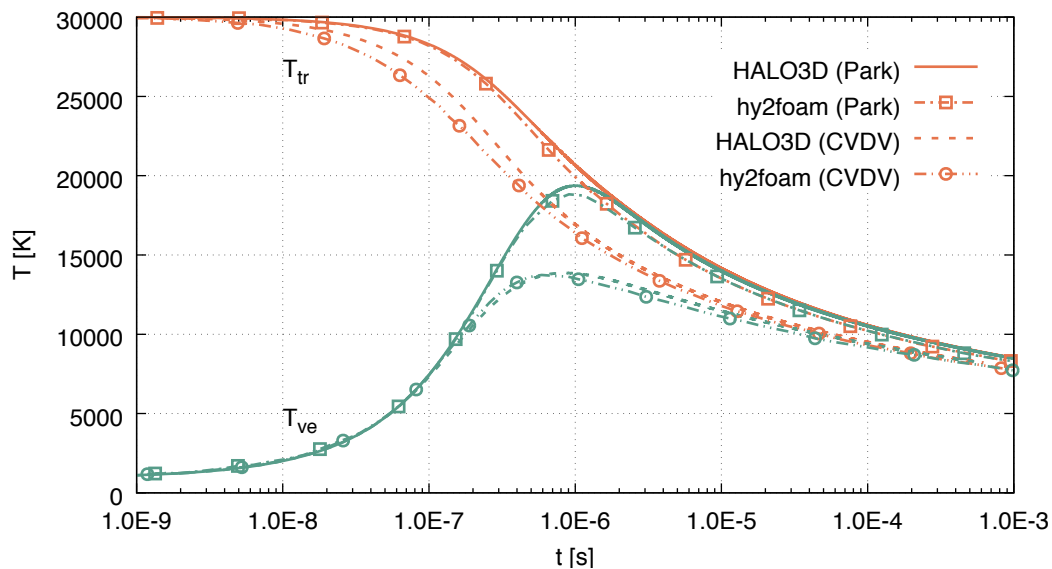


Figure 5.5 - Translation-rotational and vibrational-electronic temperatures for relaxation of nitrogen in a heat bath. Comparison of HALO3D (lines) with hy2foam (points) using the Park and CVDV-QK models.

5.3 Inviscid Thermo-chemical Non-equilibrium Flow Past a Cylinder

After verifying the implementation of the thermal and chemical non-equilibrium source terms, it is important to test the code on a canonical inviscid hypersonic test problem. The cylinder geometry is an extremely common test case for hypersonic codes as it is a blunt body that represents well various components of a hypersonic vehicle, such as the wing leading edge.

The region of the shock layer near the stagnation zone is where most non-equilibrium phenomena takes place.

The test case is of hypersonic inviscid thermo-chemical non-equilibrium flow past a cylinder. Many authors have investigated the flow characteristics of this case [63, 64] and in the present work the results are compared only with those obtained by the NASCART-GT solver [65], though the previously mentioned authors report similar results. The flow conditions are shown in Table 5.3. These conditions are sufficient to induce a significant amount of non-equilibrium in the post-shock region, due to the relatively high Mach number of 12.7. Furthermore, the low Knudsen number is well within the continuum regime. The chemical model used is Park's 1993 reaction scheme, found in Appendix B, which considers a five-species air mixture (N_2 , O_2 , NO , N and O) undergoing dissociation and bimolecular exchange reactions. Park's VD coupling model is used with a rate exponent of $q = 0.7$, and the Boltzmann thermodynamic model is used.

Table 5.3 - Flow parameters for hypersonic thermo-chemical inviscid flow past a cylinder

T_∞ [K]	196	$X_{N_2, \infty}$	79.1
P_∞ [Pa]	90	$X_{O_2, \infty}$	20.9
u_∞ [m/s]	3567	R_{cyl} [m]	0.05
M_∞	12.7	Kn	1.7E-03

The computational grid and problem setup are shown in Figure 5.6. The grid consists of 131072 hexahedral elements, resulting in 131841 periodic nodes. The inlet and outlet boundary conditions are supersonic, and the no-penetration condition is imposed at the cylinder wall. Roe's scheme was used for numerical stabilization with a Van Albada limiter for the MUSCL reconstruction. The simulation was carried out on 48 processors. To avoid convective instabilities at the start of the simulation, a preliminary run is first conducted without the MUSCL reconstruction. This is followed by a second-order run that uses the first-order solution as its initial condition. The convergence curves for each system are shown in Figure 5.7. In general, good convergence characteristics are seen. The chemical system is shown to converge but stall somewhat earlier than the other systems. It is believed that this is a result of the decoupled methodology, though this warrants further investigation.

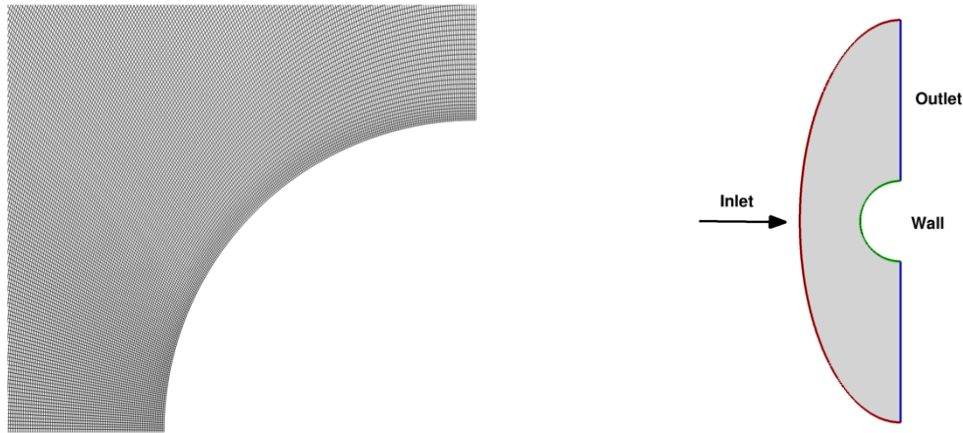


Figure 5.6 - Computational mesh (left) and problem setup (right) for hypersonic inviscid thermo-chemical non-equilibrium flow past a cylinder

The temperature and pressure along the stagnation line are plotted in Figure 5.8 left and right, respectively, and excellent agreement is seen between the two codes. The shock standoff distance is roughly $\delta/R_{cyl} = 0.3$ and the peak temperature predicted by HALO3D is 6164 K, slightly higher than the 6000 K predicted by NASCART-GT and CERANS solvers. The post-shock translational temperature exhibits relaxation due to the chemical dissociation occurring behind the shock. The vibrational-electronic is seen to lag the trans-rotational temperature due to the relatively slow vibrational relaxation time.

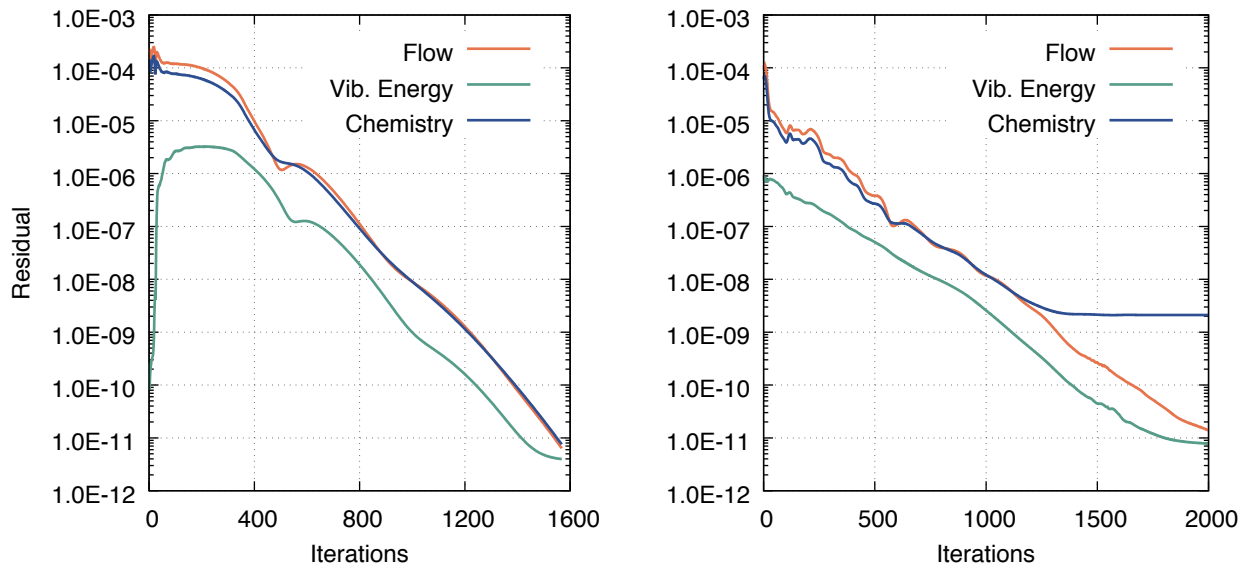


Figure 5.7 - L2 residuals for first order (left) and MUSCL (right) solutions of hypersonic inviscid thermo-chemical non-equilibrium air flow past cylinder

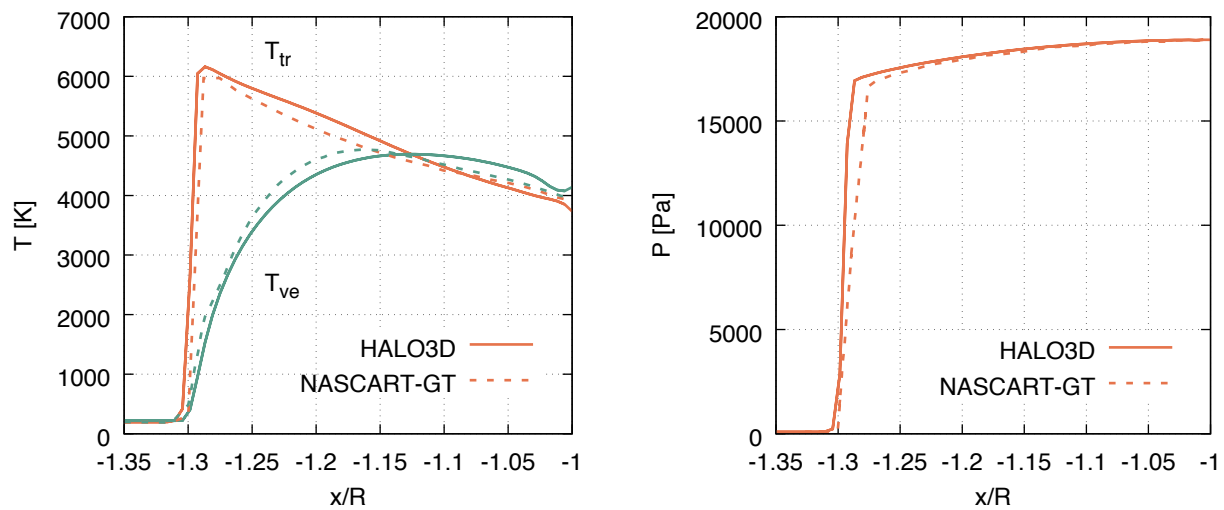


Figure 5.8 - Temperatures (left) and pressure (right) along stagnation line for hypersonic inviscid thermochemical non-equilibrium flow past cylinder. Comparison between HALO3D (solid) and NASCART-GT (dashed).

The molar fractions and density along the stagnation are plotted in Figure 5.9. Due to the relatively low temperature in the shock layer, only minor dissociation occurs. Most of the resulting atomic nitrogen is exchanged to produce nitric oxide, representing roughly 7% of the gas by volume at the stagnation point. Nearly half of the freestream oxygen is dissociated. The density is shown to experience a sharp increase through the shock, followed by a further rise due to the decrease in fluid velocity.

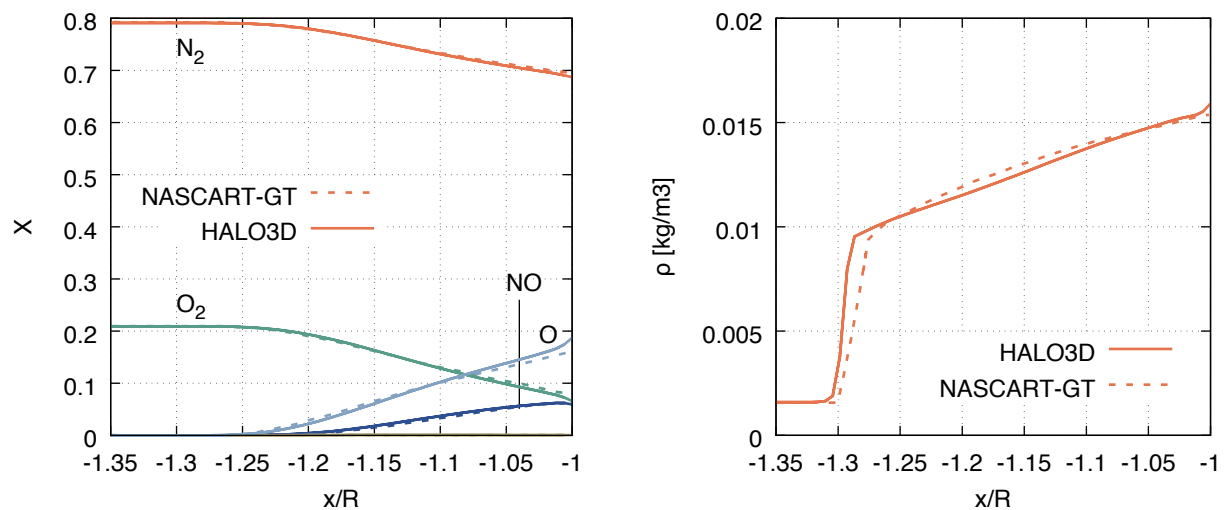


Figure 5.9 - Molar fractions (left) and density (right) along stagnation line for hypersonic inviscid thermochemical non-equilibrium flow past cylinder. Comparison between HALO3D (solid) and NASCART-GT (dashed).

The contours for the translational-rotational and vibrational-electronic temperatures are shown in Figure 5.10, where it is seen that the shock is captured sharply. The relaxation process is quite apparent in the trans-rotational temperature contours. Furthermore, it is observed that the long vibrational relaxation time contributes to the lower overall vibrational temperature in the flow. Immediately after the shock, the vibrational temperature begins to rise to meet the translational temperature. However, the chemical relaxation and increase in velocity away from the stagnation region cause the translational temperature to decrease. The vibrational temperature in this region is therefore higher than the translation temperature since it is slow to equilibrate, and the convective velocity is high. The local Damköhler number and mixture gas constant contours are plotted in Figure 5.11. These are qualitative measures of the degree of chemical non-equilibrium in the flow. The Damköhler number shows that most of the chemical activity occurs in the stagnation region, while the mixture gas constant is a thermodynamic measure of the departure from the freestream gas composition.

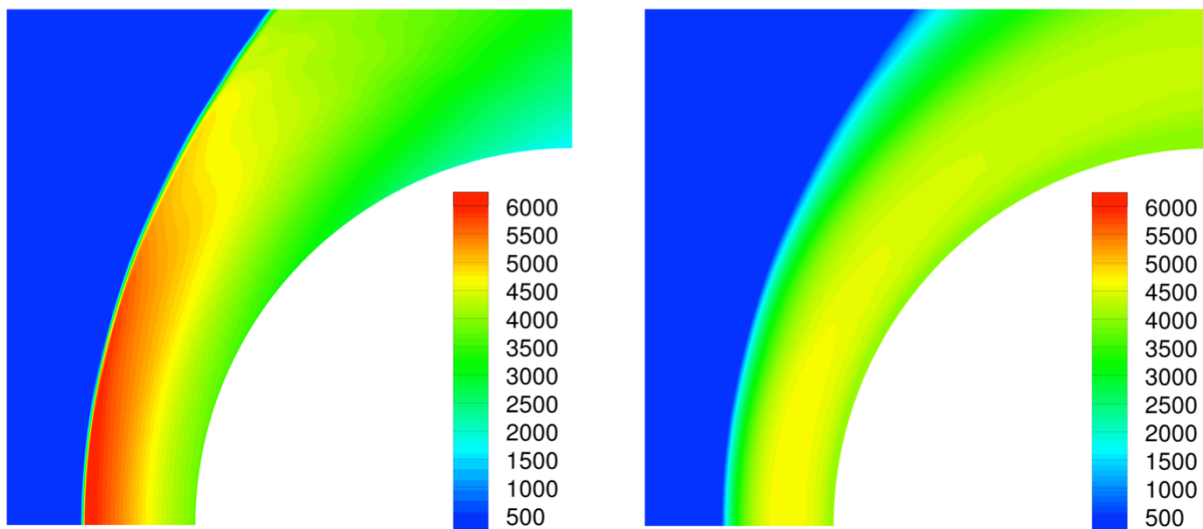


Figure 5.10 - Trans-rotational temperature (left) and vibrational-electronic temperature (right) contours for hypersonic inviscid thermo-chemical non-equilibrium flow past a cylinder

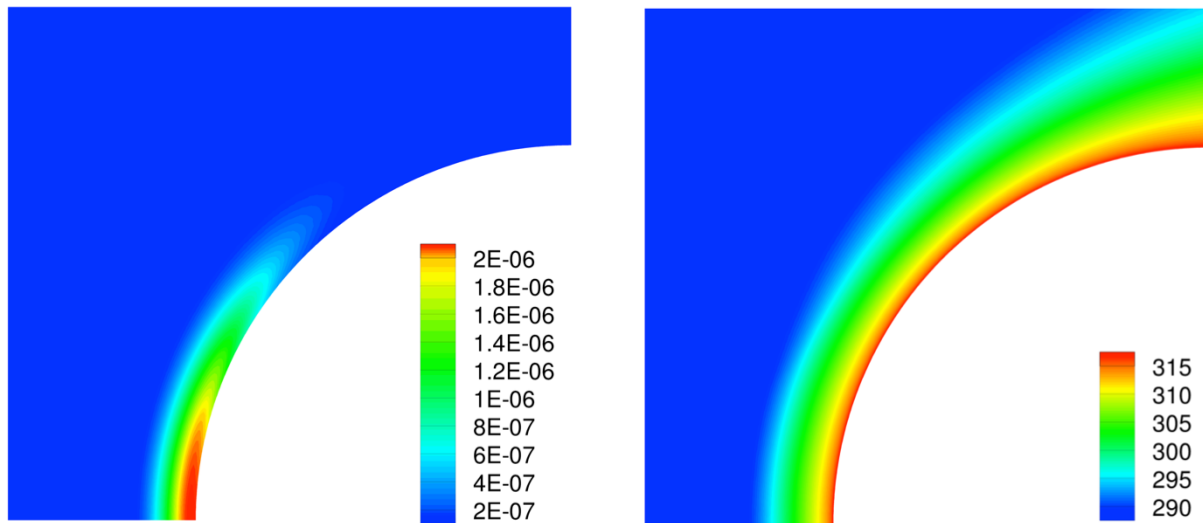


Figure 5.11 - Damköhler number (left) and mixture gas constant (right) for hypersonic inviscid thermochemical non-equilibrium flow past cylinder

5.4 Validation of Species Mass Diffusion

When simulating viscous flows, it is important to accurately model the physical diffusion processes that occur in the flow field. For flows in chemical non-equilibrium, species diffusion due to gradients in concentration is present. This phenomenon is pronounced in boundary layers, where the local convective velocity is low due to the no-slip condition at the wall, thus allowing chemical diffusion to dominate the local flow. The diffusion model therefore has a strong influence on wall quantities such as heat flux and shear stress.

To validate the species diffusion term, a test case was identified that isolates the physical diffusion in the system. This is the case of a laminar mixing layer, which consists of flow through a long channel. The inlet consists of two parallel streams of pure, unmixed gases. Because of the large gradient in species concentration near the inlet, species diffusion occurs, and a mixing layer is created. This problem is analyzed often for combustors as it is analogous to the injection of fuel into an air stream. If the inlet velocities of each stream are different, then a shear layer exists, and values such as momentum and vorticity may be transported across the mid-plane. To simplify the analysis, it is assumed that the inlet velocity of each stream is equal. The mixing layer thickness therefore has an approximate solution given by [66], shown below

$$\delta_m \approx 8 \sqrt{\frac{Dx}{u_{in}}}$$

and the mass fraction profile may be obtained as

$$Y = \frac{1}{2} \left[1 + \operatorname{erf} \left(\frac{4y}{\delta_m} \right) \right]$$

where erf is the *error function*. This expression is valid for a constant diffusion coefficient. The channel is 0.1 meters long and 0.001 meters wide. The present computation is carried out using a freestream temperature of $T_\infty = 273.15$ K, a freestream pressure of $P_\infty = 101325$ Pa, and a freestream velocity of $u_\infty = 1000$ m/s. The upper inlet stream is composed of 100% N_2 while the lower inlet stream is composed of 100% O_2 . A second-order solution is obtained using the AUSM⁺-up scheme to further reduce numerical dissipation. The N_2 mass fraction contours are shown in Figure 5.12, with values above 95% and below 5% cut off to clearly visualize the mixing layer.

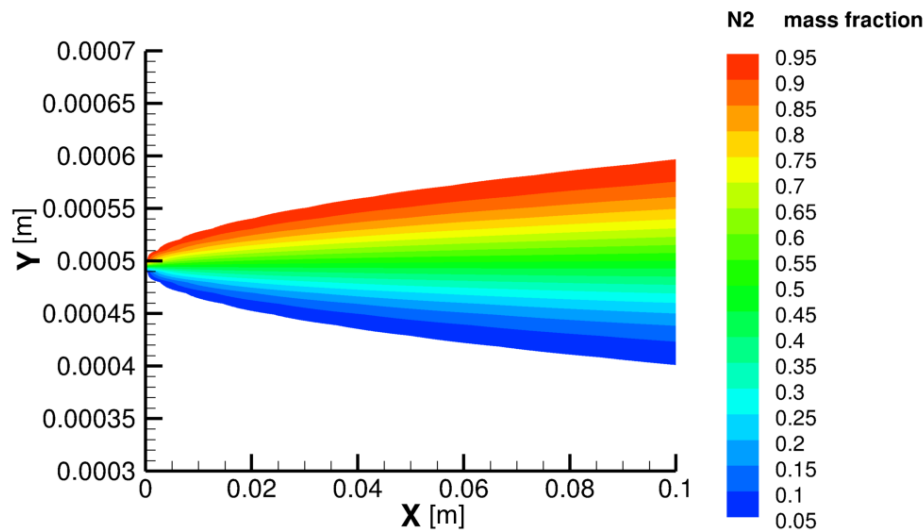
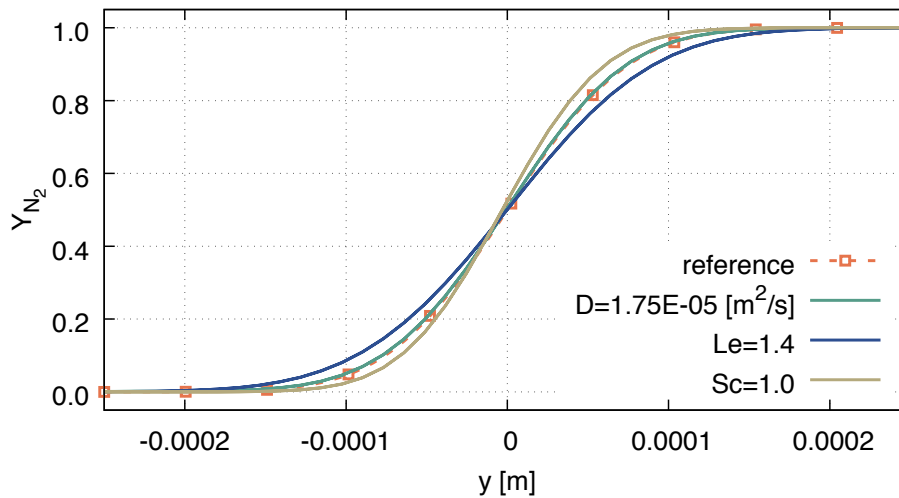


Figure 5.12 - Mass fraction contours of N_2 for zero-shear mixing layer

To compare with the reference solution, the diffusion coefficient was set to a constant of $D = 1.75E-05$ m²/s. The mass fraction profile at the outlet of the channel is plotted in Figure 5.13, with results obtained from the constant diffusion coefficient case as well as the constant Lewis number and constant Schmidt number cases for comparison.



**Figure 5.13 - Mass fraction profile at channel outlet.
Comparison of HALO3D solutions (solid) versus reference (dashed).**

The agreement between the constant coefficient case and the reference solution is shown to be very good. The assumption of a constant Lewis number of 1.4 clearly creates slightly more diffusion due to overestimating the diffusion coefficient, while the constant Schmidt number of 1.0 results in an under prediction. However, the latter models are defined by the user and therefore a range of results is possible. The present case is therefore a demonstration of the capability of these simplified models to predict a comparable amount of diffusion. An additional comparison is made by plotting the mass fraction along the $y = 0.00055$ meter plane, shown in Figure 5.14. Once again, the agreement between the reference and the constant coefficient case is good. However, along the axial direction some discrepancy is seen due to the numerical flux scheme which tends to introduce more artificial dissipation along the axial direction. As previously explained, the constant Lewis number case creates more diffusion and therefore the nitrogen mass fraction begins decreasing much quicker than for the constant diffusion coefficient case. The implemented models are shown to be adequate for viscous hypersonic flows, especially in cases where diffusion coefficient data is not readily available. However, the diffusion coefficient must eventually be modeled using more accurate methods such as Chapman-Enskog theory.

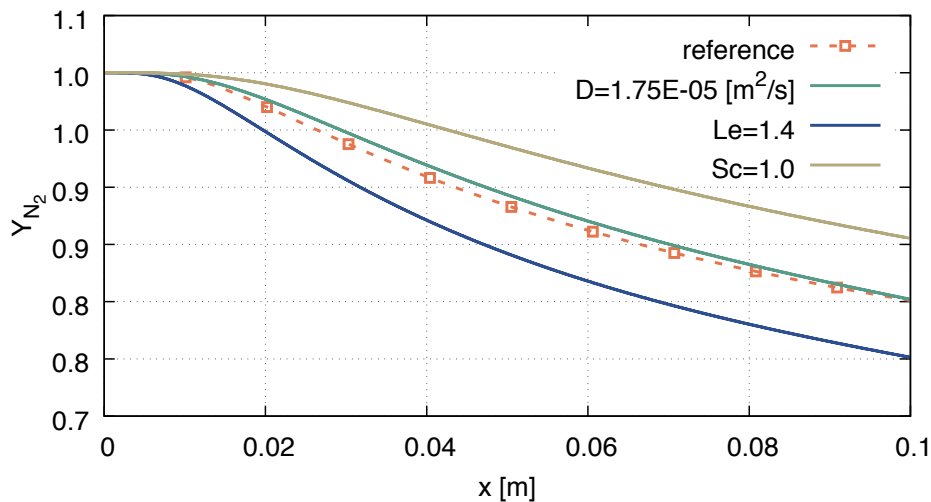


Figure 5.14 - Mass fraction of N_2 along $y=0.00055$ m plane. Comparison between HALO3D (solid) and reference (dashed).

5.5 Viscous Chemical Non-equilibrium Flow Past a Cylinder

With the addition of the viscous terms arising from chemical non-equilibrium, the code is now equipped to simulate viscous flows in chemical non-equilibrium. The present test case consists of high-enthalpy flow past a cylinder and corresponds to the HEGIII experimental flow condition conducted at the high-enthalpy shock tunnel of the German Aerospace Center (DLR) [67]. The experimental model is equipped with pressure transducers and thermocouples on its surface, allowing comparisons to be made with wall values. In addition, simulations were performed by Wasserman et al [68] and Reimann et al [69], allowing comparisons with another numerical code.

The case is referred to as a *high-enthalpy* flow due to its large freestream enthalpy. Though the Mach number is relatively low for hypersonic flows, the large freestream temperature is sufficient to result in a hot shock layer, generating a significant amount of chemical non-equilibrium. The flow conditions are shown in Table 5.4. The Knudsen number is sufficiently low for the continuum assumption to be valid.

Table 5.4 - Flow parameters for high-enthalpy viscous chemical non-equilibrium flow past a cylinder

T_∞ [K]	694	$Y_{N_2,\infty}$	0.7356
P_∞ [Pa]	687	$Y_{O_2,\infty}$	0.1340
u_∞ [m/s]	4776	$Y_{NO,\infty}$	0.0509
M_∞	8.78	$Y_{N,\infty}$	0.0000
R_{cyl} [m]	0.045	$Y_{O,\infty}$	0.07955
Re_∞	2.236E04	kn_∞	5.998E - 04

The chemistry is modelled using Dunn & Kang’s reaction set, found in Appendix B, with the equilibrium reaction rate constants computed using the Gibb’s free energy formulation. The polynomial heat capacity model for a thermally perfect gas is used. The flow is assumed to be in thermal equilibrium to conform with the other numerical simulations. This assumption is justified by Reimann [69] by the fact that the pressure and trans-rotational temperature in the flow field are high, both increasing the rate of relaxation of vibrational energy. Although the experimental model is of finite length, symmetry along the span-wise direction is assumed so that a 2D simulation may be performed. The NIST polynomial model is used for both the viscosity and thermal conductivity, while the diffusion is modelled using a constant Lewis number of $Le = 1.4$. Laminar flow is assumed.

The computational grid and problem setup are shown in Figure 5.15. The mesh consists of 39501 hexahedral elements, resulting in 40000 periodic nodes. The first layer of the mesh has a normalized height of $h/R_{cyl} = 3.6E-04$. The inlet and outlet are modelled as supersonic inlets and outlets, respectively. The wall model requires careful consideration. Since the experimental facility is what is known as an “impulse” facility, the short runtime of the experiment does not allow the model wall to absorb sufficient heat to increase the wall temperature from room temperature. The wall is therefore modelled as an isothermal wall with $T_w = 300$ K. The reference numerical simulations impose a fully catalytic wall condition for the chemistry in which the equilibrium composition for the freestream gas at 300 K is determined using NASA’s CEA program and imposed on the boundary as a pseudo-Dirichlet condition. The present simulation computes the equilibrium composition of the gas at 300 K and the freestream pressure and imposes this composition on the wall. Although this equilibrium calculation should be recomputed at each iteration to take into consideration the surface pressure, it is deemed that the equilibrium composition at 300 K does not vary significantly due to pressure. Thus, this

technique is shown to be sufficient, although future development of the fully catalytic boundary condition in HALO3D is planned.

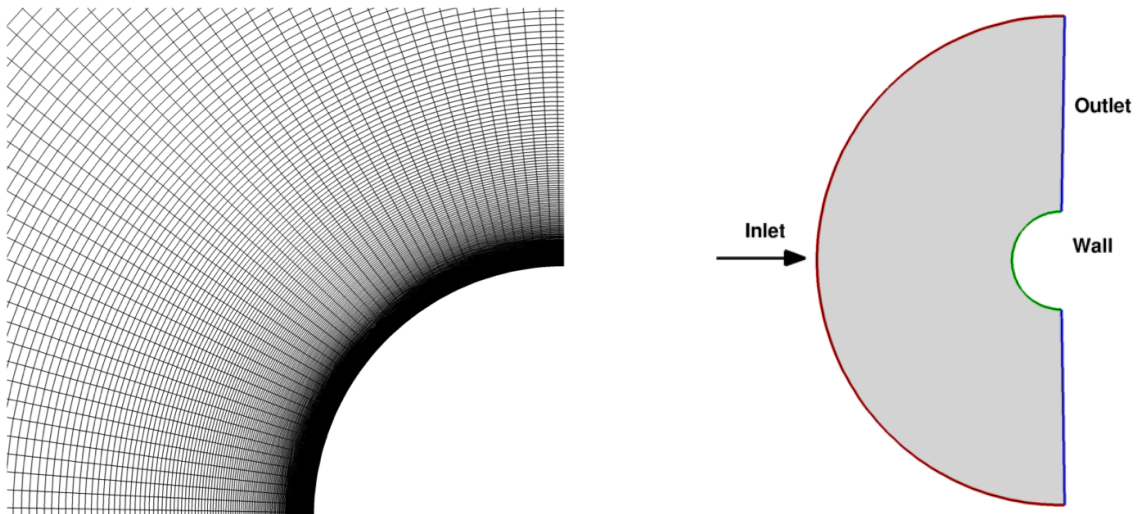


Figure 5.15 - Computational grid (left) and problem setup (right) for high-enthalpy viscous chemical non-equilibrium flow past a cylinder

The simulation is run in parallel on 48 processors. As with the previous cylinder case, an initial first-order solution is obtained and used as a restart condition for the MUSCL-reconstructed solution. The convergence curves are shown in Figure 5.16. As before, good convergence is achieved for both systems. For the second-order solution, although the chemical system stalls, four orders of magnitude of reduction is achieved.

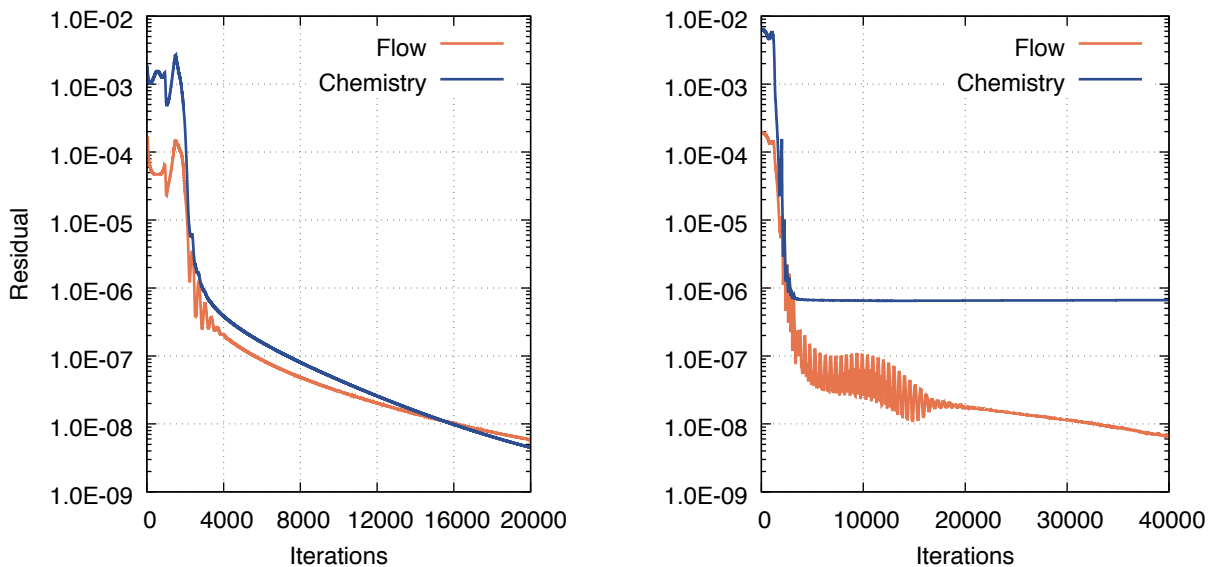


Figure 5.16 - L2 residuals for first-order (left) and second-order (right) solution of high-enthalpy viscous chemical non-equilibrium flow past a cylinder

The temperature along the stagnation line is plotted in Figure 5.17 and compared against numerical results obtained by Wasserman. The computed temperature profile is nearly identical to the reference. The shock standoff position is roughly $\delta/R_{cyl} = 0.260$ and the peak temperature with HALO3D is 7960 K. Good agreement is found with the experimentally measured value of the shock standoff distance is $\delta/R_{cyl} \approx 0.265$ [67]. Some relaxation is seen in the temperature profile behind the shock and a thermal boundary layer near the wall is clearly visible.

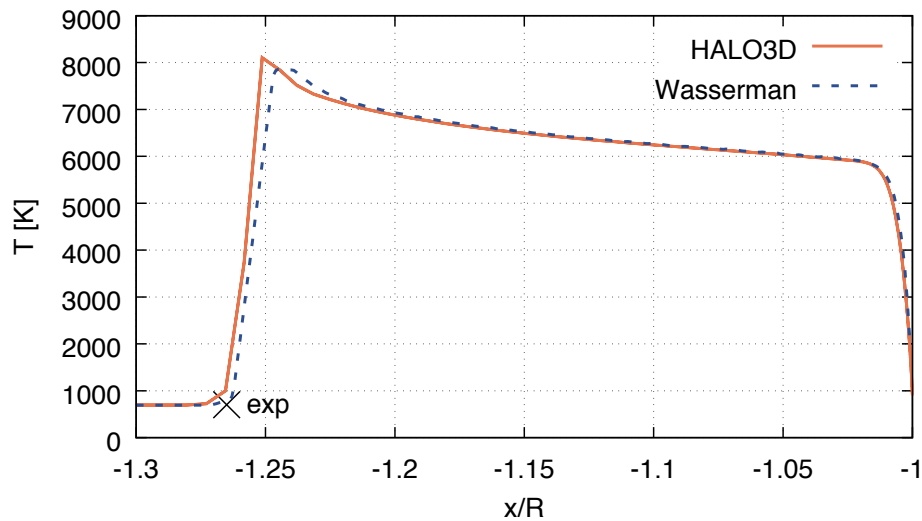


Figure 5.17 - Temperature along stagnation line for high-enthalpy viscous chemical non-equilibrium flow past a cylinder. Comparison between HALO3D (solid) and Wasserman (dashed).

The mass fractions along the stagnation line are plotted in Figure 5.18. The agreement with Wasserman's numerical results is excellent. Once again, most of the diatomic oxygen is dissociated within the shock layer. Since there is already some freestream atomic oxygen available, additional nitric oxide is produced almost immediately after the shock. This nitric oxide undergoes dissociation further into the shock layer, which is evident by the fact that atomic oxygen and nitrogen is produced without much variation in diatomic oxygen and nitrogen. Sharp gradients in the mass fractions can be seen in the boundary layer because of the fully catalytic wall condition, which enforces equilibrium chemistry at the wall. Although this condition is often used, its physical validity for an impulse facility is questionable. Nevertheless, the agreement with the reference solution is found to be good even in the boundary layer.

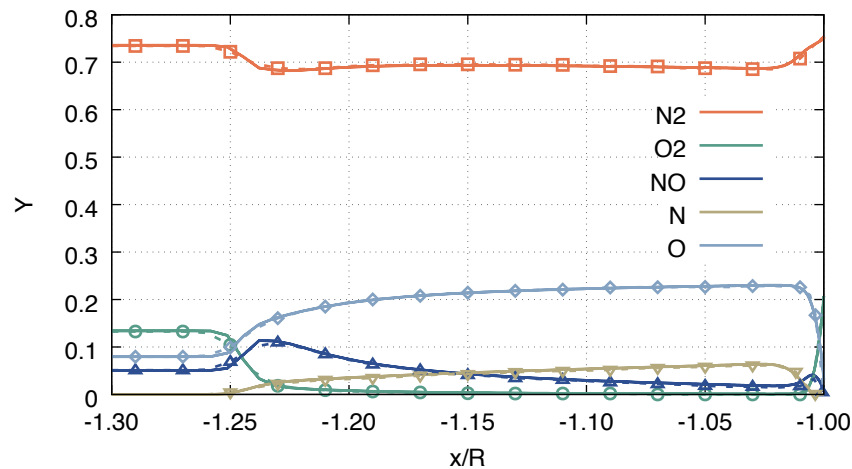


Figure 5.18 - Mass fractions along stagnation line for high-enthalpy viscous chemical non-equilibrium flow past a cylinder. Comparison between HALO3D (solid) and Wasserman (points)

The pressure and heat flux along the cylinder wall in the angular direction are plotted in Figure 5.19. Good agreement for the pressure distribution is seen with the reference result as well as the experiment. HALO3D slightly overestimates the peak heat flux by approximately 15% when compared to Wasserman and by approximately 9% when compared to the experiment. There are minor differences in the physical model that could account for this discrepancy. The present result utilizes NIST polynomial transport properties and a constant Lewis number assumption for the diffusion coefficient, while the reference uses Blottner's model for viscosity, Eucken's relation for conductivity and Chapman-Enskog theory for the diffusion coefficients.

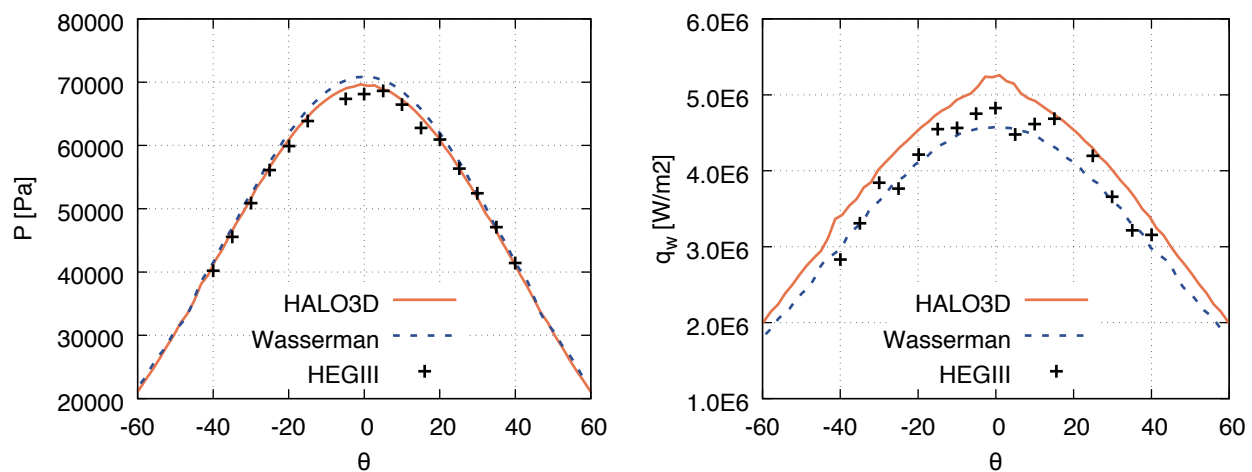


Figure 5.19 - Wall pressure (left) and heat flux (right) for high-enthalpy viscous chemical non-equilibrium flow past cylinder. Comparison between HALO3D (solid), Wasserman (dashed) and HEGIII experimental data (points)

The temperature and pressure contours are plotted in Figure 5.20. Once again, the effect of chemical reactions can clearly be seen in the stagnation region as the temperature decreases immediately behind the shock. Since the flow is viscous, a thermal boundary layer can be seen near the wall. The high pressure in the stagnation region also contributes to increasing the degree of chemical activity, as there is a higher number density of molecules colliding with each other, promoting dissociation.

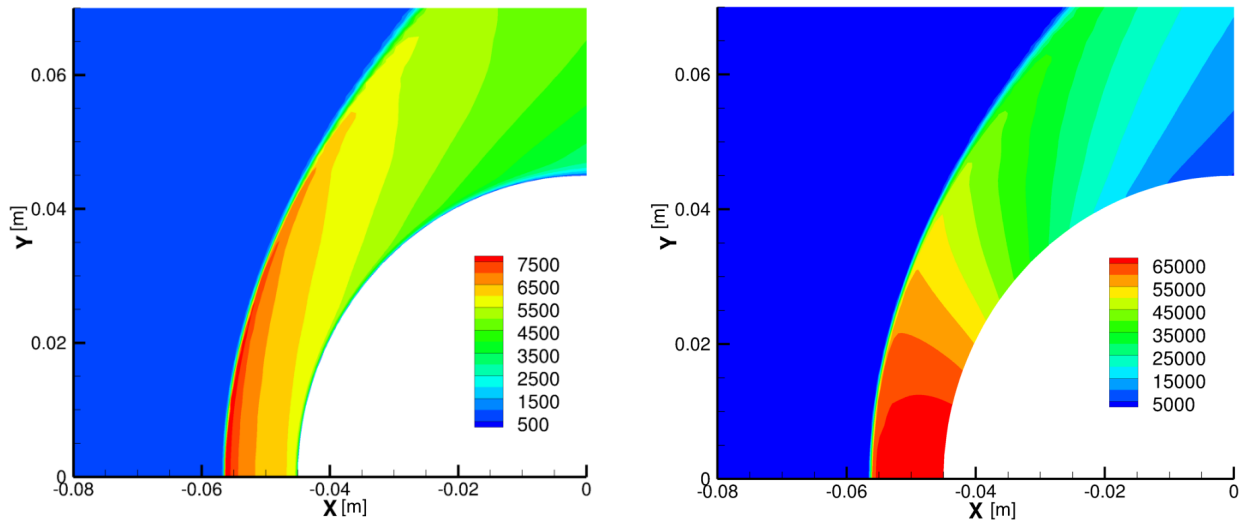


Figure 5.20 - Temperature [K] (left) and pressure [Pa] (right) contours for viscous chemical non-equilibrium flow past cylinder

Finally, sample contours for diatomic nitrogen and nitric oxide are shown in Figure 5.21. It is clear from these plots that the behavior of the chemical species is an extremely complex function of many flow variables. Diatomic nitrogen is partially dissociated immediately after the shock and a significant amount of nitric oxide is formed. However, this nitric oxide is immediately used up to create other species such as atomic oxygen. Due to the high temperature and large residence time in the shock layer, the level of nitric oxide decreases even below the freestream value.

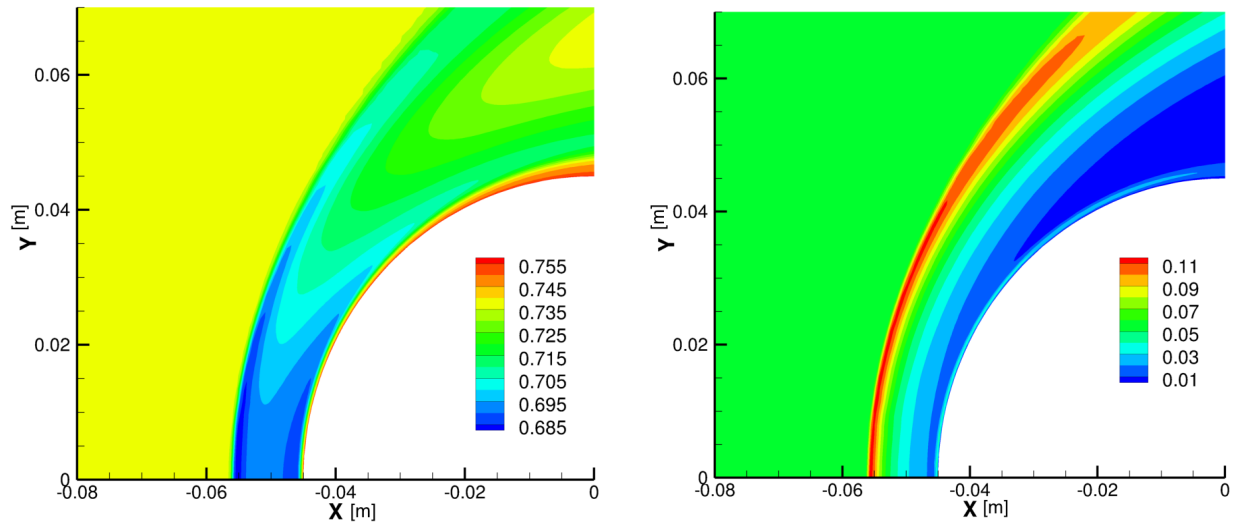


Figure 5.21 - Mass fractions contours of N_2 (left) and NO (right) for viscous chemical non-equilibrium flow past cylinder

5.6 Viscous Thermo-chemical Non-equilibrium Flow Past a Sphere

The final test case presented combines all aspects of hypersonic flows that have been previously examined. Initial investigations on hypersonic flows past a sphere were conducted by Lobb [70] in an experimental setting. Quarter-inch and half-inch spheres were launched into air at various velocities and shadowgraph images were produced, allowing the shock detachment distance and shape to be experimentally determined. Spherical geometries are also extensively studied as they approximate reentry vehicle fore-bodies and noses. This has become a canonical problem for many authors to validate their physical model for hypersonic flows. The volume of results also allows cross-validation between many codes using different models.

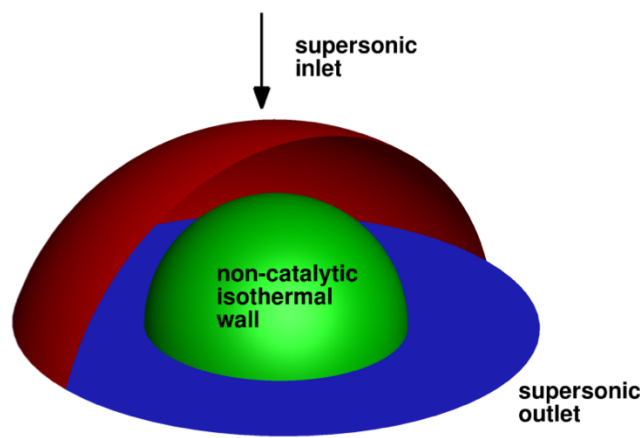


Figure 5.22 - Problem setup for Lobb's sphere

The problem setup for this test case is shown in Figure 5.22. As with the other flow cases, the inlet and outlets are supersonic. The wall is modelled as a non-catalytic isothermal wall with a set wall temperature of 1000 K. The flow parameters may be found in Table 5.5. This case corresponds to the experiment conducted by Lobb with a ½ inch sphere fired at 17315 ft/s. The resulting freestream Mach number is much higher than for previous cases and is sufficiently high to induce significant chemical and thermal non-equilibrium effects. The structured computational grid is shown in Figure 5.23. The mesh consists of 525672 volume elements and 529350 nodes. The first layer of the grid has a normalized height of $h/R_{sphere} = 5.0E - 04$. As before, Roe's scheme is used for flux stabilization with a TVD Van Albada limiter. The flow is assumed to be laminar.

Table 5.5 - Flow parameters for Lobb's sphere

T_∞ [K]	293	$Y_{N_2,\infty}$	0.79
P_∞ [Pa]	673	$Y_{O_2,\infty}$	0.21
u_∞ [m/s]	5263	$Y_{NO,\infty}$	0.00
M_∞	15.3	$Y_{N,\infty}$	0.00
R_{sphere} [m]	0.00635	$Y_{O,\infty}$	0.00
Re_∞	2.648E4	Kn_∞	1.564E - 03
T_w [K]	1000		

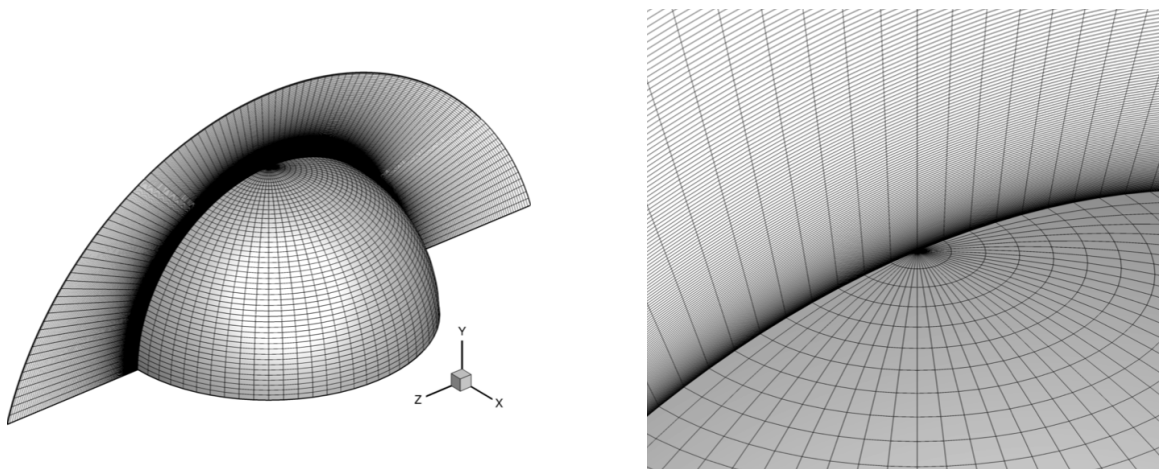


Figure 5.23 - Computational grid (left) and close-up view of near-wall elements (right) for Lobb's sphere

Firstly, results will be presented with comparisons to the CERANS code [64]. In this reference, Park's 1993 reaction model [37] is used, with a vibration-dissociation coupling exponent of 0.5 for the dissociation reactions. The Boltzmann heat model is used without the electronic contribution. The diffusion constant is computed assuming a Lewis number of 1.4 and

the viscosity and thermal conductivity are computed using the Blottner and Eucken models, respectively. The convergence curves for the first and second-order solutions are shown in Figure 5.24. Once again, several orders of reduction in the residuals are seen for both cases, despite a stall in the chemical system during the second-order solution.

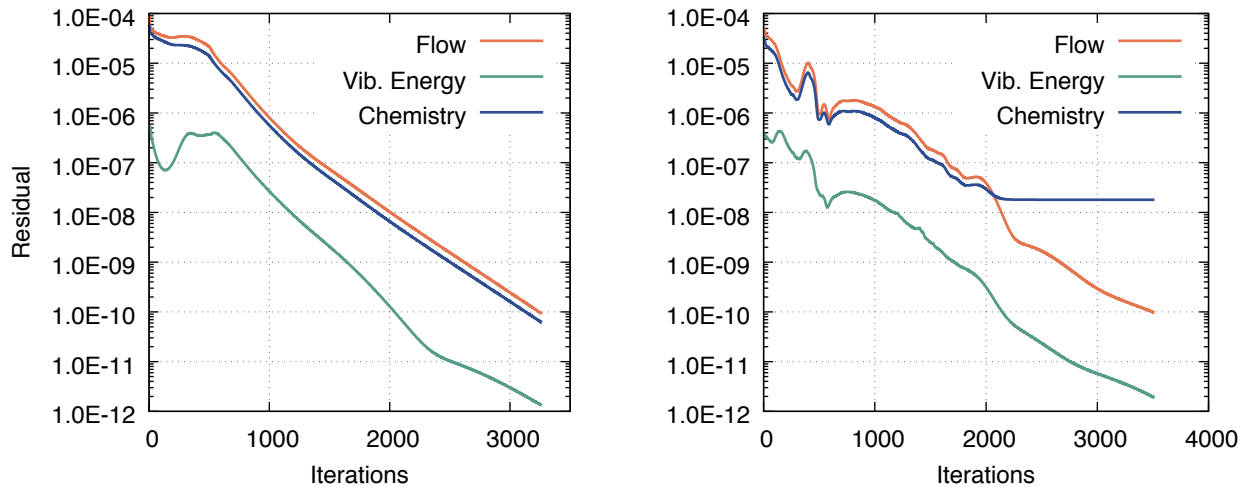


Figure 5.24 - L2 residuals for first order (left) and second order (right) solution of Lobb's sphere

The temperature contours on a cut plane of the flow field are shown in Figure 5.25, where significant differences in the trans-rotational and vibrational-electronic temperatures are seen. The translational temperature is highest just behind the bow shock, followed by relaxation due to chemical reactions. On the other hand, the vibrational temperature is seen to lag the translational temperature. A thin thermal boundary layer is seen in both temperatures due to the cold wall boundary condition.

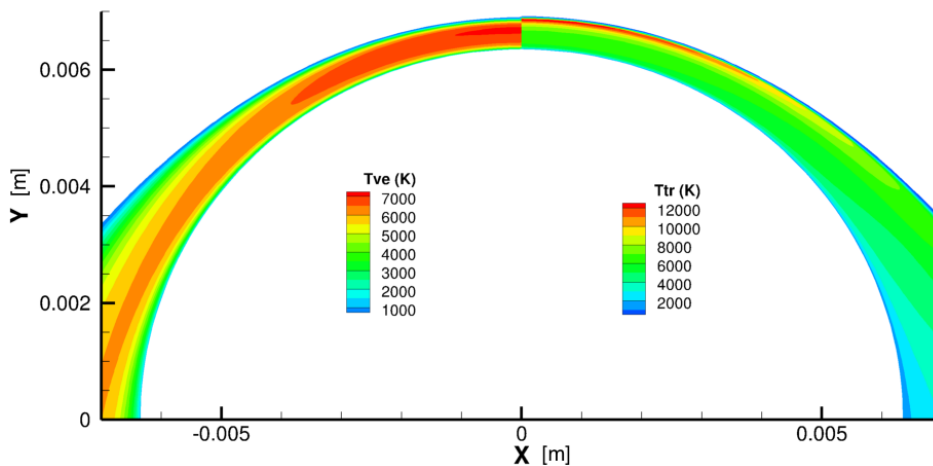


Figure 5.25 - Temperature contours for Lobb's sphere

The pressure in the flow field is shown Figure 5.26, with values below 1000 Pa cutoff for clarity. Experimental shock standoff distances from Lobb's original experiment are also shown, demonstrating that the present simulation captures the shock shape extremely well. It is clear from this plot that the stagnation region, in addition to being extremely hot, is also very dense, reaching over 300 times the freestream pressure.

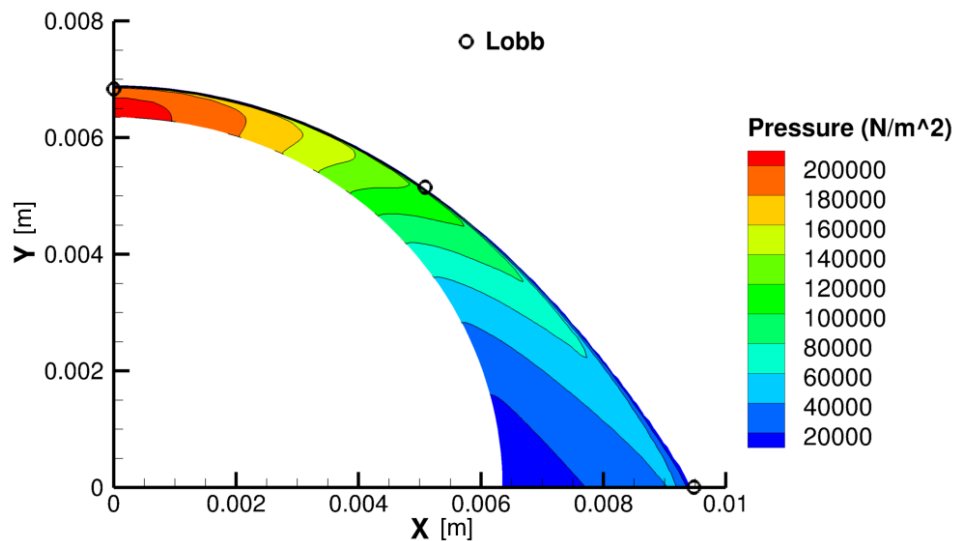


Figure 5.26 - Pressure contours for Lobb's sphere. Comparison with experimental shock locations [71].

The basis used for cross-validation of these types of flows are quantities along the stagnation line, as this is where the most significant non-equilibrium effects take place. Figure 5.27 shows the temperatures along the stagnation, with comparisons made to the numerical results from the CERANS code [64], plotted as dashed lines. Overall, the agreement is quite good, especially in the near-wall region of the shock layer. Both codes predict a shock standoff distance of roughly $\delta/R_{sphere} = 0.085$. Slight disagreement is seen in the post-shock translational temperature and post-shock behavior of the vibrational temperature. This is most likely due to the correction applied to the translation-vibration relaxation source term in [64], which would decrease the relaxation time and therefore allow the vibrational temperature to equilibrate more quickly. The post-shock translational temperature obtained from HALO3D is roughly 12500 K, compared to 14000 K from the numerical reference. Significant relaxation is seen just after the bow shock due to the very high temperatures that encourage dissociation. Moreover, after the relaxation there is a region in which the temperatures no longer vary, indicating that the reactions have proceeded nearly to completion. This effect is common in high

Mach number flows and is the reason many authors report that shock layer conditions are much closer to chemical equilibrium than they are to a chemically frozen flow field.

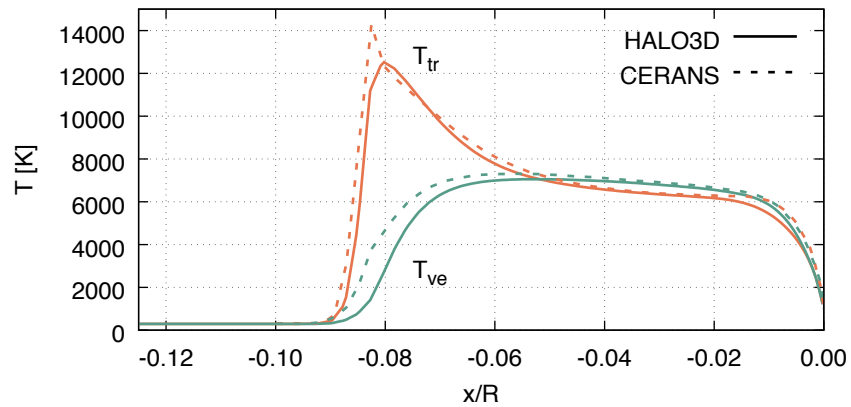


Figure 5.27 - Temperatures along stagnation line for Lobb's sphere

The mass fractions along the stagnation line are plotted in Figure 5.28. Once again, very good agreement is seen. As previously stated, significant chemical non-equilibrium effects may be seen in the shock layer. Roughly 20% of nitrogen by mass is dissociated, and complete dissociation of oxygen occurs. Due to the high temperatures, the presence of nitric oxide is short-lived, and even this molecular species dissociates into atomic oxygen and nitrogen. The effect of the cold wall may be seen through the recombination that occurs in the boundary layer. However, despite the wall temperature being relatively low at 1000 K, the chemical species do not reach equilibrium values at the wall due to the relative influence of mass diffusion. The significant effect of the reaction scheme, diffusion model and transport properties on the resulting gas temperature and heat flux to the wall demonstrates the need for further studies in this area.

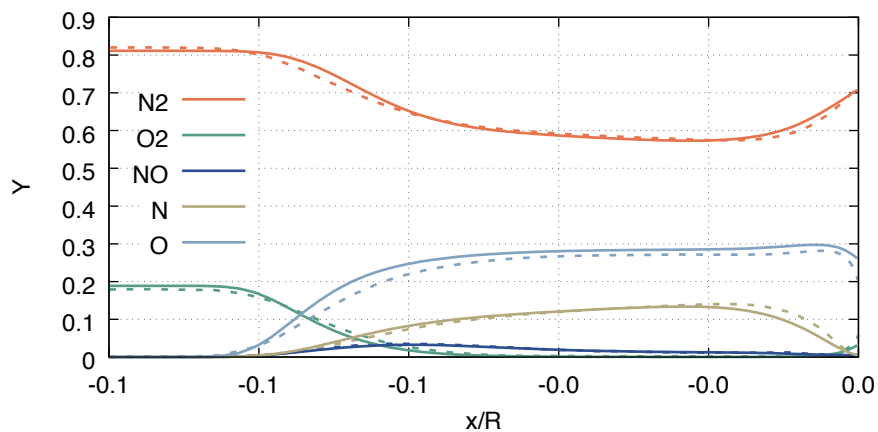


Figure 5.28 - Mass fractions along stagnation line for Lobb's sphere

Comparison of Non-equilibrium Models

A brief demonstration of the effect of the non-equilibrium assumption on the flow field will be presented. The simulation was performed using the above parameters but with different physical assumptions. Firstly, a calorically perfect simulation is conducted, where the gas is neither reacting nor in thermodynamic equilibrium. Next, a thermally perfect gas with frozen chemistry and in thermodynamic equilibrium is simulated. Finally, the results obtained using the chemical and thermodynamic non-equilibrium (TC-NEQ) assumption are compared with the former cases. The stagnation line temperatures are presented in Figure 5.29. The overall trends of what has been discussed are clearly seen. The highest temperature is obtained with the calorically perfect assumption due to the under prediction of the value of the specific heats. With the thermally perfect assumption, the energy content of the gas is more accurately modeled, and the result is a lower peak temperature and a smaller detachment distance due to the lower specific heat ratio [1]. Finally, the assumption of a chemically reacting gas decreases the shock detachment distance further through a combination of increasing the density and pressure ratios and decreasing the temperature ratios across the shock. This occurs due to the freestream kinetic energy being used up by the endothermic dissociation reactions and the pressure rising from the increase in number density [1].

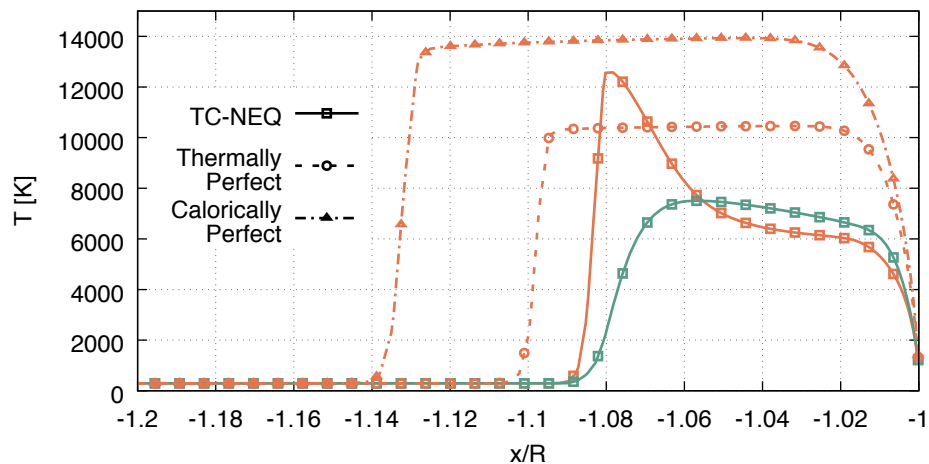


Figure 5.29 - Temperatures along stagnation line for Lobb's sphere. Comparison between calorically perfect, thermally perfect and non-equilibrium physical models.

Comparison of Heat Models

Additional simulations were also performed with the above parameters using three different heat models; the NASA polynomial model, the Boltzmann model including all energy contributions (trve), and the Boltzmann model neglecting electronic energy (trv). The stagnation line temperatures are plotted in Figure 5.30 and very little differences are seen between all three models. The Boltzmann model neglecting electronic energy predicts the highest peak temperature and vibrational temperature, whereas the polynomial model predicts the lowest. This is consistent with the analysis performed in Section 3.2.3, where it was found that the polynomial model tends to predict slightly higher internal energy for a given temperature. Thus, for the same energy, a lower temperature is obtained. The good agreement between models for this case indicates the low level of electronic excitement, which is reported by other authors [71].

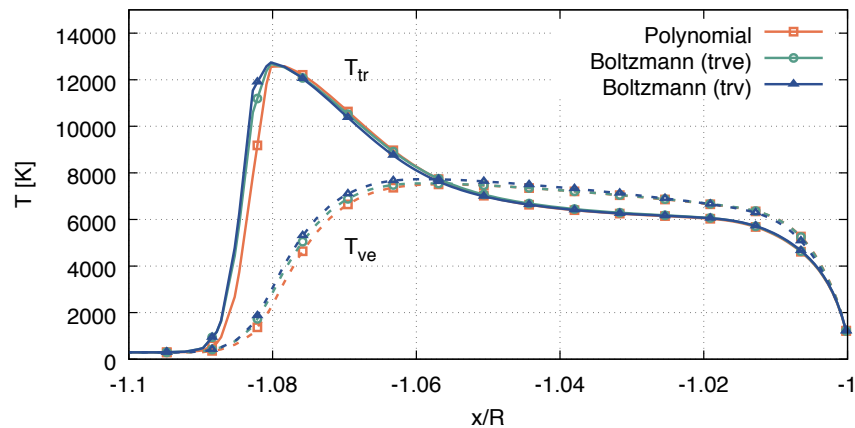


Figure 5.30 - Temperatures along stagnation line for Lobb's sphere. Comparison between polynomial and Boltzmann heat models

Comparison of Reaction Schemes

Finally, a study was conducted on the effect of chemical reactions on the flow field. This highlights the potentially large disagreements found in the Literature on kinetic rates and the resulting disparity in the shock layer predictions. The polynomial heat model is used, and the analytical equilibrium constant is employed, such that we are only comparing the forward reaction rate coefficients. For this study, Park's 1993 model [37], Park's 1985 model [21], Dunn & Kang's model [38] and Hanson's model [39] are compared. The temperatures along the stagnation line are shown in Figure 5.31, and the mass fractions of diatomic nitrogen and oxygen are shown in Figure 5.32.

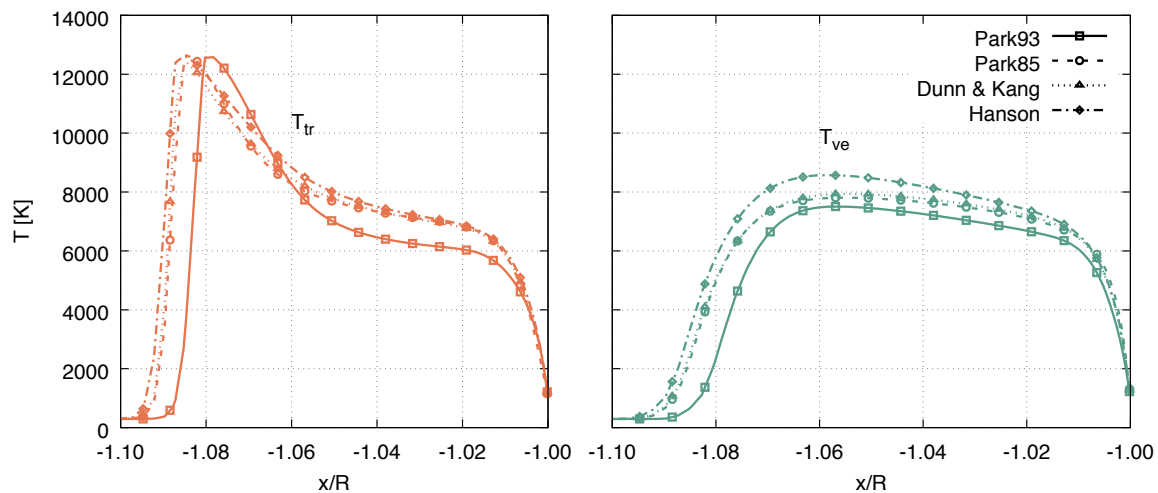


Figure 5.31 - Trans-rotational (left) and vibrational-electronic (right) temperatures along stagnation line for Lobb's sphere. Comparison between various reactions schemes using analytical equilibrium constant

Although the peak temperature is predicted to be the same for all schemes, it can be deduced that the Park 93 reaction scheme may be considered the ‘fastest’, as it produces the smallest shock standoff distance as well as the fastest chemical relaxation effect. The largest shock standoff distance is obtained using Hanson’s model, followed by the Dunn & Kang and Park 85 models. The Park 93 model also nearly reaches the equilibrium chemical state in the shock layer just before the thermal boundary layer. It is seen that the slower reaction schemes tend to predict a larger vibrational-electronic temperature since less molecules are dissociated and therefore a larger component of the internal energy is stored in the vibrational-electronic mode.

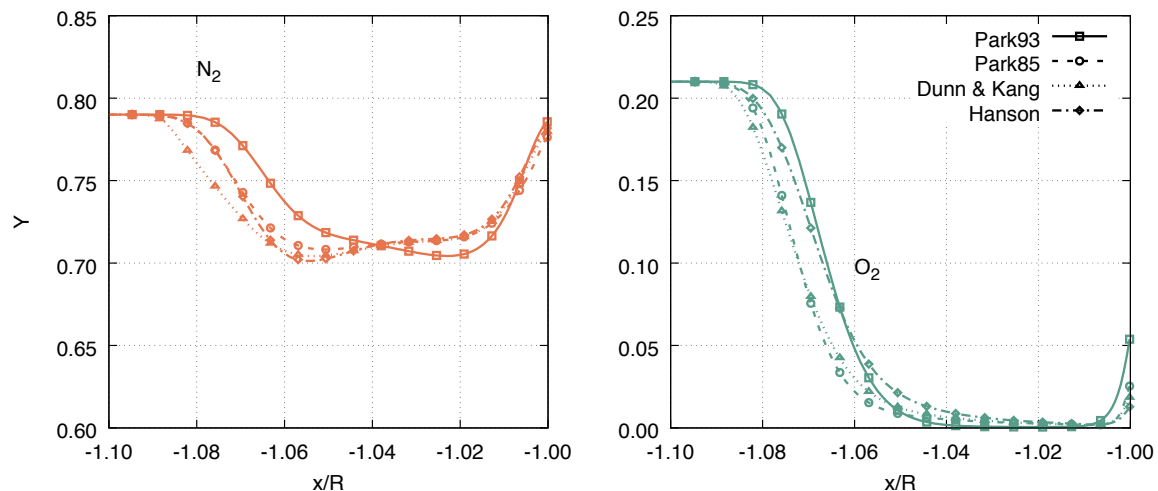


Figure 5.32 - Diatomic nitrogen (left) and oxygen (right) mass fractions along stagnation line for Lobb's sphere. Comparison between various reaction schemes using analytical equilibrium constant

From the mass fraction distributions, we once again see that the Park 93 model is the furthest from the other models. Although the rate of dissociation of diatomic nitrogen is roughly the same as the other models, oxygen is dissociated much faster, and less production of nitric oxide is allowed, resulting in more atomic nitrogen and oxygen than the other models. The Park 93 model also seems to be less dominated by mass diffusion at the wall, demonstrating significantly more recombination due to the stronger reaction rates. Of the other models, Hanson's scheme creates the least amount of dissociation, resulting in more nitric oxide due to dominating exchange reactions, and less atomic nitrogen and oxygen. Not only do these discrepancies manifest themselves in the gas composition and temperatures within the shock layer, the composition at the wall is shown to be vastly different between models. This would result in significantly different heat fluxes and shear stresses and justifies the need for further study and validation of these reaction rates.

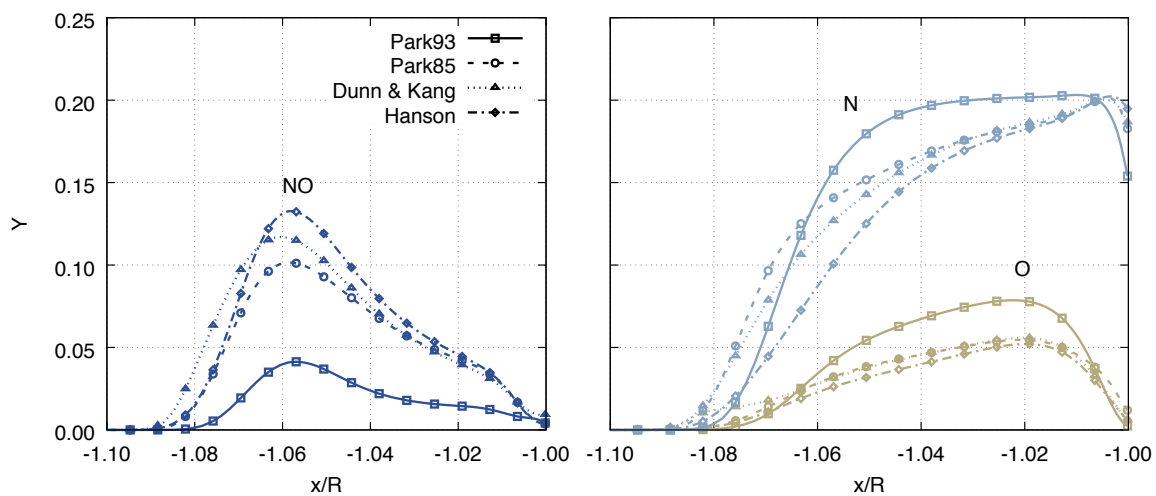


Figure 5.33 - Nitric oxide (left) and atomic nitrogen and oxygen (right) mass fractions along the stagnation line for Lobb's sphere. Comparison between various reaction schemes using analytical equilibrium constant.

6 Conclusions

A loosely-coupled methodology for solving hypersonic flows in the chemical non-equilibrium regime has been presented. The species transport equations are solved in an edge-based FEM framework using a laminar finite-rate chemical reaction model and simplified Fick's law for mass diffusion. The chemical system is solved independently from the flow and thermal system and thermodynamic relations are enforced after every solution step. The loosely-coupled, edge-based methodology proves to be an efficient and flexible framework for the multi-physics HALO3D code.

A systematic series of verification and validation tests were performed on successive components of the chemical non-equilibrium solver. Firstly, the mass production source term was tested on various zero-dimensional reactor cases, including a hydrogen iodide reaction and the high temperature dissociation of air. Both cases are shown to compare extremely well with the Cantera open source chemistry toolkit, demonstrating the ability of the code to simulate unsteady chemical reactions. The effect of chemical relaxation resulting from endothermic chemical reactions was demonstrated. A nitrogen dissociation reactor case was subsequently carried out to verify the thermal non-equilibrium effects and vibration-dissociation coupling models. The number densities of diatomic and atomic nitrogen as well as the trans-rotational and vibrational-electronic temperatures were compared with the hy2foam solver and good agreement is shown for both Park's and the CVDV vibration-dissociation coupling models.

Furthermore, a fuel mixing layer case was used to verify the mass diffusion term, and the mass fraction distribution at the outlet was shown to agree well with the analytical result in the case of a constant diffusion coefficient. The results using constant Lewis number and Schmidt number assumptions was also comparable to the analytical result, indicating the suitability of these assumptions in cases where diffusion coefficient data is not readily available in the literature. Several new mixture transport property models were also implemented, as well as Wilke's mixing rule for the computation of transport properties for a variable composition gas.

Simulations were performed on cylindrical and spherical geometries in thermodynamic and chemical non-equilibrium. These geometries are useful in understanding hypersonic flow fields surrounding leading edges, aircraft noses and reentry vehicle forebodies. Firstly, the simulation of Mach 12.7 inviscid air flowing past an infinite cylinder in thermo-chemical non-equilibrium

was presented. Stagnation line quantities were compared against numerical results obtained by the NASCART-GT code and very good agreement was shown. Appreciable non-equilibrium effects were highlighted in the flow field, such as the dissociation of freestream species, resulting in a decrease of roughly 2000 K in the shock layer temperature. Furthermore, the vibrational temperature lags the translational temperature in the post-shock region, eventually reaching equilibrium closer to the body.

The code was then tested on a viscous, chemical non-equilibrium flow past a cylinder, corresponding to an experiment performed by the HEG facility. Stagnation line quantities were compared to numerical results obtained by Wasserman and extremely good agreement was demonstrated, with both codes predicting roughly 8000 K as the peak temperature. The HALO3D code also predicted an experimental shock standoff distance of $\delta/R_{cyl} \approx 0.265$, as obtained in the experiment. The surface pressure and heat flux were also compared with numerical results as well as experimental results obtained through pressure taps and thermocouples. The surface pressure distribution was in very good agreement, while the surface heat flux was slightly over-predicted in comparison to the references. This is most likely due to the simplified diffusion model, which could alter the amount of recombination occurring in the boundary layer and therefore the heat fluxes to the wall.

Finally, the solver was tested on a viscous, thermo-chemical non-equilibrium flow past a sphere. This case, known as Lobb's sphere, exhibits strong non-equilibrium effects due to the large freestream kinetic energy and the Mach 15.3 flow. Oxygen is completely dissociated and over 20% of nitrogen, by mass, is dissociated in the shock layer. Thermal non-equilibrium is also seen in the hot post-shock region, and some recombination occurs in the boundary layer due to the decreased temperature. Stagnation line quantities are compared with numerical results obtained by the CERANS code and good agreement is obtained, especially in the equilibrium and boundary layer regions. Slight disagreement is seen in the post shock temperatures, which is most likely due to the relaxation time correction applied in the reference, as well as differences in the flux schemes. The shock shape is observed using contours of pressure and is compared to shock standoff distances obtained by Lobb, demonstrating extremely good agreement with the experimental data.

The larger goal of this research programme is to develop a comprehensive aerothermodynamics simulation package for hypersonic flows. At high temperatures, the effects

of ionization cannot be neglected, and thus the consideration of weakly ionized and fully ionized flows must be the focus of future improvements. The development of an MHD solver is already underway in the CFD Lab, and the coupling of this solver with HALO3D could enable the investigation of novel thermal protection systems as well as the simulation of plasmas. Furthermore, the prediction of heat fluxes to the vehicle is highly susceptible to the chemistry model. The investigation of catalytic boundary conditions could provide more flexibility in terms of heating studies on specific surfaces. Improving the mass diffusion model with Chapman-Enskog theory could also enhance the accuracy of heat flux predictions. Finally, the addition of ablation modeling would prove to be a powerful feature for the design of heat shields.

References

- [1] J. Anderson, *Hypersonic and High-Temperature Gas Dynamics*, Virginia: AIAA, 2006.
- [2] R. Seebass, "History and Economics of, and Future Prospects for, Commercial Supersonic Transport," in *Fluid Dynamics Research on Supersonic Aircraft*, RTO Educational Notes 4, 1998.
- [3] C. Anderson, "Rethinking Public-Private Space Travel," *Space Policy*, pp. 266-271, 2013.
- [4] J. O. Arnold, G. L. Seibert and J. F. Wendt, "Real-gas Aerothermodynamics Test Facilities," in *AGARD Advisory Report on Hypersonic Experimental and Computational Capability, Improvement and Validation*, AGARD-AR-319, 1998.
- [5] G. V. Candler, D. J. Mavriplis and L. Treviño, "Current Status and Future Prospects for the Numerical Simulation of Hypersonic Flows," in *47th AIAA Aerospace Sciences Meeting*, AIAA Paper 2009-0153.
- [6] S. Gao, W. G. Habashi, D. Isola, G. S. Baruzzi and M. Fossati, "An Edge-based Galerkin Formulation for Thermal Non-equilibrium Flows," in *2018 AIAA Aerospace Sciences Meeting*, AIAA Paper 2018-0064.
- [7] M. Dumas, W. G. Habashi, D. Isola, G. Baruzzi and M. Fossati, "Finite element modeling of non-equilibrium fluid-wall interaction beyond the continuum regime," *Journal of Aircraft*, 2017.
- [8] J. T. Seguin, W. G. Habashi, D. Isola, G. S. Baruzzi and M. Fossati, "Decoupled Finite-Element Approach for High-Mach Flows with Finite-Rate Chemistry," in *AIAA SciTech Forum*, AIAA Paper 2018-0979.
- [9] D. Knight, J. Longo, D. Drikakis, D. Gaitonde, A. Lani, I. Nompelis and et. al, "Assessment of CFD capability for prediction of hypersonic shock interactions," *Progress in Aerospace Sciences*, vol. 48, pp. 8-26, 2012.
- [10] G. A. Bird, "Monte-Carlo Simulation in an Engineering Context," in *12th International Symposium on Rarefied Gas Dynamics*, 1980.
- [11] H. Sinha, "Effect of Reynolds Number on Detached Eddy Simulation of Hypersonic Base Flows," in *45th AIAA Aerospace Sciences Meeting and Exhibit*, AIAA Paper 2007-1457.
- [12] S. N. A. a. S. Museum, *Gemini Heat Shield, Ablated*, Washington, DC.
- [13] F. A. Williams, *Combustion Theory*, Benjamin/Cummings, 1985.
- [14] K. M. Hanquist and I. D. Boyd, "Computational Analysis of Electron Transpiration Cooling for Hypersonic Vehicles," in *55th AIAA Aerospace Sciences Meeting*, AIAA Paper 2017-0900.
- [15] G. S. R. Sarma, "Physico-Chemical Modelling in Hypersonic Flow Simulation," *Progress in Aerospace Sciences*, vol. 36, pp. 281-349, 2000.
- [16] G. V. Candler, P. K. Subbareddy and I. Nompelis, "Decoupled Implicit Method for Aerothermodynamics and Reacting Flows," *AIAA Journal*, vol. 51, no. 5, pp. 1245-1254, 2013.
- [17] R. T. Davis, "Numerical Solution of the Hypersonic Viscous Shock Layer Equations," *AIAA Journal*, vol. 8, no. 5, pp. 843-851, 1970.
- [18] M. Kim, C. H. Lewis and B. A. Bhutta, "Three-dimensional Effects Upon Real Gas Flows Past the Space Shuttle," AIAA Paper 1984-0225.
- [19] J. Moss and A. Simmonds, "Galileo probe forebody flowfield predictions during Jupiter entry," AIAA Paper 1982-0874.
- [20] J.-H. Lee, "Basic Governing Equations for the Flight Regimes of Aeroassisted Orbital Transfer Vehicles," in *Thermal Design of Aeroassisted Orbital Transfer Vehicles*, AIAA, 1984, pp. 3-53.
- [21] C. Park, "On Convergence of Computation of Chemically Reacting Flows," in *AIAA 23rd Aerospace Sciences Meeting*, AIAA Paper 1985-0247.
- [22] P. A. Gnoffo, R. N. Gupta and J. L. Shinn, "Conservation Equations and Physical Models for Hypersonic Air Flows in Thermal and Chemical Non-Equilibrium," NASA Technical Paper 2867, 1989.
- [23] G. V. Candler and R. W. McCormack, "Computation of Weakly Ionized Hypersonic Flows in Thermochemical Nonequilibrium," *Journal of Thermophysics*, vol. 5, no. 3, pp. 266-273, 1991.
- [24] W. L. Kleb and K. J. Weilmuenster, "Characteristics of the Shuttle Orbiter leeside flow during a re-entry condition," *Journal of Spacecraft and Rockets*, vol. 31, no. 1, pp. 8-16, 1994.
- [25] G. V. Candler, M. J. Wright and J. D. McDonald, "Data-parallel lower-upper relaxation method for reacting

References

- flows," *AIAA Journal*, vol. 32, no. 12, pp. 2380-2386, 1994.
- [26] H. Alkandry, I. D. Boyd and A. Martin, "Comparison of Models for Mixture Transport Properties for Numerical Simulations of Ablative Heat-Shields," in *51st AIAA Aerospace Sciences Meeting*, AIAA Paper 2013-0303.
- [27] T. Gökçen and R. W. MacCormack, "Nonequilibrium effects for hypersonic transitional flows using continuum approach," in *27th Aerospace Sciences Meeting*, AIAA Paper 1989-0461.
- [28] M. Barbato, D. Giordano, J. Muylaert and C. Bruno, "Comparison of catalytic wall conditions for hypersonic flow," *Journal of Spacecraft and Rockets*, vol. 33, no. 5, pp. 620-627, 1996.
- [29] R. Upadhyay, P. T. Bauman, R. Stogner, K. W. Schulz and O. Ezekoye, "Steady-State Ablation Model Coupling with Hypersonic Flow," in *48th AIAA Aerospace Sciences Meeting*, AIAA Paper 2010-1176.
- [30] W. A. Wood, "Radiation Coupling with the FUN3D Unstructured-Grid CFD Code," in *43rd AIAA Thermophysics Conference*, AIAA Paper 2012-2741.
- [31] R. Löhner, *Applied Computational Fluid Dynamics Techniques: An Introduction Based on Finite Element Methods*, John Wiley & Sons, Ltd, 2008.
- [32] P. K. Nag, *Engineering Thermodynamics*, Tata McGraw-Hill Education, 2005.
- [33] B. J. McBride, S. Gordon and M. A. Reno, "Coefficients for Calculating Thermodynamic and Transport Properties of Individual Species," NASA, 1993.
- [34] C. Park, *Nonequilibrium Hypersonic Aerothermodynamics*, New York: Wiley, 1990.
- [35] R. P. Fedkiw, B. Merriman and S. Osher, "High Accuracy Numerical Methods for Thermally Perfect Gas Flows with Chemistry," *Journal of Computational Physics*, vol. 132, pp. 175-190, 1997.
- [36] S. K. Upadhyay, *Chemical Kinetics and Reaction Dynamics*, Springer-Anamaya, 2006.
- [37] C. Park, "Review of Chemical-Kinetic Problems of Future NASA Missions, I: Earth Entries," *Journal of Thermophysics and Heat Transfer*, vol. 7, no. 3, 1993.
- [38] M. G. Dunn and S.-W. Kang, "Theoretical and Experimental Studies of Reentry Plasmas," NASA CR-2232, 1973.
- [39] R. K. Hanson and S. Salimian, "Survey of Rate Constants in the N/H/O System," in *Combustion Chemistry*, Springer-Verlag, 1984.
- [40] L. C. Scalabrin, "Numerical Simulation of Weakly Ionized Hypersonic Flow over Reentry Capsules," PhD Thesis, 2007.
- [41] C. E. Treanor and P. V. Marrone, "Effect of Dissociation on the Rate of Vibrational Relaxation," *Physics of Fluids*, vol. 5, no. 9, pp. 1022-1026, 1962.
- [42] A. W. Cook, "Enthalpy Diffusion in Multicomponent Flows," *Physics of Fluids*, vol. 21, 2009.
- [43] O. C. Zienkiewicz, R. L. Taylor and J. Z. Zhu, *The Finite Element Method: Its Basis and Fundamentals*, Elsevier, 2005.
- [44] D. Isola, "Equivalence Conditions between Continuous Linear Finite Element and Finite Volume Discretizations of Non-Simplicial Elements," in *23rd AIAA Computational Fluid Dynamics Conference*, AIAA Paper 2017-4276.
- [45] H. Luo, J. D. Baum and R. Löhner, "Edge-Based Finite Element Scheme for the Euler Equations," *AIAA Journal*, vol. 32, no. 6, pp. 1183-1190, 1994.
- [46] V. Selmin, "The Node-centered Finite Volume Approach: Bridge Between Finite Differences and Finite Elements," *Compute Methods in Applied Mechanics and Engineering*, vol. 102, pp. 107-138, 1993.
- [47] P. L. Roe, "Approximate Riemann Solvers, Parameter Vectors, and Difference Schemes," *Journal of Computational Physics*, vol. 43, pp. 357-372, 1981.
- [48] A. Harten, "High resolution schemes for hyperbolic conservation laws," *Journal of Computational Physics*, vol. 49, no. 3, pp. 357-393, 1983.
- [49] M.-S. Liou and C. J. Steffen, "A New Flux Splitting Scheme," *Journal of Computational Physics*, vol. 107, no. 1, pp. 23-39, 1993.
- [50] B. Van Leer, "Towards the Ultimate Conservative Difference Scheme. V. A Second-Order Sequel to

References

- Godunov's Method," *Journal of Computational Physics*, vol. 32, pp. 101-136, 1979.
- [51] M.-S. Liou, "A Sequel to AUSM, Part II: AUSM+-up for all speeds," *Journal of Computational Physics*, vol. 214, pp. 137-170, 2006.
- [52] B. Larrouturou, "How to Preserve the Mass Fractions Positivity when Computing Compressible Multi-component Flows," *Journal of Computational Physics*, vol. 95, pp. 59-84, 1991.
- [53] P. K. Sweby, "High Resolution Schemes Using Flux Limiters for Hyperbolic Conservation Laws," *SIAM Journal on Numerical Analysis*, vol. 21, no. 5, pp. 995-1011, 1984.
- [54] J. N. Scott and Y.-Y. Niu, "Comparison of Limiters in Flux-Split Algorithms for Euler Equations," in *31st Aerospace Sciences Meeting & Exhibit*, AIAA Paper 1993-0068.
- [55] J. Shuen, K. Chen and Y. Choi, "A Coupled Implicit Method for Chemical Non-Equilibrium Flows at All Speeds," *Journal of Computational Physics*, vol. 106, pp. 306-318, 1993.
- [56] M. Kloker, M. Borsboom and R. Van den Braembussche, "A Fully Implicit Scheme for Unsteady Flow Calculations Solved by the Approximate Factorization Technique," Von Karman Institute for Fluid Dynamics, Project Report 1986-16.
- [57] S. Balay, W. D. Gropp, I. C. McInnes and B. F. Smith, "Efficient Management of Parallelism in Object Oriented Numerical Software Libraries," in *Modern Software Tools in Scientific Computing*, 1997, pp. 1670-1680.
- [58] J. A. Fay and F. R. Riddell, "Theory of Stagnation Point Heat Transfer in Dissociated Air," *Journal of the Aeronautical Sciences*, vol. 25, no. 2, pp. 73-85, 1958.
- [59] J. A. Manion and et al, "Chemical Kinetics Database," NIST, 2015. [Online]. Available: <https://kinetics.nist.gov/>.
- [60] T. J. Scanlon, C. White, M. K. Borg, R. C. Palharini, E. Farbar, I. D. Boyd, J. M. Reese and R. E. Brown, "Open-Source Direct Simulation Monte Carlo Chemistry Modeling for Hypersonic Flows," *AIAA Journal*, vol. 53, no. 6, pp. 1670-1680, 2015.
- [61] D. G. Goodwin, H. K. Moffat and R. L. Speth, "Cantera: An object- oriented software toolkit for chemical kinetics, thermodynamics, and transport processes," <http://www.cantera.org>, 2017.
- [62] V. Casseau, D. Espinoza, T. J. Scanlon and R. E. Brown, "A Two-Temperature Open-Source CFD Model for Hypersonic Reacting Flows, Part One: Zero-Dimensional Analysis," *Aerospace*, vol. 3, no. 34, 2016.
- [63] I. Nompelis, G. V. Candler and S. M. Holden, "Effect of Vibrational Non-Equilibrium on Hypersonic Double-cone Experiments," *AIAA Journal*, vol. 41, no. 11, pp. 2162-2169, 2003.
- [64] R. Balasubramanian and K. Anandhanarayanan, "Development of a Thermo-chemical Non-equilibrium Solver for Hypervelocity Flows," *Journal of The Institution of Engineers (India)*, vol. 96, no. 2, pp. 119-134, 2015.
- [65] J. W. Lee, "Unstructured Cartesian-grid Methodology for Non-Equilibrium Hypersonic Flows," in *AIAA Thermophysics conference*, AIAA Paper 2007-4548.
- [66] W. H. Heiser and D. T. Pratt, Hypersonic Airbreathing Propulsion, Ohio: AIAA Education Series, 1994.
- [67] S. Karl, J. Martinez-Schramm and K. Hannemann, "High Enthalpy Cylinder Flow in HEG: a basis for CFD validation," in *44th AIAA Fluid Dynamics Conference*, AIAA Paper 2003-4252.
- [68] M. Wasserman, B. Greenberg and Y. Levy, "A Robust Numerical Method for the Simulation of Chemically Reacting Flows," in *56th Israel Annual Conference on Aerospace Sciences*, 2016.
- [69] B. Reimann and V. Hannemann, "Numerical Investigation of Double-Cone and Cylinder Experiments in High Enthalpy Flows using the DLR Tau Code," in *48th AIAA Aerospace Sciences Meeting*, AIAA Paper 2010-1282.
- [70] R. K. Lobb, "Experimental Measurement of Shock Detachment Distance on Spheres Fired in Air at Hypervelocities," in *AGARD-NATO Specialists' Meeting*, 1962.
- [71] A. Prakash, N. Parsons, X. Wang and X. Zhong, "High-Order Shock-Fitting Methods for Hypersonic Flow with Chemical and Thermal Non-equilibrium," in *40th Fluid Dynamics Conference and Exhibit*, AIAA Paper 2010-4997.
- [72] V. Selmin and L. Formaggia, "Unified Construction of Finite Element and Finite Volume Discretizations for Compressible Flows," *International Journal for Numerical Methods in Engineering*, vol. 39, pp. 1-32, 1996.

Appendix A: Species data**Species thermodynamic data**

species	M_s [kg/m ³]	h_f^0 [J/kg]	θ_v [K]
N_2	28	0	3395
O_2	32	0	2239
NO	30	3.00E06	2817
N	14	3.36E06	0
O	16	1.54E07	0

Appendix B: Chemical models

Park's Model (1985) [21]:

Reaction	M	A_f	η_f	E_a/R_u
$N_2 + M \rightleftharpoons 2N + M$	N_2	3.70E21	-1.60	113200
	O_2	3.70E21	-1.60	113200
	NO	3.70E21	-1.60	113200
	N	1.11E22	-1.60	113200
	O	1.11E22	-1.60	113200
$O_2 + M \rightleftharpoons 2O + M$	N_2	2.75E19	-1.00	59500
	O_2	2.75E19	-1.00	59500
	NO	2.75E19	-1.00	59500
	N	8.25E19	-1.00	59500
	O	8.25E19	-1.00	59500
$NO + M \rightleftharpoons N + O + M$	N_2	2.30E17	-0.50	75500
	O_2	2.30E17	-0.50	75500
	NO	2.30E17	-0.50	75500
	N	4.60E17	-0.50	75500
	O	4.60E17	-0.50	75500
$NO + O \rightleftharpoons N + O_2$	-	2.16E08	1.29	19220
$O + N_2 \rightleftharpoons N + NO$	-	3.18E13	0.10	37200

$K_{eq}(z) = \exp(B_1 + B_2z + B_3z^2 + B_4z^3 + B_5z^4)$					
Reaction	B_1	B_2	B_3	B_4	B_5
$N_2 + M \rightleftharpoons 2N + M$	1.335	-4.127	-0.616	0.093	-0.005
$O_2 + M \rightleftharpoons 2O + M$	3.898	-12.611	0.683	-0.118	0.006
$NO + M \rightleftharpoons N + O + M$	1.549	-7.784	0.228	-0.043	0.002
$NO + O \rightleftharpoons N + O_2$	0.215	-3.657	0.843	-0.136	0.007
$O + N_2 \rightleftharpoons N + NO$	2.349	-4.828	0.455	-0.075	0.004

Park's Model (1993) [37]:

Reaction	M	A_f	η_f	E_a/R_u
$N_2 + M \rightleftharpoons 2N + M$	N_2	7.00E21	-1.60	113200
	O_2	7.00E21	-1.60	113200
	NO	7.00E21	-1.60	113200
	N	3.00E21	-1.60	113200
	O	3.00E21	-1.60	113200
$O_2 + M \rightleftharpoons 2O + M$	N_2	2.00E21	-1.50	59500
	O_2	2.00E21	-1.50	59500
	NO	2.00E21	-1.50	59500
	N	1.00E22	-1.50	59500
	O	1.00E22	-1.50	59500
$NO + M \rightleftharpoons N + O + M$	N_2	5.00E15	0.00	75500
	O_2	5.00E15	0.00	75500
	NO	5.00E15	0.00	75500
	N	1.10E17	0.00	75500
	O	1.10E17	0.00	75500
$NO + O \rightleftharpoons N + O_2$	-	8.40E12	0.00	19450
$O + N_2 \rightleftharpoons N + NO$	-	6.40E17	-1.00	38400

$$K_{eq}(z) = \exp\left(\frac{B_1}{z} + B_2 + B_3 \ln z + B_4 z + B_5 z^2\right)$$

Reaction	B_1	B_2	B_3	B_4	B_5
$N_2 + M \rightleftharpoons 2N + M$	1.4766	1.6291	1.2153	-11.457	-0.009444
$O_2 + M \rightleftharpoons 2O + M$	0.50989	2.4773	1.7132	-6.5441	0.02959
$NO + M \rightleftharpoons N + O + M$	0.50765	0.73575	0.48042	-7.4979	-0.016247
$NO + O \rightleftharpoons N + O_2$	-0.002428	-1.7415	-1.2331	-0.95365	-0.04585
$O + N_2 \rightleftharpoons N + NO$	0.96921	0.89329	0.73531	-3.9596	0.006818

Dunn and Kang Model [38]:

Reaction	M	A_f	η_f	$E_{a,f}/R_u$	A_b	η_b	$E_{a,b}/R_u$
$N_2 + M \rightleftharpoons 2N + M$	N_2	4.70E17	-0.50	11300	2.72E16	-0.50	0
	O_2	1.90E17	-0.50	11300	1.10E16	-0.50	0
	NO	1.90E17	-0.50	11300	1.10E16	-0.50	0
	N	4.085E22	-1.50	11300	2.27E21	-1.50	0
	O	1.90E17	-0.50	11300	1.10E16	-0.50	0
$O_2 + M \rightleftharpoons 2O + M$	N_2	7.20E18	-1.00	59500	6.00E15	-0.50	0
	O_2	3.24E19	-1.00	59500	2.70E16	-0.50	0
	NO	3.60E18	-1.00	59500	3.00E15	-0.50	0
	N	3.60E18	-1.00	59500	3.00E15	-0.50	0
	O	9.00E19	-1.00	59500	7.50E16	-0.50	0
$NO + M \rightleftharpoons N + O + M$	N_2	3.90E20	-1.50	75500	1.00E20	-1.50	0
	O_2	3.90E20	-1.50	75500	1.00E20	-1.50	0
	NO	7.80E21	1.50	75500	2.00E21	-1.50	0
	N	7.80E21	1.50	75500	2.00E21	-1.50	0
	O	7.80E21	1.50	75500	2.00E21	-1.50	0
$NO + O \rightleftharpoons N + O_2$	-	3.20E09	1.00	19700	1.30E10	1.00	35800
$O + N_2 \rightleftharpoons N + NO$	-	7.00E13	0.00	38000	1.56E13	0.00	0

Hanson's Model [39]:

Reaction	M	A_f	η_f	E_a/R_u
$N_2 + M \rightleftharpoons 2N + M$	N_2	3.70E21	-1.60	113200
	O_2	1.40E21	-1.60	113200
	NO	1.40E21	-1.60	113200
	N	1.60E22	-1.60	113200
	O	1.40E21	-1.60	113200
$O_2 + M \rightleftharpoons 2O + M$	N_2	3.64E18	-1.00	59380
	O_2	1.64E19	-1.00	59380
	NO	1.82E18	-1.00	59380
	N	1.82E18	-1.00	59380
	O	4.56E19	-1.00	59380
$NO + M \rightleftharpoons N + O + M$	N_2	4.00E20	-1.50	75500
	O_2	4.00E20	-1.50	75500
	NO	8.00E21	-1.50	75500
	N	8.00E21	-1.50	75500
	O	8.00E21	-1.50	75500
$NO + O \rightleftharpoons N + O_2$	-	3.80E09	1.00	20820
$O + N_2 \rightleftharpoons N + NO$	-	1.82E14	0.00	38370

Scanlon's Model [60]:

Reaction	M	A_f	η_f	E_a/R_u
$N_2 + M \rightarrow 2N + M$	N_2	2.47E18	-0.62	113176
	O_2	9.03E18	-0.68	113176
	NO	9.03E18	-0.68	113176
	N	6.022E18	-0.68	113176
	O	2.41E18	-0.54	113176
$O_2 + M \rightarrow 2O + M$	N_2	7.83E19	-1.00	59418
	O_2	3.21E19	-1.00	59418
	NO	6.62E19	-1.50	59418
	N	1.82E18	-1.00	59418
	O	9.03E19	-1.00	59418
$NO + M \rightarrow N + O + M$	N_2	1.26E20	-1.00	75531
	O_2	1.20E20	-1.00	75531
	NO	6.02E19	-1.00	75531
	N	2.41E20	-1.10	75531
	O	2.41E20	-1.10	75531
$NO + O \rightarrow N + O_2$	-	1.39E11	0.50	19243
$O + N_2 \rightarrow N + NO$	-	4.82E13	0.00	37525
$O_2 + N \rightarrow NO + O$	-	2.41E15	-0.39	1443
$NO + N \rightarrow N_2 + O$	-	3.01E14	-0.35	1443

Appendix C: Derivation of Jacobian Matrices

The Jacobian matrices for a one-dimensional set of species conservation equations will be presented. Recall that the decoupled chemical is given by

$$\frac{\partial \mathbf{Q}}{\partial t} + \frac{\partial (\mathbf{F}^i - \mathbf{F}^v)}{\partial x} = \mathbf{S}$$

Where the chemical conservative variables vector \mathbf{Q} , the inviscid flux vector \mathbf{F}^i , the viscous flux vector \mathbf{F}^v and the chemical source term vector \mathbf{S} are given by

$$\mathbf{Q} = \begin{Bmatrix} \rho_1 \\ \rho_2 \\ \dots \\ \rho_{N_s} \end{Bmatrix}, \quad \mathbf{F}^i = \begin{Bmatrix} \rho_1 u \\ \rho_2 u \\ \dots \\ \rho_{N_s} u \end{Bmatrix}, \quad \mathbf{F}^v = \begin{Bmatrix} J_1 \\ J_2 \\ \dots \\ J_{N_s} \end{Bmatrix}, \quad \mathbf{S} = \begin{Bmatrix} \dot{\omega}_1 \\ \dot{\omega}_2 \\ \dots \\ \dot{\omega}_{N_s} \end{Bmatrix}$$

The chemical primitive variables vector is defined as the set of mass fractions, $\mathbf{Y} = \{Y_1, Y_2, \dots, Y_{N_s}\}^T$. In the absence of chemical source terms (frozen flow), the set of species conservation equations is linear. The following simple Jacobian matrices are obtained

$$\frac{\partial \mathbf{Q}}{\partial \mathbf{Y}} = \rho \mathbf{I}, \quad \frac{\partial \mathbf{Y}}{\partial \mathbf{Q}} = \frac{1}{\rho} \mathbf{I}, \quad \frac{\partial \mathbf{F}^i}{\partial \mathbf{Y}} = \rho u \mathbf{I}, \quad \frac{\partial \mathbf{F}^i}{\partial \mathbf{Q}} = u \mathbf{I}$$

Jacobian of Chemical Source Term

Recall that the chemical source term vector is given by

$$S_s = M_s \sum_{r=1}^{N_r} (v''_{s,r} - v'_{s,r}) R_r, \quad \text{where } R_r = R_{f,r} - R_{b,r}$$

Note that $R_r = R_r(\mathbf{C}, \mathbf{Y}, T_{tr}, T_{ve})$, where T_{tr} and T_{ve} are the trans-rotational and vibrational-electronic temperatures, respectively, and \mathbf{C} is the conservative flow variables vector

$$\mathbf{C} = \{\rho, \rho u, \rho v, \rho w, \rho e\}^T$$

Recall that

$$R_{f,r}(\mathbf{C}, \mathbf{Y}, T_{tr}, T_{ve}) = k_{fr}(T_c) \prod_{i=1}^{N_s} \left(\frac{\rho Y_i}{M_s} \right)^{v'_{i,r}}$$

$$R_{b,r}(\mathbf{C}, \mathbf{Y}, T_{tr}) = k_{br}(T_{tr}) \prod_{i=1}^{N_s} \left(\frac{\rho Y_i}{M_i} \right)^{v''_{i,r}}$$

The chemical system is solved assuming that the gasdynamic and thermodynamic variables are held constant. The entries in the Jacobian are therefore defined as

$$\frac{\partial S_s}{\partial Q_i} = \left[\frac{\partial S_s}{\partial Y_i} \right]_{C, Y_s \neq Y_i, T_{tr}, T_{ve}} \left[\frac{\partial Y_i}{\partial Q_i} \right] = M_s \sum_{r=1}^{N_r} \left[(v''_{s,r} - v'_{s,r}) \left[\frac{\partial R_r}{\partial Y_i} \right]_{C, Y_s \neq Y_i, T_{tr}, T_{ve}} \right] \frac{1}{\rho}$$

The derivative of the reaction rate R_r with respect to mass fraction Y_i must be taken with partial derivatives as follows

$$\left[\frac{\partial R_r}{\partial Y_i} \right]_{C, Y_s \neq Y_i, T_{tr}, T_{ve}} = \sum_{j=1}^{N_s} \left[\frac{\partial R_r}{\partial Y_j} \right]_{C, Y_s \neq Y_i, T_{tr}, T_{ve}} \left[\frac{\partial Y_j}{\partial Y_i} \right]$$

Firstly, we will derive the reaction rate R_r with respect to the mass fraction Y_j

$$\left[\frac{\partial R_r}{\partial Y_j} \right]_{C, Y_s \neq Y_j, T} = k_{fr} \frac{\partial}{\partial Y_j} \left[\prod_{l=1}^{N_s} \left(\frac{\rho Y_l}{M_l} \right)^{v'_{l,r}} \right] - k_{br} \frac{\partial}{\partial Y_j} \left[\prod_{l=1}^{N_s} \left(\frac{\rho Y_l}{M_l} \right)^{v''_{l,r}} \right]$$

The result after simplifying is

$$\left[\frac{\partial R_r}{\partial Y_j} \right]_{C, Y_s \neq Y_j, T} = \frac{1}{Y_j} (v'_{j,r} R_{fr} - v''_{j,r} R_{br})$$

We recognize that $\frac{\partial Y_j}{\partial Y_i}$ is simply δ_{ij} , and therefore we have

$$\sum_{j=1}^{N_s} \left[\frac{\partial R_r}{\partial Y_j} \right]_{C, Y_s \neq Y_j, T} \left[\frac{\partial Y_j}{\partial Y_i} \right]_{C, Y_s \neq Y_j, T} = \frac{1}{Y_i} (v'_{i,r} R_{fr} - v''_{i,r} R_{br})$$

The resulting Jacobian term is therefore

$$\frac{\partial S_s}{\partial Q_i} = \frac{M_s}{\rho Y_i} \sum_{r=1}^{N_r} [(v''_{s,r} - v'_{s,r})(v'_{i,r} R_{fr} - v''_{i,r} R_{br})]$$

Jacobian of the Numerical Inviscid Fluxes

The numerical edge-based inviscid flux in the chemical system is given by

$$F_{s,ij}^i = \boldsymbol{\eta}_{ij} \cdot \frac{\mathbf{F}_{s,j}^i + \mathbf{F}_{s,i}^i}{2} = \hat{F}_{ij}^\rho \begin{cases} Y_{s,i} & \text{if } \hat{F}_{ij}^\rho \geq 0 \\ Y_{s,j} & \text{else} \end{cases}$$

We assume that the total mass flux from the flow solver is constant with respect to the species densities. Taking the derivatives with respect to the i and j nodes yields the following

$$\frac{\partial F_{s,ij}^i}{\partial Q_{s,i}} = \frac{\partial F_{s,ij}}{\partial Y_{s,i}} \frac{\partial Y_{s,i}}{\partial Q_{s,i}} = \frac{\hat{F}_{ij}^\rho}{\rho_i} \begin{cases} 1 & \text{if } \hat{F}_{ij}^\rho \geq 0 \\ 0 & \text{else} \end{cases}$$

$$\frac{\partial F_{s,ij}^i}{\partial Q_{s,j}} = \frac{\partial F_{s,ij}^i}{\partial Y_{s,j}} \frac{\partial Y_{s,j}}{\partial Q_{s,j}} = \frac{\hat{F}_{ij}^\rho}{\rho_j} \begin{cases} 0 & \text{if } \hat{F}_{ij}^\rho \geq 0 \\ 1 & \text{else} \end{cases}$$

Jacobian of the Numerical Viscous Fluxes

The edge-based numerical viscous flux in the chemical system is given by

$$F_{s,ij}^v = \text{tr}(\mathbf{D}_{ij}^S) [-\rho_{ij} D_{ij} (Y_{s,j} - Y_{s,i})]$$

We assume that the change in the midpoint density and diffusion coefficient is negligible. Taking the derivative with respect to the i and j nodes yields

$$\frac{\partial F_{s,ij}^v}{\partial Q_{s,i}} = \frac{\partial F_{s,ij}^v}{\partial Y_{s,i}} \frac{\partial Y_{s,i}}{\partial Q_{s,i}} = \text{tr}(\mathbf{D}_{ij}^S) (-\rho_{ij} D_{ij}) (-1) \frac{1}{\rho_i}$$

$$\frac{\partial F_{s,ij}^v}{\partial Q_{s,j}} = \frac{\partial F_{s,ij}^v}{\partial Y_{s,j}} \frac{\partial Y_{s,j}}{\partial Q_{s,j}} = \text{tr}(\mathbf{D}_{ij}^S) (-\rho_{ij} D_{ij}) (1) \frac{1}{\rho_j}$$

Jacobian of the Inter-diffusional Heat Flux

The edge-based numerical inter-diffusional heat flux in the flow system is given by

$$F_{ij}^{E,D} = \text{tr}(\mathbf{D}_{ij}^S) (-\rho_{ij} D_{ij}) \sum_{s=1}^{N_s} h_{s,ij} (Y_{s,j} - Y_{s,i})$$

It is assumed that the change in the diffusion coefficient is negligible. The derivative with respect to the total energy per unit volume at node i is

$$\frac{\partial F_{ij}^{E,D}}{\partial (\rho e)_i} = \left[\frac{\partial F_{ij}^{E,D}}{\partial p_{ij}} \right]_{c,Y} \left[\frac{\partial p_{ij}}{\partial p_i} \right] \left[\frac{\partial p_i}{\partial (\rho e)_i} \right]_{\rho,u,v,e,Y} + \left[\frac{\partial F_{ij}^{E,D}}{\partial T_{ij}} \right]_{c,Y} \left[\frac{\partial T_{ij}}{\partial T_i} \right] \left[\frac{\partial T_i}{\partial (\rho e)_i} \right]_{\rho,u,v,e,Y}$$

where

$$\left[\frac{\partial T_{ij}}{\partial T_i} \right] = \frac{\partial}{\partial T_i} \left(\frac{T_i + T_j}{2} \right) = \frac{1}{2} \quad \text{and} \quad \left[\frac{\partial p_{ij}}{\partial p_i} \right] = \frac{\partial}{\partial p_i} \left(\frac{p_i + p_j}{2} \right) = \frac{1}{2}$$

The derivative with respect to the midpoint pressure is given by

$$\left[\frac{\partial F_{ij}^{E,D}}{\partial p_{ij}} \right]_{c,Y} = -\text{tr}(\mathbf{D}_{ij}^S) D_{ij} \frac{\partial \rho_{ij}}{\partial p_{ij}} \sum_{s=1}^{N_s} h_{s,ij} (Y_{s,j} - Y_{s,i})$$

where

$$\frac{\partial \rho_{ij}}{\partial p_{ij}} = \frac{\rho_{ij}}{p_{ij}}$$

therefore

$$\left[\frac{\partial F_{ij}^{E,D}}{\partial p_{ij}} \right]_{c,Y} = \frac{F_{ij}^{E,D}}{P_{ij}}$$

The derivative with respect to the midpoint temperature is given by

$$\left[\frac{\partial F_{ij}^{E,D}}{\partial T_{ij}} \right]_{c,Y} = -\text{tr}(\mathbf{D}_{ij}^S) D_{ij} \left[\frac{\partial \rho_{ij}}{\partial T_{ij}} \sum_{s=1}^{N_s} h_s(Y_{s,j} - Y_{s,i}) + \rho_{ij} \frac{\partial}{\partial T_{ij}} \left(\sum_{s=1}^{N_s} h_{s,ij}(Y_{s,j} - Y_{s,i}) \right) \right]$$

where

$$\frac{\partial \rho_{ij}}{\partial T_{ij}} = -\frac{\rho_{ij}}{T_{ij}} \quad \text{and} \quad \frac{\partial}{\partial T_{ij}} \left(\sum_{s=1}^{N_s} h_{s,ij}(Y_{s,j} - Y_{s,i}) \right) = \sum_{s=1}^{N_s} C_{p,s,ij}(Y_{s,j} - Y_{s,i})$$

therefore

$$\left[\frac{\partial F_{ij}^{E,D}}{\partial T_{ij}} \right]_{c,Y} = -\text{tr}(\mathbf{D}_{ij}^S) \rho_{ij} D_{ij} \left[\frac{-1}{T_{ij}} \sum_{s=1}^{N_s} h_{s,ij}(Y_{s,j} - Y_{s,i}) + \sum_{s=1}^{N_s} C_{p,s,ij}(Y_{s,j} - Y_{s,i}) \right]$$

Finally, the derivatives of the pressure and temperature with respect to the total energy are given by

$$\left[\frac{\partial p}{\partial \rho e} \right]_{\rho,u,v,w,Y} = \frac{R}{C_v}$$

$$\left[\frac{\partial T}{\partial \rho e} \right]_{\rho,u,v,w,Y} = \frac{1}{\rho C_v}$$

The final expression of the Jacobian is therefore

$$\frac{\partial F_{ij}^{E,D}}{\partial (\rho e)_i} = \frac{F_{ij}^{E,D}}{P_{ij}} \frac{R}{2C_v} - \left[\frac{F_{ij}^{E,D}}{T_{ij}} + \text{tr}(\mathbf{D}_{ij}^S) \rho_{ij} D_{ij} \sum_{s=1}^{N_s} C_{p,s,ij}(Y_{s,j} - Y_{s,i}) \right] \frac{1}{2\rho C_v}$$

Jacobian of the Inter-diffusional Vibrational-electronic Energy Flux

The contribution of the species mass diffusion to the vibrational-electronic energy is given by

$$F_{ij}^{VE,D} = \text{tr}(\mathbf{D}_{ij}^S) (-\rho_{ij} D_{ij}) \sum_{s=1}^{N_s} e_{s,ve,ij}(Y_{s,j} - Y_{s,i})$$

The Jacobian with respect to the vibrational energy per unit volume at node i is given by

$$\frac{\partial F_{ij}^{VE,D}}{\partial(\rho e_{ve})_i} = \left[\frac{\partial F_{ij}^{VE,D}}{\partial(T_{ve})_{ij}} \right]_{\mathbf{c}, \mathbf{Y}, T_{tr}} \left[\frac{\partial(T_{ve})_{ij}}{\partial(T_{ve})_i} \right] \left[\frac{\partial(T_{ve})_i}{\partial(\rho e_{ve})_i} \right]$$

following a derivation similar to the previous section, we obtain

$$\frac{\partial F_{ij}^{VE,D}}{\partial(\rho e_{ve})_i} = - \frac{\text{tr}(\mathbf{D}_{ij}^S) \rho_{ij} D_{ij}}{2 \rho_i C_{v,ve,i}} \sum_{s=1}^{N_s} C_{v,s,ve,ij} (Y_{s,j} - Y_{s,i})$$

Jacobian of the Vibration-dissociation Source Term

The contribution of the chemical source term to the production or destruction of vibrational-electronic energy, assuming a non-preferential model is given by

$$Q_{V-D} = \sum_{s=1}^{N_s} \omega_s (e_{v,s} + e_{el,s})$$

Recall that the total energy and vibrational-electronic per unit volume are given by

$$\rho e(\rho, \mathbf{Y}, \mathbf{V}, T_{tr}, T_{ve}) = \rho \sum_s Y_s C_{v,tr,s} T_{tr} + \frac{1}{2} \rho \mathbf{V} \cdot \mathbf{V} + \rho \sum_s Y_s h_s^0 + \rho e_{ve}(\rho, \mathbf{Y}, T_{ve})$$

$$\rho e_{ve}(\rho, \mathbf{Y}, T_{ve}) = \rho \sum_s Y_s (e_{v,s} + e_{el,s})$$

The derivative of the vibration-dissociation source term with respect to the total vibrational-electronic energy holding the gasdynamic quantities and the mass fraction vector is given by

$$\frac{\partial Q_{V-D}}{\partial \rho e_{ve}} = \frac{\partial}{\partial \rho e_{ve}} \left[\sum_{s=1}^{N_s} \omega_s (e_{v,s} + e_{el,s}) \right]_{\mathbf{c}, \mathbf{Y}}$$

Let $\rho e_{ve} = E^{ve}$

$$\frac{\partial Q_{V-D}}{\partial E^{ve}} = \sum_{s=1}^{N_s} \left[\frac{\partial \omega_s}{\partial E^{ve}} \Big|_{\rho, \mathbf{Y}, \mathbf{V}, T_{tr}} (e_{v,s} + e_{el,s}) + \omega_s (C_{v,v,s} + C_{v,el,s}) \frac{\partial T_{ve}}{\partial E^{ve}} \Big|_{\rho, \mathbf{Y}, \mathbf{V}, T_{tr}} \right]$$

where

$$\frac{\partial T_{ve}}{\partial E^{ve}} \Big|_{\rho, \mathbf{Y}} = \frac{1}{\rho C_{v,ve}}$$

Recall that

$$\omega_s = M_s \sum_{r=1}^{N_r} (v''_{s,r} - v'_{s,r}) (R_{f,r}(\rho, \mathbf{Y}, T_{tr}, T_{ve}) - R_{b,r}(\rho, \mathbf{Y}, T_{tr}))$$

The derivative of the chemical source term with respect to the total vibrational-electronic energy is given by

$$\frac{\partial \omega_s}{\partial E^{ve}} = M_s \sum_{r=1}^{N_r} (v''_{s,r} - v'_{s,r}) \left(\frac{\partial R_{f,r}(\rho, Y, T_{tr}, T_{ve})}{\partial E^{ve}} \Big|_{\rho, Y, T_{tr}} \right)$$

where

$$\frac{\partial R_{f,r}}{\partial E^{ve}} \Big|_{\rho, Y, T_{tr}} = \frac{\partial k_{f,r}(T_c)}{\partial T_c} \frac{\partial T_c(T_{tr}, T_{ve})}{\partial T_{ve}} \Big|_{T_{tr}} \frac{\partial T_{ve}(\rho, Y, E^{ve})}{\partial E^{ve}} \Big|_{\rho, Y} \prod_{i=1}^{N_s} \left(\frac{\rho Y_i}{M_i} \right)^{v'_{i,r}}$$

Recall that

$$k_{f,r}(T_c) = A_{f,r} T_c^{\eta_{f,r}} \exp\left(-\frac{E_{a,r}}{R_u T_c}\right), \quad T_c = \begin{cases} T_{tr}^q T_{ve}^{q-1} & \text{if dissociation} \\ T_{tr} & \text{else} \end{cases}$$

Therefore

$$\begin{aligned} \frac{\partial k_{f,r}(T_c)}{\partial T_c} &= A_{f,r} \left(\eta_{f,r} T_c^{\eta_{f,r}-1} \exp\left(-\frac{E_{a,r}}{R_u T_c}\right) + \frac{T_c^{\eta_{f,r}} E_{a,r}}{R_u T_c^2} \exp\left(-\frac{E_{a,r}}{R_u T_c}\right) \right) \\ &= \frac{\partial k_{f,r}(T_c)}{\partial T_c} = \frac{k_{f,r}(T_c)}{T_c} \left(1 + \frac{E_{a,r}}{R_u T_c} \right) \end{aligned}$$

and

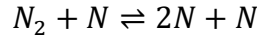
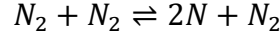
$$\frac{\partial T_c}{\partial T_{ve}} \Big|_{T_{tr}} = T_{tr}^q (q-1) T_{ve}^{q-2} = \frac{T_c (q-1)}{T_{ve}}$$

Finally, the complete Jacobian is given by

$$\begin{aligned} \frac{\partial Q_{V-D}}{\partial E^{ve}} &= \frac{T_c (q-1)}{T_{ve} \rho C_{v,ve}} \sum_{s=1}^{N_s} \left[(e_{v,s} + e_{el,s}) M_s \sum_{r=1}^{N_r} (v''_{s,r} - v'_{s,r}) \left[\left(\frac{k_{f,r}}{T_c} \left(1 + \frac{E_{a,r}}{R_u T_c} \right) \right) \prod_{i=1}^{N_s} \left(\frac{\rho Y_i}{M_i} \right)^{v'_{i,r}} \right] \right. \\ &\quad \left. + \omega_s (C_{v,v,s} + C_{v,el,s}) \right] \end{aligned}$$

Appendix D: Example of Reaction Kinetics

We consider the basic dissociation of nitrogen given by the following set of reactions:



We therefore have a system with $N_s = 2$ and $N_r = 2$. The stoichiometric matrices are given by:

$$[v'] = \begin{bmatrix} 2 & 0 \\ 1 & 1 \end{bmatrix}, \quad [v''] = \begin{bmatrix} 1 & 2 \\ 0 & 3 \end{bmatrix}$$

Firstly, we calculate the forward and backward reaction rates:

$$R_{f,1} = k_{f,1} \prod_{i=1}^{N_s} \left(\frac{\rho Y_i}{M_i} \right)^{v'_{i,1}} = k_{f,1} \left(\frac{\rho Y_{N_2}}{M_{N_2}} \right)^2$$

$$R_{b,1} = k_{b,1} \prod_{i=1}^{N_s} \left(\frac{\rho Y_i}{M_i} \right)^{v''_{i,1}} = k_{b,1} \left(\frac{\rho Y_{N_2}}{M_{N_2}} \right)^1 \left(\frac{\rho Y_N}{M_N} \right)^2$$

$$R_{f,2} = k_{f,2} \left(\frac{\rho Y_{N_2}}{M_{N_2}} \right)^1 \left(\frac{\rho Y_N}{M_N} \right)^1$$

$$R_{b,2} = k_{b,2} \left(\frac{\rho Y_N}{M_N} \right)^3$$

The full rates of progress in mol/(m³·s) are therefore given by:

$$R_1 = k_{f,1} \left(\frac{\rho Y_{N_2}}{M_{N_2}} \right)^2 - k_{b,1} \left(\frac{\rho Y_{N_2}}{M_{N_2}} \right)^1 \left(\frac{\rho Y_N}{M_N} \right)^2$$

$$R_2 = k_{f,2} \left(\frac{\rho Y_{N_2}}{M_{N_2}} \right)^1 \left(\frac{\rho Y_N}{M_N} \right)^1 - k_{b,2} \left(\frac{\rho Y_N}{M_N} \right)^3$$

The net rate of production in kg/(m³·s) is given by:

$$\begin{aligned} \dot{\omega}_{N_2} &= M_{N_2} [(v''_{N_2,1} - v'_{N_2,1})R_1 + (v''_{N_2,2} - v'_{N_2,2})R_2] \\ &= M_{N_2} [(-1)R_1 + (-1)R_2] \end{aligned}$$

$$\dot{\omega}_N = M_N [(2)R_1 + (2)R_2]$$

Appendix E: Chemical Equilibrium Solver

List of Symbols:

N_s	Number of species	K_{eq}	Equilibrium constant
N_e	Number of elements	μ_i	Chemical potential of species i
G_i	Gibbs free energy of species i	R	Gas constant
T	Temperature	a_{ij}	Number of atoms of i in species j
b_i	Initial number of mols of element i	N_i	Number of mols of species i
P	Pressure	P_0	Reference pressure

Free energy minimization is a common technique used to compute chemical equilibrium compositions. The formulation of a minimization problem is made relatively simple if all species are assumed to remain in the gas phase and isothermal and isobaric conditions are imposed. This technique has the benefit of not requiring a priori knowledge of the relevant reactions occurring in the gas.

Methodology

The equilibrium constant of a reaction is given by the ratio of the product concentrations to the reactant concentrations, shown below

$$K_{eq} = \frac{\prod_{i=1}^{N_s} [B]_i^{v_i''}}{\prod_{i=1}^{N_s} [B]_i^{v_i'}}$$

If the equilibrium constant for a given thermodynamic state is known, then the equilibrium gas composition may be computed. However, for large systems with many species and reactions, this is generally not feasible. Alternatively, the equilibrium composition may be found by minimizing the Gibbs free energy of the system. The Gibbs free energy change for a reaction is given by

$$\Delta_r G^o = -RT \ln K_{eq}$$

The formal definition of the Gibbs free energy is

$$G = u + Pv - Ts$$

where u , v and s are the specific energy, volume and entropy. Taking the derivative yields

$$dG = \left(\frac{dG}{dT}\right)_{P,N} dT + \left(\frac{dG}{dP}\right)_{T,N} dP + \sum_{i=1}^{N_s} \left(\frac{dG}{dN_i}\right)_{P,T,N_i} dN_i$$

Where N_i is the number of moles of species i . Assuming a reaction occurring at constant temperature and pressure, the equilibrium condition is given by

$$dG = \sum_{i=1}^{N_s} \mu_i dN_i = \sum_{i=1}^{N_s} \left(\frac{dG}{dN_i} \right)_{T,P,N_i} dN_i = 0$$

Where we have defined the chemical potential μ_i . For an ideal gas, this is simply the Gibbs free energy of a species, plus a contribution from the pressure of the system:

$$\mu_i = G_i + R_u T \left[\ln \left(\frac{N_i}{N_{tot}} \right) \right]$$

Which may be readily computed with the NASA thermodynamic polynomials. When solving for the equilibrium composition, the number of mols of each species, N_i , as well as the total number of moles N_{tot} are required. We note that the number of mols of each species are constrained by elemental mass balances. The constraint equations are given by

$$\sum_{j=1}^{N_s} a_{ij} N_j - b_i = 0 = \psi_i(\mathbf{N}) \quad \forall i \in N_e$$

Where a_{ij} is the number of atoms of element i in species j , and b_i is the initial number of mols of element i . We are thus presented with the following constrained minimization problem

$$\text{Minimize } G(T, P, \mathbf{N}) \text{ subject to the constraints } \psi(\mathbf{N})$$

We can solve this system by introducing Lagrange multipliers. The objective function G is extended with the constraint equations multiplied by the Lagrange multipliers and subsequently derived to obtain the following

$$dG = \sum_{i=1}^{N_s} \left(\mu_i + \sum_{j=1}^{N_e} \lambda_j a_{ij} \right) dN_i + \sum_{j=1}^{N_e} \psi_j d\lambda_j$$

The system to be solved therefore consists of the following equations

$$\begin{aligned} \mu_i + \sum_{j=1}^{N_e} \lambda_j a_{ij} &= 0 \quad \forall i \in N_s \\ \sum_{i=1}^{N_s} a_{ij} N_i - b_j &= 0 \quad \forall j \in N_e \end{aligned}$$

$$N_{tot} - \sum_{i=1}^{N_s} N_i = 0$$

The system is solved iteratively using a Newton Raphson technique. The following first order expansion is introduced

$$N_i^{n+1} \approx N_i^n + \delta N_i$$

Taking the first equation we have

$$0 = G_i + RT[\ln(N_i^n + \delta N_i) - \ln(N_{tot}^n + \delta N_{tot}) + \ln(P/P_0)]$$

$$\delta \ln N_i - \delta \ln N_{tot} + \frac{1}{RT} \sum_{j=1}^{N_e} \lambda_j a_{ij} = -\frac{\mu_i}{RT} \quad \forall i \in N_s$$

For the constraint equation, the correction variables are modified to be the same as the previous equation

$$N_i^{n+1} \approx N_i^n + N_i^n \delta \ln N_i$$

Therefore, we have the following equations arising from the elemental and total constraints

$$\sum_{i=1}^{N_s} a_{ij} N_i \delta \ln N_i = b_j - \sum_{i=1}^{N_s} a_{ij} N_i \quad \forall j \in N_e$$

$$\sum_{i=1}^{N_s} N_i \delta \ln N_i - N_{tot} \delta \ln N_{tot} = N_{tot} - \sum_{i=1}^{N_s} N_i$$

which forms the system to be solved. An example system is shown below for a gas mixture consisting of 5 species and 3 elements

$$\begin{bmatrix} 1 & 0 & 0 & 0 & 0 & -a_{11} & -a_{21} & -a_{31} & 1 \\ 0 & 1 & 0 & 0 & 0 & -a_{12} & -a_{22} & -a_{32} & 1 \\ 0 & 0 & 1 & 0 & 0 & -a_{13} & -a_{23} & -a_{33} & 1 \\ 0 & 0 & 0 & 1 & 0 & -a_{14} & -a_{24} & -a_{34} & 1 \\ 0 & 0 & 0 & 0 & 1 & -a_{15} & -a_{25} & -a_{35} & 1 \\ a_{11}N_1 & a_{12}N_2 & a_{13}N_3 & a_{14}N_4 & a_{15}N_5 & 0 & 0 & 0 & 0 \\ a_{21}N_1 & a_{22}N_2 & a_{23}N_3 & a_{24}N_4 & a_{25}N_5 & 0 & 0 & 0 & 0 \\ a_{31}N_1 & a_{32}N_2 & a_{33}N_3 & a_{34}N_4 & a_{35}N_5 & 0 & 0 & 0 & 0 \\ N_1 & N_2 & N_3 & N_4 & N_5 & 0 & 0 & 0 & -N_{tot} \end{bmatrix} \begin{bmatrix} \delta \ln N_1 \\ \delta \ln N_2 \\ \delta \ln N_3 \\ \delta \ln N_4 \\ \delta \ln N_5 \\ \lambda'_1 \\ \lambda'_2 \\ \lambda'_3 \\ \delta \ln N_{tot} \end{bmatrix} = \begin{bmatrix} -\mu_1/R_u T \\ -\mu_2/R_u T \\ -\mu_3/R_u T \\ -\mu_4/R_u T \\ -\mu_5/R_u T \\ b'_1 \\ b'_2 \\ b'_3 \\ N' \end{bmatrix}$$

where the following variables are introduced for clarity

$$\lambda' = -\frac{\lambda}{RT}, \quad b' = b_j - \sum_{i=1}^{N_s} a_{ij} N_i, \quad N' = N_{tot} - \sum_{i=1}^{N_s} N_i$$

After solving the linear system, the number of moles of each species are updated as follows

$$N_i^{n+1} = \exp(\ln(\max(\epsilon, N_i^n)) + r\Delta \ln N_i)$$

where ϵ is a small number to avoid taking the logarithm of zero and r is a relaxation factor.

The solver is used to compute the equilibrium composition of a 5-species air mixture up to 10000 K. The gas is composed of 79% diatomic nitrogen and 21% diatomic oxygen by mass and the pressure is kept at 101325 Pa.

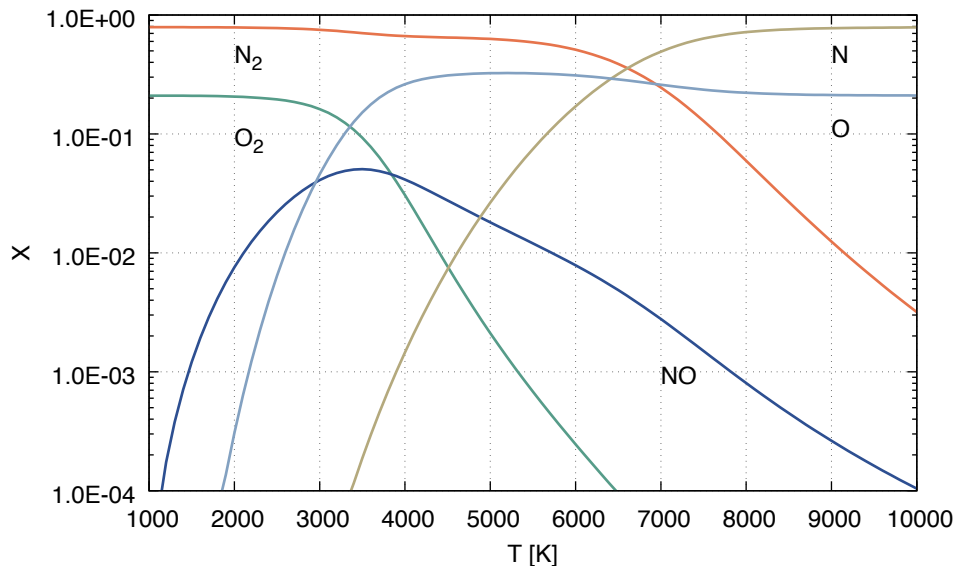


Figure A.1 - Equilibrium molar fractions of five-species air model

The extension to ionized gases requires the addition of a conservation of electric charge equation to the system. The coupling of this solver to the HALO3D code may be done to simulate chemical non-equilibrium flow fields or boundary conditions. These tasks are planned as future work.